Correlation between plasma and beam properties at the ELISE test facility

Isabella Mario

Angaben zur Veröffentlichung / Publication details:

Mario, Isabella. 2020. "Correlation between plasma and beam properties at the ELISE test facility." Augsburg: Universität Augsburg.

Correlation between plasma and beam properties at the ELISE test facility

Dissertation

zur Erlangung des akademischen Grades

Dr. rer. nat.

eingereicht an der
Mathematisch-Naturwissenschaftlich-Technischen Fakultät
der Universität Augsburg

von

Isabella Mario

Augsburg, August 2020

Vorgelegt am 03.08.2020

Tag der mündlichen Prüfung: 18.02.2021

Erste Gutachterin: Prof. Dr.-Ing. Ursel Fantz

Zweiter Gutachter: Prof. Dr. Helmut Karl

Contents

1 Introduction

Fusion power plants based on magnetic confinement can provide a reliable, safe, and environmentally low-impact source of energy. ITER, the first experimental fusion reactor, is under construction in Cadarache (FR) and shall prove the feasibility of fusion as a large-scale source of energy. ITER will open the way to the DEMO power plant, which will safely generate electricity and prove regular, rapid, and reliable maintenance of the plant. The main reaction in fusion power plants is the fusion between deuterium and tritium into a fast helium particle and a fast neutron. To enable and sustain the fusion reaction, a high temperature ($>$ 100 million K) is needed. An important component of ITER is the neutral beam injection (NBI) system, where a beam of fast hydrogen or deuterium atoms is injected in the fusion plasma. ITER will include two NBI systems delivering a total of 33 MW.

The ITER NBI system consists of a 2 m high 1 m wide ion source from which negative H or D ions are extracted and accelerated by an electrostatic, multi-aperture and multi-grid extraction and acceleration system: seven grids for a total HV applied up to 1 MeV are divided vertically into segments each one hosting 320 apertures arranged in 4 groups of 5 $\times$ 16 apertures each. The grid segments are tilted vertically to focus the beam on a 1.08 m high 0.55 m wide port placed at 26 m distance from the grids. Steering and edge compensation of the beamlet are also applied to improve the beam transmission. The accelerated particles are then neutralized in a gas neutralizer; remaining charged particles are magnetically removed and dumped into a residual ion dump. The neutralized beam is injected into the fusion chamber and the beam particles deposit their energy into the fusion plasma via collisions.

The requirement for the ITER NBI ion source is to deliver an accelerated negative ion current density of 230 A/m^2 in hydrogen and 200 A/m^2 in deuterium with a total extraction area of 0.2 m^2 (1280 extraction apertures) and a co-extracted electron current lower than the negative ion current up to 3600 s in deuterium and 1000 s in hydrogen. The required particle energy is 1 MeV in deuterium and 870 keV in hydrogen. The beam homogeneity, defined among apertures, has to be higher than

90% over the total beam surface, and the single beamlet divergence has to be lower than 7 mrad. The requirements on the accelerated current density are transferred in terms of extracted current density when considering 30% of stripping losses, namely neutralization of negative ions before full acceleration through collisions with the background gas within the grids: 329 A/m^2 in hydrogen and 286 A/m^2 in deuterium. The neutral beam injection (NBI) system is based on RF-driven negative hydrogen or deuterium ion sources where the low-temperature, low-pressure plasma is generated by inductive coupling in 8 cylindrical drivers. Negative ions are mainly generated by surface conversion of atoms or positive ions on a low-work function surface, which corresponds to the first grid (plasma grid) of the extraction and acceleration system. The low work function is achieved by the evaporation of caesium into the ion source. The design of the NBI system requires research and development activities since the ITER requirements have never been achieved simultaneously by any negative ion source. In the framework of the European roadmap toward the ITER neutral beam injection system, the ELISE (Extraction from a Large Ion Source Experiment) test facility plays a fundamental role in demonstrating the scalability of the ion source design towards the full-size ITER NBI and allows long pulse plasma operation up to 1 hour with a large (1/2 of the ITER NBI source) negative ion source. The ELISE test facility is equipped with a half-size (1 m×1 m) ion source, which has half the height and the same width of the ITER NBI source. The plasma is generated by inductive coupling in 4 cylindrical drivers and is sustained up to steady-state. A three-grid multi-aperture electrostatic extraction system is attached to the negative ion source and allows extraction in pulsed mode (10 s every 150 s). The aperture arrangement in groups on the grids mimics the ITER arrangement. The total HV for extraction and acceleration at ELISE is limited to 60 kV with flat grids. The beam produced has a dimension of approximately 1 m × 1 m and the beam power density can be up to 2.5 MW/m^2. The limited total high voltage applied to the three-grid extraction and acceleration system, in comparison to the seven grids foreseen for ITER up to 1 MeV, results in a higher beam divergence at ELISE compared to the ITER requirement. The power density profile and the divergence of the beam produced at the ELISE test facility are very relevant for studying the power density distribution, i.e. beam homogeneity along the vertical and horizontal directions, accelerated current and divergence integrated over groups of apertures.

Inevitably with the extraction of negative ions, electrons are co-extracted, and they are dumped on the second grid (the extraction grid). The power load on the second grid must be reduced as much as possible, to avoid damages, hence the co-extracted

electron current has to be lower than the extracted negative ion current. Hence, the plasma close to the plasma grid has to be characterized by a high ratio between negative ions and electrons, namely an electronegative plasma. To achieve this condition, the destruction of negative ions, mainly due to collision with energetic electrons, must be minimized, thus a horizontal magnetic field, called filter field, is used to reduce electron temperature close to the plasma grid. The magnetic filter field is created by a current I_{PG} flowing vertically along the plasma grid. In addition to the filter field, the plasma grid is positively biased with respect to the source walls to further reduce the co-extraction of electrons. The presence of a horizontal filter field together with axial electric fields and density gradients lads to vertical plasma drifts which affect the vertical uniformity of the plasma density and the plasma potential.
The ITER requirements in terms of extracted currents have been achieved for short pulses in both H and D, whereas long pulses are challenging due to the temporal instability of the co-extracted electron current. While in hydrogen a current of $300\,\mathrm{A/m^2}$ could be maintained for 1000 s with an electron-to-ion ratio below the unity, the ITER requirements are not yet reached in deuterium during long pulses. The beam homogeneity at ELISE, which is defined between the top and bottom beam segments, shows a non-homogeneity in terms of beam segment width and peak intensity. The beam segments are characterized by a different top-bottom beam divergence as well. This work aims to improve the understanding of the relationship between plasma and extracted particles, i.e. co-extracted electrons and negative ions, to tackle the issues related to the long pulse stability and asymmetry of the co-extracted electrons. In deuterium the correlation between plasma and co-extracted electrons is of high relevance to find operational recipes to reduce the amount of co-extracted electrons, thus increasing the operational parameters to reach the extracted negative ion current density required for ITER. Investigations on the beam power density distribution and beam divergence are fundamental to identify the causes and to tackle the issues related to the beam homogeneity. Several diagnostics installed on the plasma and the beam side as well as electrical measurements on the ion source and beamline components are used to support the scope of this work. The different measurement domains of the diagnostic systems make the correlation between plasma and beam particularly challenging, since localized measurements, i.e. $\approx$ cm or line-of-sight integrated, are compared and correlated to measurements over large portions of the beam, i.e. grid and beam halves. The scalability of the ion source concept and performance make the studies performed at ELISE applicable to the full-size ITER ion source.

2 Negative ion sources for fusion

Thermonuclear fusion is a renewable source of energy, which can play a relevant role in the future, greenhouse-emission-free, energetic scenario. ITER, the first experimental fusion reactor, aims to demonstrate the technological feasibility of fusion and to achieve a gain factor of 10, defined as the ratio between the output fusion power and the input heating power. ITER is based on the magnetic confinement of a hot plasma ($\approx 100 \cdot 10^6\,\mathrm{K}$), since a very high temperature is needed to overcome the Coulomb barrier between the nuclei and, consequently, to increase the probability of the fusion process. The main fusion process is ${}^2\mathrm{D} + {}^3\mathrm{T} \rightarrow {}^4\mathrm{He}(3.5\,\mathrm{MeV}) + \mathrm{n}(14.1\,\mathrm{MeV})$[1] where the neutrons can escape the magnetic cage and transfer the kinetic energy into the blanket to the water coolant [2]. The net output energy is then used for production of electrical power.

ITER will be based on the tokamak concept, which uses a combination of toroidal and poloidal magnetic fields to confine the plasma inside a D-shaped section toroidal vessel (major radius 6.2 m, minor radius 2 m). The magnetic fields are created by magnetic field coils for the toroidal magnetic field and by a solenoid transformer which induces a toroidal current that, in turn, induces a poloidal magnetic field. The use of a solenoid transformer limit the pulse length to one hour. The combination of toroidal and poloidal magnetic fields results in a stable magnetic confinement of the plasma. A sketch of the tokamak configuration is shown in figure 2.1.

The experimental phases for ITER are three: an initial testing phase of the system with hydrogen plasma without fusion reactions, then a deuterium - deuterium plasma phase[1] and finally a deuterium - tritium phase. The plasma is sustained by plasma ohmic heating, auxiliary heating systems based on electromagnetic wave coupling (electron cyclotron resonance heating -ECRH- for electron heating and ion cyclotron resonance heating -ICRH- for ion heating) and heating based on neutral beam injection -NBI-. The former systems are foreseen to deliver a total power of 20 MW, the

[1] where the main fusion reaction is ${}^2\mathrm{D} + {}^2\mathrm{D} \rightarrow {}^3\mathrm{He}(0.82\,\mathrm{MeV}) + \mathrm{n}(2.45\,\mathrm{MeV})(50\%)$ or ${}^2\mathrm{D} + {}^2\mathrm{D} \rightarrow {}^3\mathrm{T}(1.01\,\mathrm{MeV}) + \mathrm{p}(3.02\,\mathrm{MeV})(50\%)$[1]

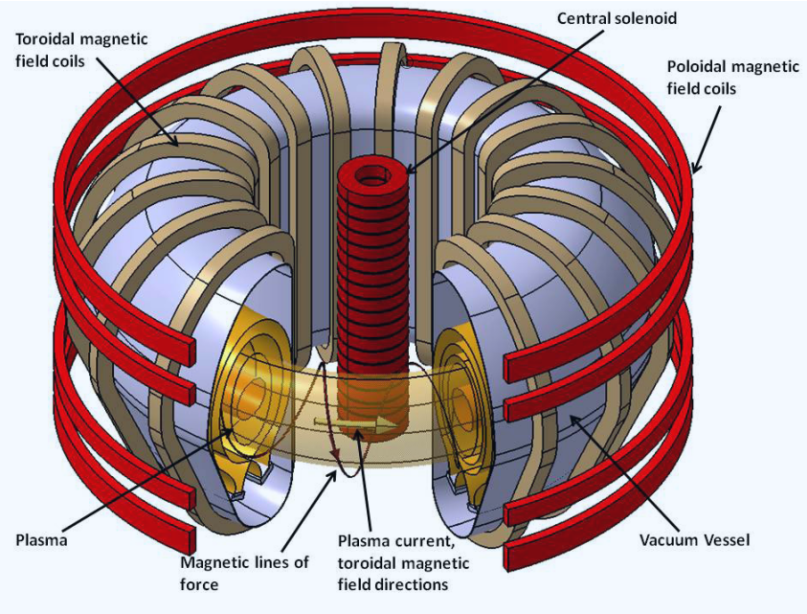

Figure 2.1: Sketch of the Tokamak configuration for a fusion device. External poloidal coils create a toroidal field, whereas a central solenoid induces a toroidal electrical current, thus resulting in a poloidal magnetic field. Poloidal magnetic field coils are used to control the plasma positioning and shape [1].

latter a total power of 33 MW divided in two NBI beamlines [3][4].
The NBI heating systems transfer energy to the fusion plasma through collisions of fast hydrogen or deuterium particles: after entering the fusion plasma the neutral beam is ionized and, consequently, confined by the magnetic field. NBI systems can drive a toroidal current if the beam is injected tangentially to the fusion chamber [5]. The NBI system can operate in hydrogen or in deuterium according to the need: in hydrogen during the initial testing phase of the systems whereas in deuterium for the D-D and the D-T campaigns.

2.1 Neutral beam injection for ITER

The ITER NBI system consists of several components: hydrogen or deuterium ions are created in a plasma inside an ion source attached to a multi-aperture, multi-grid electrostatic extraction and acceleration system made of 7 grids. 1280 beamlets, which are extracted and accelerated at the apertures up to the required energy, form a large beam which is neutralized downstream of the grid system in a gas neutralizer. Any residual ions are electrostatically deflected apart from the neutral beam into an ion dump. Up to now most operational NBI systems are based on positive ions whereas for ITER the NBI systems are based on negative ions. The choice depends on the

final particle energy and, since most of the fusion experiments require a moderate particle energy, most of the NBI systems in operation are based on positive ions, e.g. the NBI system at the Joint European Torus, Culham (UK) which requires a particle energy up to 160 keV [6]. In figure 2.2 the schematic of a NBI based on negative ions with all the aforementioned elements is shown.

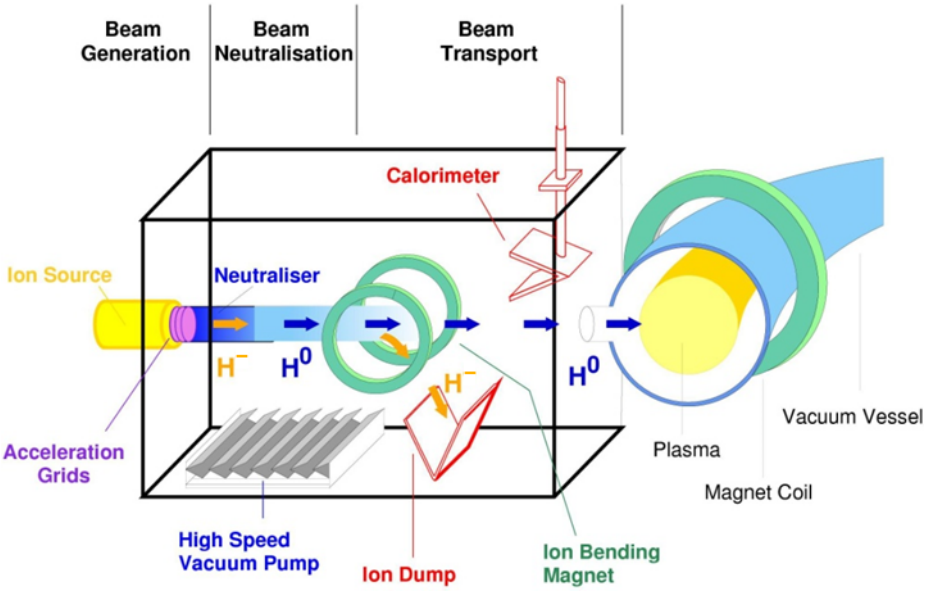

Figure 2.2: Scheme of a neutral beam injection system: consisting of an ion source for negative hydrogen ions, a multi-aperture multi-grid electrostatic type acceleration system, a gas neutralizer and an ion dump for non-neutralized particles.

At the maximum energy required for ITER, i.e. 1 MeV, the choice between negative and positive ions for the NBI ion source is based on the neutralization efficiency: at this energy for an optimized gas neutralizer the neutralization efficiency is of few percent for positive ions whereas it is around 60% for negative ions. A plot of the maximum achievable neutralization efficiency for an optimized neutralizer is shown in figure 2.3. The main reason behind the high neutralization efficiency at high energies of negative ions is the low binding energy (about 0.75 eV [7][8]) of the second electron. On the other side, for positive ions, the neutralization efficiency is limited by the enhanced probability of ionization by collision of the neutrals at high current density or large size of the neutralizer [9].

The use of negative ions implies three major drawbacks:

- high destruction probability of the negative ions due to electron stripping and due to collisions with the background gas before full acceleration, i.e. within the

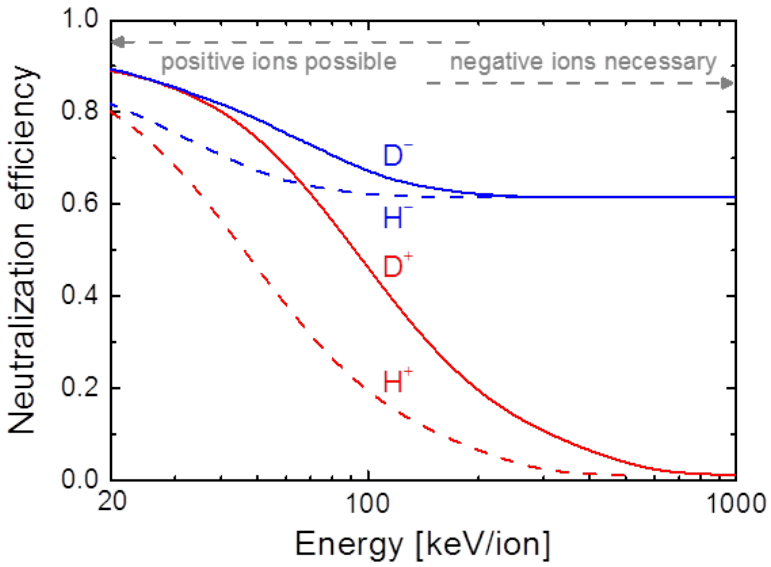

Figure 2.3: Neutralization efficiency of positive and negative hydrogen and deuterium ions as a function of the ion energy for optimum neutralizer thickness. At the energy foreseen for ITER, i.e. 1 MeV in D, the use of negative ions is mandatory [9].

extraction and acceleration system, due to the low binding energy of the second electron;

- simultaneous extraction of electrons, called co-extracted electrons, together with negative ions. Such electrons need to be removed from the beam before full acceleration to avoid power loads on downstream beamline components;

- production of negative ions (the production mechanisms will be discussed in section 2.2) is hard to achieve because it is mainly based on surface conversion, thus the negative ion extracted current density is typically one order of magnitude lower than for positive ion sources. Thus, for a comparable extracted ion current, negative ion sources are typically larger.

The above points determine two of the requirements for the ITER NBI source. The first is the pressure inside the grid system and, consequently, the source filling pressure (p_{fill}), that has to be equal or lower than 0.3 Pa to have a stripping fraction, i.e. neutralization of negative ions through collisions with the background gas particles, up to 30%. The second requirement involves the ratio between the co-extracted electrons and the extracted negative ions that must be lower than one in order to minimize the power load on the surfaces where the co-extracted electrons are dumped. To reach

the heating power foreseen for ITER with the limitation on the extracted negative ion density, the requirement for the ITER NBI total high voltage (HV) is of 1 MV for D (0.87 MV for H). The total accelerated current at the exit of the last grid has to be of 40 A in D (46 in H) from which the requirement for the extracted current of 57 A in D (66 A in H) is derived by considering 30% of stripping losses within the grid system. Strict requirements on the beam properties have to be fulfilled to maximize the beam transmission through the 26 m long beamline and to minimize the power loads on the beamline components: the beamlet divergence has to be lower than 7 mrad with 15% of the power in each beamlet carried by an 'halo' fraction with a divergence of 30 mrad [10]. Moreover, the power homogeneity among the 1280 beamlets must be better than 90% to avoid non homogeneous power deposition in the fusion plasma. The required pulse length is of 3600 s in D (1000 s in H). The ITER NBI requirements for hydrogen and deuterium are listed in table 2.1 [10].

	D	H
Final power (per beamline)	16.5 MW	16.5 MW
Particle energy	1 MeV	0.87 MeV
Accelerated current density	200 A/m^2	230 A/m^2
Extracted current density	286 A/m^2	329 A/m^2
Co-extracted electron to ion ratio	≤ 1	≤ 1
Source filling pressure	≤ 0.3 Pa	≤ 0.3 Pa
Pulse length	3600 s	1000 s
Beam homogeneity	$\geq 90\%$	$\geq 90\%$
Beam divergence	≤ 7 mrad	≤ 7 mrad

Table 2.1: Requirements for the ITER NBI system in case of hydrogen and deuterium operation[7][10]

The grid system foreseen for ITER has a total extraction area of 0.2 m^2 made of 1280 circular apertures with a diameter of 14 mm. The apertures are arranged in eight groups, called beamlet groups, each with 5 vertical columns of 16 apertures. The apertures in each beamlet group are separated by 20 mm gap in the horizontal direction and 22 mm gap in the vertical direction; the distance between the beamlet groups is 80 mm. All the grids are ≈ 1.6 m high and ≈ 0.8 m wide, each grid consists of four ≈ 0.4 m high, ≈ 0.8 m wide segments, vertically stacked. Each grid segment contains 4 beamlet groups, i.e. 320 apertures per segment. To ensure transmission through a 1.08 m high, 0.55 m wide port placed at about 26 m distance from the ion source, the grids are tilted, thus focusing the beam [10][11].
The extraction system consists of 2 grids, between which the extraction voltage is applied: the first grid is directly in contact with the plasma of the ion source and

it is called plasma grid (PG) and the second is the extraction grid (EG). The EG embeds permanent magnets, called deflection magnets, that magnetically dump the co-extracted electrons on the upstream side of the EG. The deflection magnets affect the beamlet particle trajectory, thus resulting in a left or right beamlet deflection for alternated rows: compensation magnets, named asymmetric deflection compensation magnets or ADCM, are embedded as well in the EG to compensate the beamlet deflection [10]. The EG is water-cooled and the power load is technologically limited. The distance between the two grids is 6 mm and the potential applied to the EG with respect to the PG is of about +10 kV [10].
The acceleration stages are five, each one of +200 kV, the distances between the grids are about 85 mm [10]; the last grid, the grounded grid (GG), is at ground potential, i.e. the ion source is at -1 MeV for deuterium operation (-870 keV for hydrogen operation). In the following, the extraction and acceleration voltages are indicated in absolute values without the sign which is anyway positive for the extraction and acceleration of negative ions.
Two different ion source concepts have been developed and can be employed in neutral beam injection: arc source and radio frequency (RF) driven source. These two concepts differ for the plasma generation mechanism: in both cases the plasma is generated through collisions of electrons with the background gas, but in the first case the plasma is generated starting from electrons emitted via thermionic emission from hot tungsten filaments [12] whereas for RF-driven sources the electron motion is induced by RF-field produced by means of radio frequency coils [13]. The latter is chosen for the ITER NBI system because less maintenance is required with respect to the arc source concept.
The European roadmap to meet the ITER target design and operational parameters in time for the ITER construction envisages preparatory design activity and R&D [14]. For this reason several test facilities are currently in operation and others are under construction:

- the **BATMAN**[2] testbed located at IPP Garching is equipped with a prototype RF-driven ion source (1/8 of the ITER NBI ion source) which started operation in the late 1990s [13]. The test facility was designed to run short plasma pulses up to about 7 s and 5 s extraction phases due to limitations on the HV power supply and on the vacuum system. The maximum HV is 22 kV for a three-grid extraction and acceleration system. The testbed could run in hydrogen or

[2] **BA**varian **T**est **MA**chine for **N**egative ions

in deuterium. The facility has been upgraded in 2016 [15] with a new ITER-like grid system and the possibility to have up to 10 s extraction phases with a total HV up to 50 kV. The upgrade aims to improve the extraction system and the beam diagnostics. The BATMAN test facility demonstrated the ITER requirements for the extracted current density and the electron to ion ratio at 0.3 Pa source pressure [16].

- the **ELISE**[3] test facility is located at IPP, Garching. The 1 m high, 1 m wide RF-driven ion source (1/2 of the ITER NBI ion source) started operation in 2013. The test facility can operate in H and D and sustain the RF plasma in steady state. The extraction is pulsed: for 9.5 s every ≈ 150 s and up to 60 kV total HV for a three-grid extraction and acceleration system [17][18]. The target for ELISE is to demonstrate the size scalability of the RF driven ion source concept in terms of extracted negative ion current density and co-extracted electron density for a large extraction area (about 0.1 m^2) and in long pulses [19][16]. A detailed description of ELISE will be given in chapter 3.

- the **SPIDER**[4] test facility in operation since 2018 at Consorzio RFX, Padova is a full-size ITER NBI ion source [20]. The SPIDER experiment is part of the PRIMA[5] [21] test facility. SPIDER has the same size as the ITER NBI ion source and the same extractor design, can be operated in H and in D and provides a total acceleration of 100 keV with a three-grid system for a pulse duration up to 3600 s. The target of SPIDER is to demonstrate the ITER requirements for the negative ion and co-extracted electron current densities for pulses up to one hour. For SPIDER also the requirement for the beam homogeneity will be tackled.

- the **MITICA**[6] test facility [21] is also included in the PRIMA facility at Consorzio RFX, Padova. MITICA is a full-scale prototype of the ITER NBI and will start operation in 2023 [22]. The target of MITICA is to fulfill all the ITER requirements for the full beamline, including the homogeneity and divergence requirements. MITICA will also represent a testbed, where solutions to the eventual issues connected to the achievement of ITER NBI requirements will be tested.

[3] **E**xtraction from a **L**arge **I**on **S**ource **E**xperiment
[4] **S**ource for **P**roduction of **I**on of **D**euterium **E**xtracted from **R**F plasma
[5] **P**adova **R**esearch on **I**TER **M**egavolt **A**ccelerator
[6] **M**egavolt **IT**ER **I**njector & **C**oncept **A**dvancement

In figure 2.4 the size scaling of the two negative ion sources at BATMAN and ELISE in comparison with the ion source for the ITER NBI (SPIDER and MITICA) is shown. A more comprehensive description of the ion source will be discussed in section 2.3.

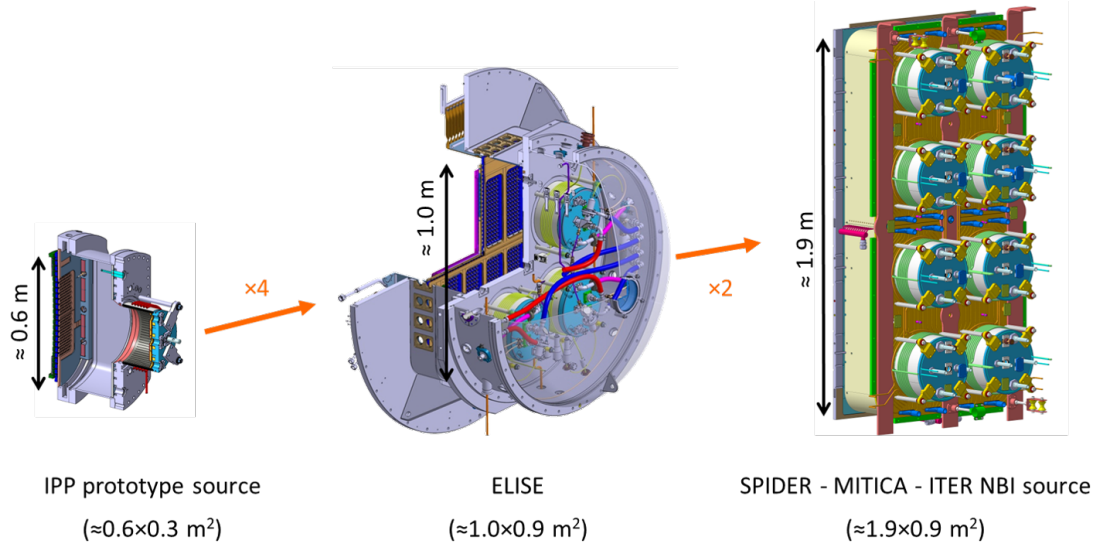

Figure 2.4: Schematic showing the size scaling between the RF driven prototype source at BATMAN (1/8 of the ITER-NBI source size), at ELISE (half the ITER-NBI source size) and the full source for ITER installed at SPIDER and MITICA [13][17][22][20].

2.2 Negative ion production and destruction mechanisms

Due to the low binding energy (0.75 eV) of the second electron in a H^- (or D^-) ion, the electron can be easily stripped, i.e. removed through collisions with the background particles. In order to preserve the negative ions, collisions with the background particles and with energetic electrons must be avoided: low-pressure, low temperature plasmas are then mandatory to reduce the destruction rate of the negative ions, thus improving the efficiency of the ion source [23].
Two processes can contribute to the negative ion generation: volume production [8][24] and surface production [25].

- **Volume production.** Negative ions are produced by dissociative electron attachment of vibrationally excited molecules:

$$H_2(\nu'') + e \rightarrow H_2^- \rightarrow H^- + H \tag{2.1}$$

where ν'' is the vibration state number. If $\nu'' > 5$ ($\nu'' > 8$ for D_2), the threshold energy for dissociative attachment is lower than 1 eV and the cross section increases for increasing vibrational level [26]. Therefore, the condition that enhances the volume production of negative ions is represented by a plasma populated by high vibrationally-excited molecules and a low electron energy ($T_e \leq 1\,\text{eV}$). On the other hand, the production of such highly vibrationally-excited molecules is more probable through collisions with energetic electrons ($\geq 10\,\text{eV}$) [26], thus two separate parts are necessary for optimizing the volume production of negative ions: one part with high electron energy where highly vibrationally-excited molecules are created and another part with low electron energy to enhance the volume production of negative ions.

- **Surface production.** Negative ions are produced from atoms or positive ions interacting with a low work function surface:

$$H + e^-_{\text{surface}} \rightarrow H^- \tag{2.2}$$

$$H^+_x + e^-_{\text{surface}} \rightarrow H + e^-_{\text{surface}} \rightarrow H^- \tag{2.3}$$

  where e^-_{surface} is an electron belonging to the conduction band (with an energy close to the Fermi energy) of the metallic surface where the conversion takes place. The electron reaches the affinity level of a hydrogen atom located close to the surface by quantum tunneling: the hydrogen atom captures the electron and escapes as an H^- ion [8][27]. The lower the work function of the surface, the higher the probability of quantum tunneling to occur, hence the higher the production efficiency of negative ions via surface production.

Surface production is the most relevant process in the negative ion production for NBI.

Surface production of negative ions is efficient if the work function of the conversion surface is low, which is not the case of the metals used for the ion source surfaces (i.e. $> 4\,\text{eV}$), thus the work function is lowered by adsorption of alkali or alkaline earth metals. Among the stable elements, caesium (Cs) with a work function of 2.14 eV is the one with the lowest work function. Since Cs is not applicable for constructing walls or grids due to the low melting point (28.5°C) [28] and the high reactivity, it is evaporated into the ion source through specific Cs ovens [27] and re-distributed on the source walls by the plasma. The work function of the conversion surface depends on the Cs coverage and on the possible impurities and compounds formed on the surfaces. Without considering the impurity level, the optimized Cs coverage reduces

the work function to a value below the one of the bulk Cs. In figure 2.5 the work function ϕ of a molybdenum surface as a function of the Cs coverage θ in monolayer is shown: without Cs, i.e. no coverage of the substrate, the work function is the one of the bulk molybdenum ϕ_{sub}. By increasing the Cs coverage, the work function decreases and reaches a minimum value ϕ_{min} at a minimum coverage θ_{min}, usually between 0.5 and 0.7 monolayer. The value of monolayers is obtained by averaging the coverage over a defined surface, thus also fractions can be obtained. When the coverage is above one monolayer the resulting work function is the one of bulk Cs. The same reasoning is valid for different metals as substrate and the minimum Cs coverage to obtain the minimum work function can be found in reference [29].

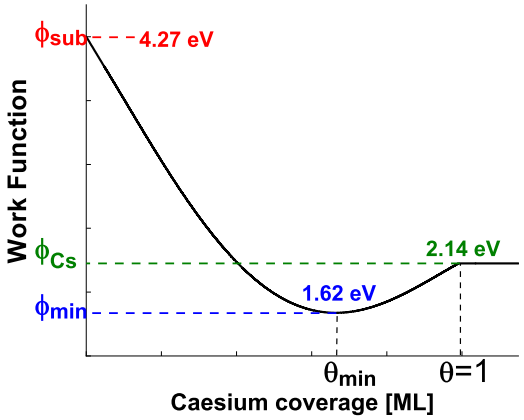

Figure 2.5: Schematic of the work function of a molybdenum surface as a function of the Cs coverage expressed in monolayer [29].

In negative ion sources for fusion, the flux and energy of atoms and positive ions (see reactions 2.2 and 2.3) at the conversion surface, assuming a low work function, determine the conversion yield for the conversion of both positive ions [30] and atoms [31] into negative ions. Thus, the main contributor to the surface-produced negative ions are H atoms which are mainly created by dissociation of hydrogen molecules by electron impact ($T_e \approx 10\,eV$) [32]; the ratio between atomic to molecular density expressed as $\frac{n_H}{n_{H_2}}$ can be up to 0.4 [33].
The main destruction mechanisms of negative ions in the source are listed in table 2.2.

$H^- + e^- \rightarrow H + 2e^-$	Electron stripping
$H^- + H_x^+ \rightarrow H + H_x$ $H^- + Cs^+ \rightarrow H + Cs$	Mutual neutralization
$H^- + H \rightarrow e + H_2$	Associative detachment
$H^- + H \rightarrow e + 2H$	Non-associative detachment
$H^- + H_2 \rightarrow e + H + H_2$	Collisional detachment

Table 2.2: List of the destruction processes for the negative ions

The relevance of the different destruction processes depends on the destruction rate R of each process that is given by

$$R_{\mathrm{H}^-,k} = n_{\mathrm{H}^-} \cdot n_k \cdot X_k, \tag{2.4}$$

where n_{H^-} is the negative ion density, n_k is the density of the particle species involved in the collision and X_k is the rate coefficient of the considered process. For some of the processes mentioned in table 2.2 the rate coefficients are shown in figure 2.6 calculated for typical particle temperatures of the negative ion sources.

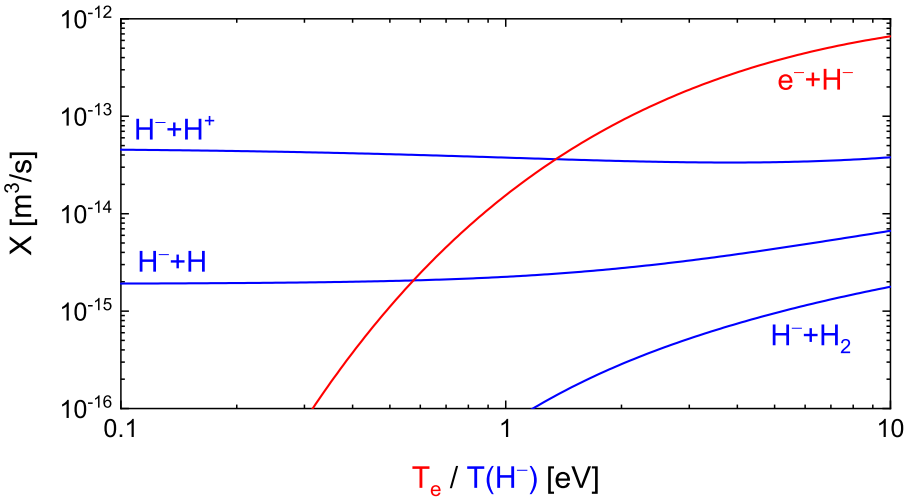

Figure 2.6: Rate coefficients for several H^- destruction processes: electron stripping in red as a function of the electron temperature (with $T_{\mathrm{H}^-} = 0.8\,\mathrm{eV}$) and the other processes as a function of the negative ion temperature ($T_{\mathrm{H}^+} = T_{\mathrm{H}} = 0.8\,\mathrm{eV}$, $T_{\mathrm{H}_2} = 650\,\mathrm{K}$). The rate coefficient for $\mathrm{H}^- + \mathrm{H}$ is the sum of associative and non-associative detachment. Cross sections obtained with a private communication with Dr. R. Janev (2011) and rate coefficients computed by Dr. Dirk Wünderlich, private communication (2020).

For the ion sources for fusion, electron stripping is the most effective destruction process for electron temperatures $T_e > 2\,eV$, thus a low electron temperature and density is needed, not only to reduce the co-extracted electrons, but also to reduce the H^- losses due to electron stripping. The mutual neutralization process with positive ions has a rate coefficient which is by one order of magnitude higher than the one of detachment with H, but it is less relevant because atomic and molecular densities ($n_H \approx n_{H_2} \approx 10^{19}\,m^{-3}$) are at least two orders of magnitude higher than the positive ion density ($n_{H_x^+} \approx 10^{17}\,m^{-3}$ and $n_{Cs^+} \approx 10^{15}\,m^{-3}$). Collisional detachment with H_2 becomes relevant only for negative ion energy above 2 eV. The cross sections used for the above considerations are listed in [34].
The source design copes with the plasma conditions required to enhance the production of negative ions and to reduce the destruction processes. In particular, to enhance the surface-produced negative ions, the ion source has to comprehend two regions, the so-called tandem concept: one region with $T_e \approx 10\,eV$ in order to dissociate the molecules into atoms and another region with $T_e \approx 1\,eV$ to minimize the destruction rate due to electron stripping. Moreover, the low electron energy and density regime is beneficial to reduce the co-extracted electrons.

2.3 Concept of a negative ion source for the ITER NBI

The plasma is generated in cylindrical volumes called drivers: the driver is a cylinder made of quartz around which the RF coil is wound. In order to protect the inner part of the driver, an actively cooled Faraday shield is installed [17]. In the design for the ITER NBI source two drivers are connected in series to one RF generator, the driver pairs are then stacked vertically (one single driver for BATMAN, four drivers in the case of ELISE, eight drivers for SPIDER and MITICA) as shown in figure 2.4. The plasma generated in the drivers ($n_e \approx 10^{18}\,m^{-3}$, $T_e \approx 10\,eV$ [35]) expands into the expansion region, namely the volume between the driver exit and the PG. In the expansion region a magnetic filter field ($\approx$ mT) is employed to reduce the electron temperature and density. The filter field is created by a current ($\approx$ kA) flowing vertically along the PG. An additional development introduced to reduce the co-extracted electrons is a positive biasing of the PG with respect to the source walls [36]. To enhance the effectiveness of the PG biasing, a bias plate, i.e. a metallic plate that encloses the aperture groups, extends the source wall potential close to the extraction apertures. The walls of the expansion region as well as the backplate,

namely the rear surface of the expansion region facing the first grid, are made out of copper coated with low sputtering yield metals (e.g. molybdenum-coated in case of ITER [10]) to reduce the sputtering due to the plasma particle bombardment. The source walls as well as the PG and bias plate are water cooled and controlled in temperature which was demonstrated to be beneficial for the temporal stability of the Cs coverage [17]. Cs is evaporated inside the source through nozzles connected to the Cs ovens located outside the source walls (one oven for BATMAN and BUG, two for ELISE and three for SPIDER and MITICA). The extraction apertures on the plasma facing side of the PG are designed with a conical chamfer to increase the available surface and to produce ions with a suitable starting angle for extraction [37]. The aforementioned elements implemented in the ELISE test facility are shown in figure 3.1 and in chapter 3 the ion source of ELISE is described in detail.

2.4 Plasma physics applied to negative ion sources

A plasma can be defined as a (partially or fully) ionized gas which is globally neutral and exhibits a collective behavior. Negative particles, usually electrons, positive particles and neutrals (atoms and molecules) in a plasma interact via collisions and electromagnetic interactions. The collective behavior of a plasma is determined by the neutrality principle: a charge imbalance as well as external electric fields are screened by the plasma within approximately one Debye length λ_D,

$$\lambda_D = \sqrt{\frac{\epsilon_0 k_B T_e}{e^2 n_e}}, \tag{2.5}$$

where k_B is the Boltzmann constant and ϵ_0 is the vacuum permittivity. The first species reacting to the electric fields are the electrons (due to the higher mobility), which in turn create a local electric field, the so-called ambipolar electric field, which pull the positive ions thus restoring quasi neutrality. The plasma frequency f_{pe},

$$f_{\mathrm{pe}} = \sqrt{\frac{e^2 n_e}{\epsilon_0 m_e}}, \tag{2.6}$$

where n_e is the electron density and m_e the electrons mass, defines the time scale for restoring the quasi neutrality.

In a low pressure plasma (0.1-1000 Pa), where the mean free path for ions and neutrals is large and the collision frequency[7] is low, the temperature of the different particle species not necessarily is identical, thus it is generally the case that the electron temperature is larger than the temperature of the other species. In the driver region of the ion sources under discussion, the RF heating mechanism is mainly targeting the electrons, thus the resulting plasma is formed by energetic electrons ($T_e \approx 10\,\mathrm{eV}$) with heavier particle, i.e. molecules, atoms and ions, with energy significantly below 1 eV.

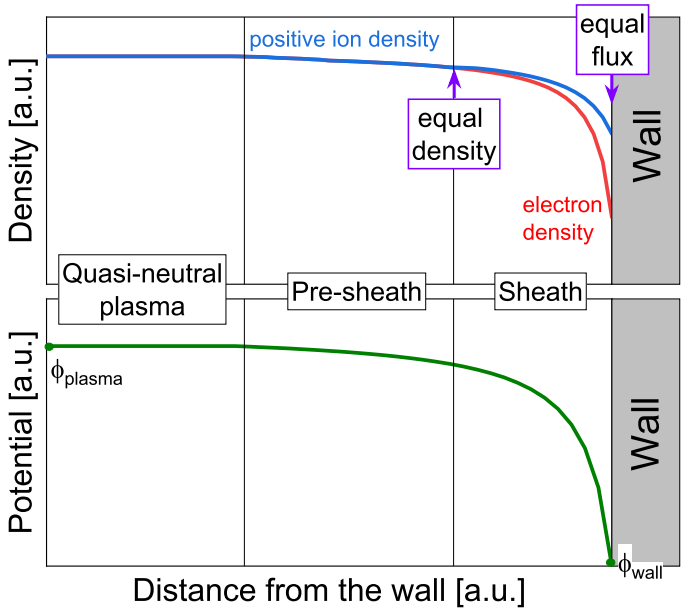

Figure 2.7: Representation of the particle density profile (top) and of the potential profile in case of plasma-wall interaction [40].

The potential difference between the wall potential and the plasma potential is determined by the electron temperature and by the quantity m_{ion}/m_e [41]:

$$\phi_{\mathrm{plasma}} - \phi_{\mathrm{wall}} = -k_B T_e ln\left(\sqrt{\frac{m_{\mathrm{ion}}}{2\pi m_e}}\right). \tag{2.7}$$

A result of the quasi neutrality kept by means of an ambipolar electric field is the formation of the sheath between the plasma and a wall: the flux of electrons towards the

[7] in this context the relevant collision frequency is the one between electrons and havier particles, i.e. H_x^+, H, H_2. The electron-ion Coulomb collision frequency is $\nu_{eH^+} = \frac{\sqrt{2}e^4 n_i (ln\Lambda)}{12\pi^{3/2}\epsilon_0^2\sqrt{m_e(k_B T_e)^3}} \approx 3.3{\cdot}10^6$ Hz. For collisions between electrons and H or H_2 the frequency is given by $\nu_{eH} = n_H \sigma_{eH} v_e \approx 1 \cdot 10^6$ Hz and by $\nu_{eH_2} = n_{H_2}\sigma_{eH_2} v_e \approx 2.5 \cdot 10^6$ Hz, respectively. σ_{eH_2} and σ_{eH} are the cross sections for the elastic collision from ref.[38]. The total collision frequency is obtained by summing the three contributions, i.e. $\nu \approx (1 + 2.5 + 6.6) \cdot 10^6$ Hz $\approx 1 \cdot 10^7$ Hz at a pressure of 0.3 Pa, a positive ion density of $2 \cdot 10^{17}\mathrm{m}^{-3}$, $T_e = 1$ eV and a Coulomb logarithm of $ln\Lambda \approx 11$[39].

wall $\Gamma_e = n_e v_e$ is dominant with respect to the flux of ions due to the higher mobility given by the lower mass. Hence, an ambipolar electric field is settled to reduce the loss of electrons at the walls. At the wall the fluxes of electrons and positive ions are equalized by establishing a potential difference between the plasma potential ϕ_{plasma} and the wall potential ϕ_{wall}, i.e. $\phi_{\text{plasma}} > \phi_{\text{wall}}$. A scheme of the potential profile and of the charged particle density profile at the wall is shown in figure 2.7. The region, where the quasi neutrality is not fulfilled, is called sheath and it extends for some Debye lengths from the wall.

The positive PG biasing is controlled in current, thus the equilibrium of the integrated flux over the PG is shifted from the value of current of 0 A[8], due to the establishment of the sheath at the surface, to a positive value I_{bias} driven by a power supply. The PG biasing controlled in current, instead of in voltage, is operationally more stable and safe because it avoids current overshooting, e.g. at plasma ignition. The potential U_{bias} applied to the PG by the power supply is measured. Different potential profiles can be established at the PG: at low or no biasing of the PG, the sheath regime is electron repelling, i.e. $U_{\text{bias}} < \phi_{\text{plasma}}$, whereas a strong biasing of the PG results in an electron attracting sheath, i.e. $U_{\text{bias}} > \phi_{\text{plasma}}$. The two regimes are schematized in figure 2.8, where the resulting electric field $\vec{E}$ is also shown.

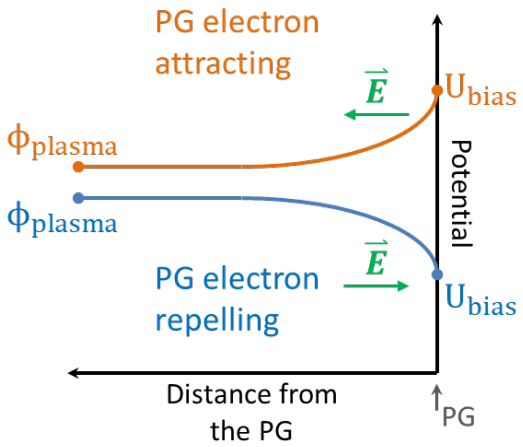

Figure 2.8: Scheme of the potential profile at a surface when a biasing is applied. If the bias is low (blue case), the case is qualitatively similar to a normal sheath whereas for high bias (orange) the wall potential is higher than the plasma potential. In green the resulting electric field is shown.

2.4.1 Magnetic field

The presence of a magnetic field B, created by a current flowing along the PG, affects the charged particle trajectory due to the Lorentz force perpendicularly to the magnetic field and to the velocity vector. The resulting trajectory of the charged

[8]The net current is given by the net flux multiplied by the area of the PG, namely $I = \Gamma \times A_{\text{PG}}$

particles is a gyration around a point, called guiding center, with radius r_{L}, called Larmor radius, and a frequency ω_{c}, called cyclotron frequency[9]:

$$r_{\mathrm{L}} = \frac{mv}{|q|B} = \frac{\sqrt{2mk_BT}}{|q|B} \tag{2.8}$$

$$\omega_{\mathrm{c}} = \frac{|q|B}{m} \tag{2.9}$$

where k_B is the Boltzmann constant and all the other quantities are related to the charged particle under investigation. A quantitative criterion for discerning if a particle species is magnetized is given by the ratio between the cyclotron frequency f_{c} and the collision frequency[10] $\nu_{\mathrm{coll}} \approx 10^7\,\mathrm{Hz}$ is larger than one ($f_{\mathrm{c}}/\nu_{\mathrm{coll}} > 1$), namely when the particle completes at least one gyration around the field line before one collision occurs. For a typical magnetic field of 3 mT, electrons with T_e=1 eV, r_{L}=1.1 mm (ω_{c}=84 MHz) and for positive ions with T_{H^+}=0.8 eV, r_{L}=4.3 cm (ω_{c}=46 kHz). If the plasma is partially or fully magnetized, namely at least one or all the species are magnetized, the presence of the magnetic filter field makes the plasma properties anisotropic: perpendicular to the magnetic field direction the diffusion of particles is reduced, since it is determined only by collisions. In the case of the RF-driven ion sources for fusion with a pressure of 0.3 Pa and with a typical magnetic field of B=3 mT, the electrons in the expansion region are magnetized, whereas the positive ions are not.

Fluid models [41] can be used to describe the dynamics of a plasma assuming that every particle species (electrons, neutrals, positive ions, etc.) is modeled by a single fluid. The single fluids are interpenetrating and interact among each other through collisions and/or electromagnetic interactions. The properties of the single fluid, such as velocity, momentum, energy are averaged over the particle distribution. The dynamic of a particle species in the plasma is described by the following fluid equation [41]:

$$mn\frac{d\vec{u}}{dt} = -\nabla p - en\vec{u} \times B - mn\nu_{\mathrm{coll}}\vec{u} \tag{2.10}$$

where $\vec{u}$ is the averaged fluid velocity, $p = nk_BT$ is the pressure determined by the thermal velocity T and ν_{coll} is the collision frequency. From this equation, the diffusion

[9] value given in rad/s, the value in Hz can be obtained by dividing by 2π

[10] in this context the relevant collision frequency for electrons is the one with heavier particles, i.e. H, H_2 and H_x^+. For positive ions the relevant collisions are the Coulomb collisions with electrons, i.e. $\approx 3.3 \cdot 10^6$ Hz whereas the collision frequency for mutual neutralization is of the order of $1 \cdot 10^4$ Hz, thus negligible.

coefficients along ($D_\parallel$) and across ($D_\perp$) the magnetic field lines can be derived [41]:

$$D_\parallel = \frac{k_B T}{m\nu_{\text{coll}}} \tag{2.11}$$

$$D_\perp = \frac{D_\parallel}{1 + \frac{\omega_{\text{ce}}}{\nu_{\text{coll}}}} \tag{2.12}$$

The magnetic field reduces the diffusion across the field lines: the more intense the magnetic field, the larger the electron cyclotron frequency ω_{ce}, thus the lower the diffusion across the magnetic field lines.

2.4.2 Plasma drift

In the RF ion sources for fusion, a vertical asymmetry of the plasma density has been observed experimentally, e.g. in the prototype source BATMAN [42] and in numeric simulations [43], only in presence of a magnetic field. Thus, the vertical asymmetry in the plasma density and potential is caused by $\times B$ plasma drifts [43]. The relevant drifts for the ion source are described in the following.
A magnetic field $\vec{B}$ combined with a generic perpendicular force $\vec{F}$ generates a drift of the guiding center for the magnetized particles with the velocity:

$$\vec{v}_D = \frac{\vec{F} \times \vec{B}}{qB^2} \tag{2.13}$$

where q is the charge of the particles subjected to the drift. The drift velocity is perpendicular to the direction of the magnetic field and of the acting force. In the negative ion source the plasma drift directly affects only the electrons as they are the only magnetized species in the expansion region. However, due to the ambipolar field, also the positive ions are influenced, thus the whole plasma is affected by the plasma drifts.
A particular case of equation 2.13 is when $\vec{F} = q\vec{E}$, where $\vec{E}$ is an electric field. In this case the drift velocity is

$$\vec{v}_D = \frac{\vec{E} \times \vec{B}}{B^2} \tag{2.14}$$

and it is independent on the charged particle.
The diamagnetic drift is defined in a fluid description and acts perpendicularly to the pressure gradient and to the magnetic field lines. The drift velocity is defined as:

$$\vec{v}_{\nabla p} = -\frac{\vec{\nabla} p \times \vec{B}}{qnB^2} \tag{2.15}$$

where p is the pressure, n the particle density and q the charge.
In the ion source, different plasma drifts give a vertical asymmetry over the ion source height:

- The temperature and density gradients of the electrons between the driver region and the expansion region give rise to a diamagnetic drift which affects mainly the fluxes of electrons [43], thus the vertical spatial distribution at the PG. This drift is relevant where the pressure gradient is enhanced, namely at the driver exit.

- Electric fields in combination with the magnetic field give a $E \times B$ drift which affects the electrons, since they are the only magnetized species, thus resulting in a vertical asymmetry. In the expansion region the electric field is created by the different electron density in the drivers with respect to the expansion region whereas at the PG, the biasing of the PG can give an additional electric field, whose direction is determined by the sheath regime (see figure 2.8).

2.4.3 Negative ion emission

The emission of negative ions from the conversion surface complicates the physics in the vicinity of the plasma grid: negative ions replace electrons preserving the neutrality of the plasma. For high negative ion emission at the surface a potential well, namely an inversion of the potential curve, can be formed within the sheath region [40], to equalize the fluxes of particles at the wall. In figure 2.9 a sketch of the charged particle density in the case of surface emission and of the potential profile is shown. In presence of a potential well the flux of negative ions from the wall towards the bulk plasma is limited and, if the potential well is too deep with respect to the bulk plasma potential, negative ions are not emitted into the plasma. The depth of the potential well is determined by the equilibrium of fluxes of charged particles at the wall and by the quasi neutrality principle in the pre-sheath region. If, for example, the positive ion density in the bulk plasma is too low, thus space-charge limiting the negative ion density, then the potential well shape will be such as to limit the emission of negative ions from the wall. A quantitative description of the potential well structure can be achieved by using kinetic models which describe the dynamics of single particles, thus computationally expensive for a high amount of particles [44][45].

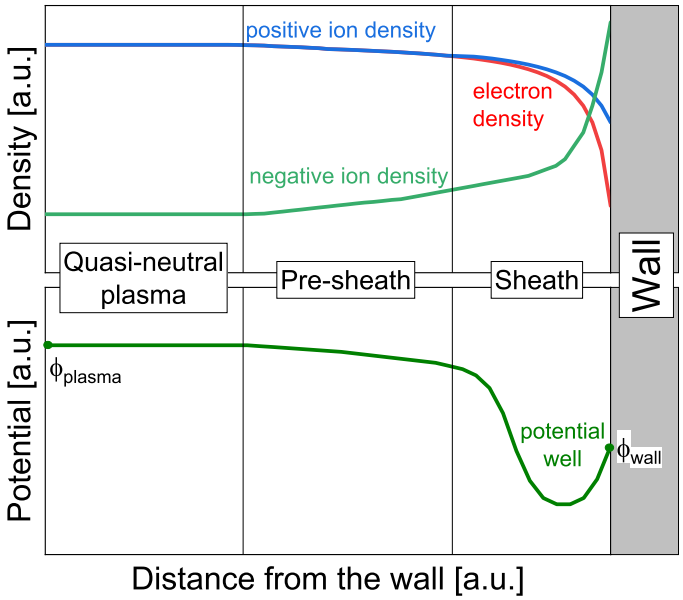

Figure 2.9: Representation of the particle density profile (top) and of the potential profile in case of plasma-wall interaction and emission of negative ions from the wall [40].

2.4.4 Plasma parameters and particle fluxes

The particle flux towards the PG is determined for the charged particles by the density and by the potential profile at the PG and for the neutral plasma species, i.e. atomic and molecular hydrogen and neutral Cs, by the density and the species temperature. Typical particle densities and temperatures in the vicinity of the PG for the ELISE test facility are reported in table 2.3. The electron temperature and positive ion density have been measured with Langmuir probes [46] (by assuming a ratio $n_{H^+} : n_{H_2^+} : n_{H_3^+} = 1{:}1{:}0.5$), negative ion density and atomic Cs density are measured with laser diagnostics techniques [47][48][49]. From optical emission spectroscopy the atomic to molecular density ratio is retrieved as well as the molecular hydrogen temperature [16]. The temperature of H and H^+ is higher than the one of H_2, since energy is gained during the dissociation process [50]. For both species the estimated value of the temperature is 0.8 eV. The temperature of the negative ions produced at the surface is estimated to be 0.8 eV [50]. From the values in table 2.3, the mono-directional fluxes ($\Gamma_i = 1/4 v_i n_i$) towards the PG can be assessed: $\Gamma_{\text{atoms}} = 2.5 \cdot 10^{22}\,\text{m}^{-2}\text{s}^{-1}, \Gamma_{\text{e}} = 7 \cdot 10^{21}\,\text{m}^{-2}\text{s}^{-1}, \Gamma_{\text{H}^-} = 3 \cdot 10^{20}\,\text{m}^{-2}\text{s}^{-1}, \Gamma_{\text{H}^+} = 3 \cdot 10^{20}\,\text{m}^{-2}\text{s}^{-1}$ and $\Gamma_{\text{Cs}} = 2.5 \cdot 10^{17}\,\text{m}^{-2}\text{s}^{-1}$.The negative ions are produced mainly from atoms, apart from the rate coefficient of the surface production process, since the flux is two orders of magnitude higher than the one of positive ions. The density of electrons, and in turn the flux, is strongly dependent on the amount of negative ions, since they are replaced

Parameter	Value
n_{H_2}	$2 \cdot 10^{19}\,\mathrm{m}^{-3}$
n_H/n_{H_2}	0.4
n_{Cs^0}	$0.5 - 1 \cdot 10^{15}\,\mathrm{m}^{-3}$
n_+	$0.5 - 2 \cdot 10^{17}\,\mathrm{m}^{-3}$
n_{H^-}	$0.1 - 2 \cdot 10^{17}\,\mathrm{m}^{-3}$
$n_e \approx n_+ - n_{H^-}$	$5 \cdot 10^{16}\,\mathrm{m}^{-3}$
T_e	1 eV
T_{H_2}	0.1 eV
$T_H \approx T_{H^+} \approx T_{H^-}$	0.8 eV

Table 2.3: Plasma parameters in the vicinity of the PG for the ELISE ion source for typical operational parameters [16].

to keep the quasi neutrality. An adequate amount of Cs at the PG is necessary to have a low work function for an efficient production of negative ions and the suppression of electrons. The connection between beam homogeneity and homogeneity of the particle fluxes towards the PG needs localized knowledge of the particle fluxes, namely measurements of density and temperature with a certain spatial resolution. Whereas the temperature and density of neutral species, e.g. hydrogen atoms, can be considered fixed, the flux of charged particles towards the PG is determined by the potential profile, which can vary locally due to the plasma drifts.

The extracted negative ion current of the ion source, given a fixed particle flux, is determined by the efficiency of the negative ion production at the PG, namely by the work function at the PG. Negative ions are efficiently produced at any surface of the ion source where the work function is low enough and the destruction mechanisms are minimized, but the survival length for negative ions in plasma is of the order of cm [51]. Thus, only negative ions produced at the surfaces surrounding the apertures, i.e. PG and a portion of the bias plate, are extracted.
The PG work function is determined by the Cs layer deposited on it. The operational routine is made of different phases and the Cs layer is affected differently according to the phase.

- During the vacuum phase between pulses the background pressure is low, i.e. 10^{-4} Pa, so the Cs deposition and dynamics are determined by the spatial properties of the Cs oven evaporation.

- During the plasma phase the Cs transport is determined by collisions and, due to collisions, Cs can be ionized. Positive Cs ions are then affected by the magnetic field. Removal of Cs from the ion source surfaces during the plasma phase is determined by the plasma erosion, mainly sputtering from positive hydrogen ions.

- During the HV phase, in addition to the dynamics already described in the plasma phase, positive ions which are created within the grids are back-accelerated and can sputter Cs from the backplate. The Cs removed from the backplate can contribute to the Cs layer on the PG.

A detailed description of the Cs dynamics for the ion sources for fusion is given in reference [52]. The work function or the thickness of the Cs layer are not accessible quantities at the ion sources, but the amount and the temporal instability of the co-extracted electrons or of the extracted negative ions depend on the work function value at the PG. The sheath at the conversion surface is also determined by the work function, because the negative ion flux from the PG is determined by the work function.

2.5 Extraction and acceleration of a multi-beamlet beam

In correspondence of the PG apertures the charged particles are affected by the extraction potential: negative ions and electrons are extracted, then the former form the beamlets, the latter are dumped onto the EG. Positive ions are pushed back into the plasma. The interface between the neutral plasma and the beamlet (net negative charges) is called meniscus: plasma particles that reach the meniscus are accelerated from the plasma into the grids if negatively charged or accelerated back into the plasma if positively charged. The meniscus shape is defined by the equilibrium between the plasma diffusion forces and the electric field force generated by the extraction potential.
A schematic view of the meniscus shape and of the the beamlet profile is shown in figure 2.10.

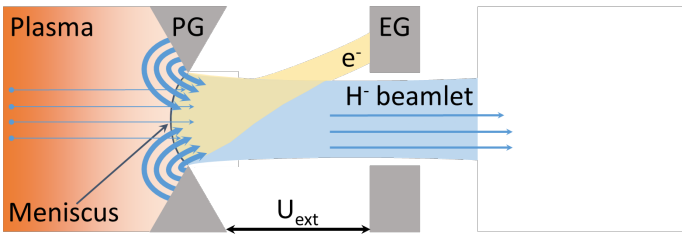

Figure 2.10: Schematic of the extraction of a beamlet. The majority of the extracted negative ions are surface produced, volume produced negative ions are also extracted as well as electrons from the plasma which are then dumped onto the EG.

The meniscus shape can be modified by acting on the plasma diffusion forces: since the thermal velocity of the plasma species is fixed at fixed pressure, the plasma pressure can be modified by changing the particle density or the collisionality, i.e.

acting on the pressure. Since the pressure is fixed by the ITER requirements, to act on the meniscus the negative ion density in the plasma can be changed, thus affecting the extracted current density. The total extracted current density can be limited by the Child-Langmuir law, which is explained in the following, and in this case an increase of negative ion density in the plasma does not lead to an increase of the extracted current density. This is not the case for the negative ion sources for fusion, since the extracted current density is generally about 30% of the maximum achievable value. The meniscus is influenced also by the electric field applied for extraction, namely by the extraction voltage U_{ext}. The maximum current that can be extracted from a circular aperture of radius a by applying a potential difference U_{ext} to two infinitely extended planar surfaces separated by a distance d is given by the Child-Langmuir law [53]:

$$I_{\max} = j_{\max}\pi a^2 = \frac{4\epsilon_0}{9}\sqrt{\frac{2e}{m}}\frac{\pi a^2}{d^2}U_{\text{ext}}^{3/2} \tag{2.16}$$

where a is the aperture radius, m the ion mass and e the charge unit. This maximum in current is determined by the space charge limit that, solving the Poisson equation, gives a space potential which limits the charged particle density. The meniscus shape is related to the source performance through the concept of perveance P:

$$P = \frac{I_{\text{ext}}}{U_{\text{ext}}^{3/2}} \tag{2.17}$$

where I_{ext} is the extracted current and U_{ext} is the extraction voltage.
In order to compare different extraction systems, the concept of normalized perveance is introduced:

$$P/P_0 = \frac{\frac{I_{\text{ext}}}{U_{\text{ext}}^{3/2}}}{\frac{4N\pi\epsilon_0}{9}\sqrt{\frac{2e}{m}}\left(\frac{a}{d}\right)^2} \tag{2.18}$$

where the denominator is the total maximum extractable current according to equation 2.16, taking into account the N apertures of the extraction system, the ion mass m, the aperture radius a and the distance d between PG and EG. For the ion sources for fusion, the value P/P_0 is always below one.

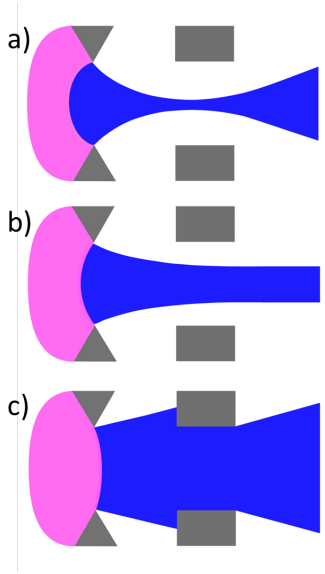

Figure 2.11: Beamlet profile as a function of the meniscus shape: a) strongly concave meniscus causes a divergent beamlet; b) optimal case with a slightly concave meniscus and a parallel beamlet; c) convex meniscus causes a divergent beamlet that may lead to beamlet scraping.

The meniscus shape influences the width of the angular distribution of the extracted negative ions, namely the beamlet divergence. The entering particles cross the meniscus surface perpendicularly: a slightly concave meniscus is desirable in order to have a parallel beam and minimize the beamlet divergence. A diagram of the beamlet shape as a function of the meniscus shape is shown in figure 2.11: in case *a)* the meniscus is strongly concave and deeply penetrates into the plasma being the electric field much stronger than the plasma diffusion force; in case *b)* the meniscus profile and the beamlet divergence are optimal; case *c)* represents the case in which the electric field is not sufficient to compensate the plasma diffusion forces and, consequently, the meniscus is convex. Under certain circumstances the beamlet may impinge on the EG (beamlet scraping).

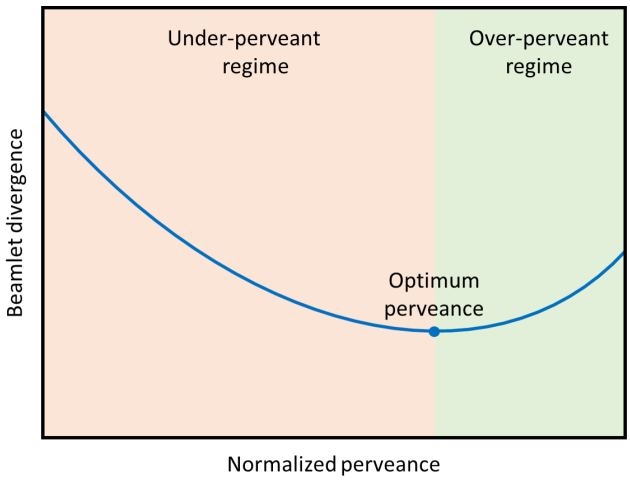

Figure 2.12: Qualitative sketch of the beamlet divergence as a function of the perveance. The shaded areas highlight the different regimes: the under-perveant case, the optimum perveance case and the over-perveant case.

The optimum normalized perveance is defined as the value which minimizes the beamlet divergence. For values below or above the optimum, the beamlet is defined as under-perveant or over-perveant, respectively. The normalized perveance can be

changed by varying the extracted current density or the extraction potential. The evolution of the beamlet divergence as a function of the normalized perveance is schematized in figure 2.12. The over-perveant regime is not always experimentally observable because the beam can be scraped on the EG, thus the angular distribution is cut.

The acceleration gaps, namely the gaps between EG and GG, play an important role in focusing the beamlets: in general, an aperture with a different electric field strength on the two sides works as an electrostatic lens. The focal length f of such lens, described as a function of the upstream electric field E_u and of the downstream one E_d, is defined as [54]

$$f = \frac{4V}{E_d - E_u} \tag{2.19}$$

where V is the ion energy at the lens position (in volts).

The averaged beam particle velocity is given by the equation 2.20 and it depends on the total HV applied to the grid system and to the negative ion mass m.

$$v = \sqrt{\frac{2eU_{HV}}{m}} \tag{2.20}$$

The initial velocity of the negative ions at the meniscus ($\approx 1\,\mathrm{eV}$) is negligible with respect to the energy gained through the electrostatic acceleration in the grid system. Nevertheless, a perpendicular component of the velocity with respect to the beamlet axis causes a broadening of the beamlet divergence.

Within the grid system beam particles can collide with the background gas particles and negative ions can be neutralized before full acceleration. The velocity of the neutralized particles depends on the energy gained up to the position where the collision takes place. The stripped electron can impinge on the grids or downstream the grid system on the tank, namely the vessel enclosing the beam.

After the last grid, the beamlets undergo space charge compensation which prevents the fast increase of the beamlet divergence due to the electrostatic repulsion among the negative ions [55]. The space charge neutralizing particles, i.e. positive ions for negative ion beams, are produced by collisions of the beam particles with the background gas, thus the space charge compensation depends on the background gas density and on the beamlet current density [54].

The beam is made of multiple beamlets and the beam power density profile mimics the arrangement of the apertures in the grid system. With increasing distance from the last grid, the beamlet width increases and the beamlet power density decreases. Beamlet overlapping, namely the superposition of the beamlet power profiles, becomes

significant at large distance from the last grid and depends on the spacing between beamlets and on the single beamlet divergence. The filter field is still present downstream of the grid system, thus influencing the particle trajectory due to the Lorentz force. The acceleration $\vec{a}$ that the beam particles with velocity $\vec{v}$ and mass m undergo due to a magnetic field B can be written as

$$\vec{a} = \frac{q}{m}\vec{v} \times \vec{B} \tag{2.21}$$

The total beam deflection calculated at one fixed position along the beamline is an integrated value over the particle velocity perpendicular to the magnetic field and over the magnetic field strength. The final value depends on the particle mass and velocity, the magnetic field strength and, if the negative ion is neutralized, the position in which the neutralization takes place.

3 The ELISE test facility

In this chapter technical details of the ELISE test facility will be given together with the experimental setup, diagnostic systems installed, and data analysis techniques.

3.1 Description

In figure 3.1 a CAD drawing of the ELISE ion source is shown and the essential elements of the ion source are pointed out. The ion source is equipped with two pairs of drivers connected in series to two RF generators that can deliver up to 150 kW RF power per couple of drivers. The source walls are coated with nickel or molybdenum, in particular, the bias plate and the PG are coated with molybdenum [17]. At ELISE the filter field in the expansion chamber is oriented towards the positive horizontal axis using the reference system shown in figure 3.1 and it is generated by a current, called I_{PG} current ($<$5 kA), flowing vertically from the bottom to the top along the PG. At two cm axial distance from the PG, an I_{PG} of 1 kA corresponds to a filter field strength of 0.95 mT.

Two Cs ovens are placed sideways the ion source with the nozzles sticking into the two vertical sidewalls and pointing towards the backplate. The plasma grid is positively biased against the source walls by a power supply which is controlled in current (I_{bias}) and the resulting biasing voltage of the PG (U_{bias}) is measured. The extraction of negative ions takes place at the 640 apertures of the PG: the extraction and acceleration system in ELISE is made of three grids with a total high voltage (U_{HV}) up to 60 kV. The extraction gap is of 6 mm with an extraction voltage (U_{ext}) up to 12 kV whereas the acceleration gap is of 15 mm. The acceleration potential (U_{acc}) can be up to the remaining part of the total HV [19].

The apertures are arranged in eight vertically elongated beamlet groups with five columns of 16 apertures each. The grids are divided into two segments stacked vertically, each one hosting four beamlet groups. The arrangement of the apertures is shown in figure 3.2, the projection of the drivers and the window-framed bias plate in

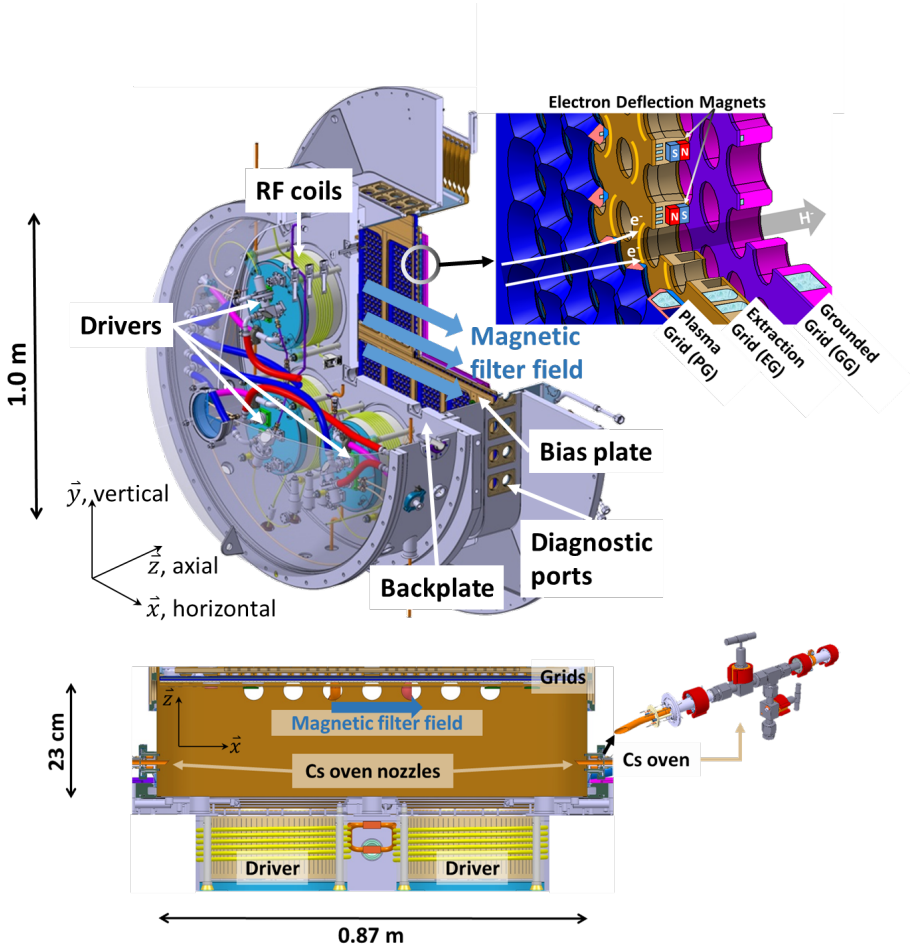

Figure 3.1: Top: schematics showing the ion source and grid system at the ELISE test facility, some of the main components are highlighted; a detail of the extraction and acceleration system is shown. Bottom: horizontal cut, top view of the ion source with the Cs nozzles visible; a sketch of the Cs oven is shown.

front of the PG are also shown. The two grid segments of the EG and GG are electrically insulated thus providing individual electrical measurements of the impinging current. Other components downstream of the GG are electrically insulated, such as the grounded-grid grid holder box (GGGHB), which is connected to the electrostatic shield that extends the ground potential into the HV ring to shield the beam from other potentials [17]. The design of the grid system is based on the SINGAP concept [56] with modifications for both PG and EG to maximize the extracted negative ion current density at about 10 kV extraction voltage [57] and allowing a higher power load on the EG through better cooling of the grid. The RF-sustained plasma can run in steady-state whereas the extraction phase is up to 9.5 s every $\approx$ 150 s due to limitations of the HV power supply. A typical pulse scheme is shown in figure 3.3: the plasma is initially ignited at higher pressure and lower power, i.e. $p_{\mathrm{fill}} \approx 1$ Pa and

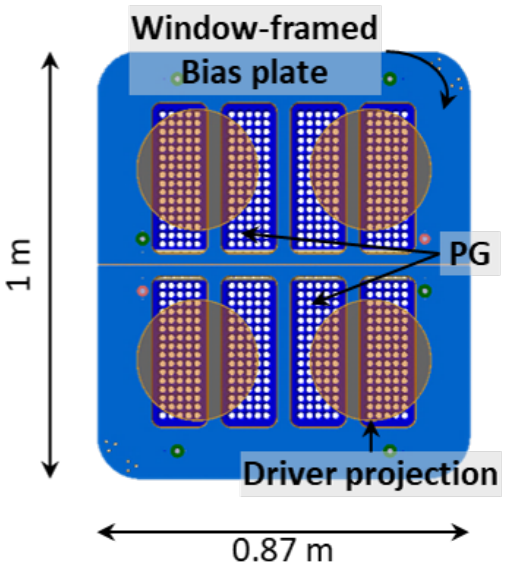

Figure 3.2: View of the plasma-facing side of the PG partially covered by the bias plate. The arrangement of the extraction apertures in the eight beamlet groups is shown. The large circles represent the projection of the four drivers on the grid system.

$P_{\mathrm{RF}} \approx 40\,\mathrm{kW/generator}$, then the pressure and the RF power are set to the desired operational values. When stable plasma conditions are reached, HV is applied to the grid system and the beam is extracted. After the beam phase, plasma is still running for about 6 seconds.

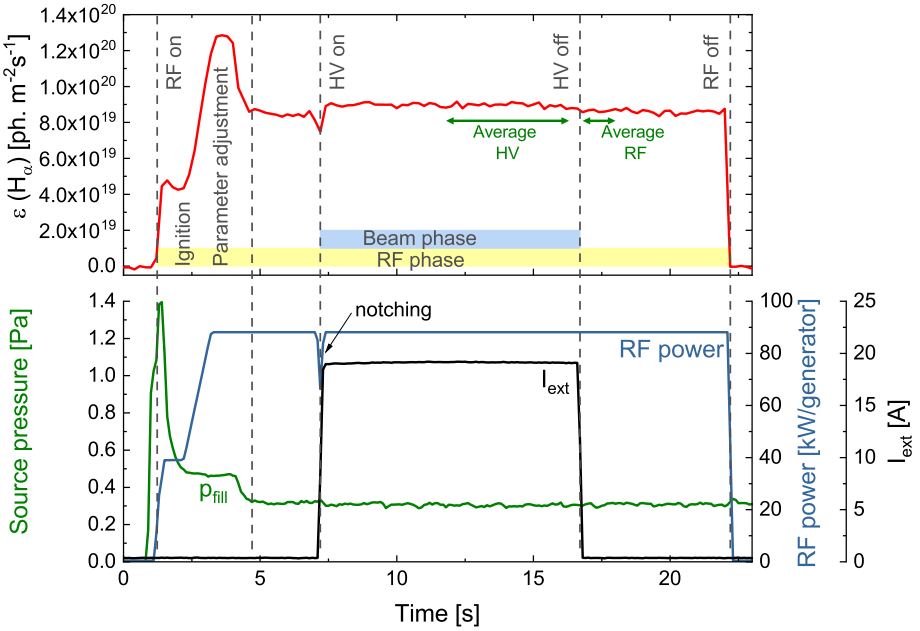

Figure 3.3: Time-trace of the H_α emission measured close to the PG. The switching on and off of the RF and HV system is highlighted as well as the plasma ignition phase. The time intervals for the signal averaging are shown with arrows. At the bottom, the time-traces of the source pressure, RF power coupled and extracted current are shown.

The averaging of signals from electric measurements or diagnostic systems is performed for two time intervals during the HV phase and RF phase after the beam extraction: the time intervals for the averaging are shown in figure 3.3. In the rest of the thesis, the single value for RF and HV phase are the averaged values in the time intervals shown.
The beam is dumped onto a diagnostic calorimeter placed at 3.5 m distance from the GG. The pressure in the tank is around $p_{tank} = 0.001 - 0.005$ Pa during the pulse.
The range of the operational parameters of the present setup of the ELISE test facility is listed in table 3.1.

Total HV ($U_{ext} + U_{ext}$)	60 kV
Total RF power (two generators)	up to 300 kW
RF frequency	≈ 1 MHz
I_{PG} current	≤ 5 kA
I_{bias} current	≤ 250 A (up to 60 V)
Extraction area	0.1 m^2
Source and grid filling pressure	0.2 Pa – 1 Pa
Beam pulse length	9.5 s every ≈150 s

Table 3.1: Operational parameters of the ELISE ion source and extraction system[19]

3.2 Diagnostic techniques for plasma and beam

In this section an overview of the diagnostic systems that are applied to study the plasma and beam properties at ELISE is presented. Diagnostic systems for RF sources and ion beams need to work in a harsh environment due to the presence of RF noise, the high voltage applied to the source, and, on the beam side, highly localized power density. Moreover, the experimental access to the areas of interest is limited to the diagnostic ports available, relevant measurements at the PG surface, e.g. the work function, are not possible as well as localized measurements over the PG, e.g. of the atomic flux onto the PG.

3.2.1 Plasma diagnostic techniques

At ELISE, several diagnostic ports are located on the source walls of the expansion vessel, on the source backplate and the back of the drivers: a technical drawing with the ports available at ELISE ion source is shown in figure 3.4 with the relative

nomenclature of the ports: the first character (X, Y or Z) indicate that the line-of-sight (LOS) is parallel to the x, y or z axes, respectively (reference shown in figure 3.1). The second character indicates whether the port is positioned in the bottom (B), in the top (T), left (L) or right (R) side of the expansion vessel. For panel *c)* B indicates the position of the port in the backplate whereas D in the driver. The third character is the relative position of the port: in panel *a)* from -3 to 3 is the positioning from top to bottom or from left to right. For the drivers: 1 is the top left driver and 4 is the bottom right driver. The fourth character in panel *a)* indicates whether the port is upstream U or downstream D the PG whereas in panel *c)* whether the port is on the top (T), bottom (B) or center (C) of the corresponding driver. Ports located downstream the PG looks into the beam. The axial distance of the center of the ports positioned upstream the PG is of about 2 cm axial distance from the PG. More details on the diagnostic ports are reported in reference [58]. Any combination of diagnostics can be installed at these ports, though the installation of multiple diagnostics at one port is not possible.

Not all the ports can be used for diagnostic purposes: for example, YB-2U, YB0U, YB+2U, and the corresponding upper ports are used for the installation of the potential rods.

Diagnostic techniques applied at ELISE to the plasma region are optical emission spectroscopy (OES), cavity ring-down spectroscopy (CRDS), tunable diode laser absorption spectroscopy (TDLAS) and Langmuir probes (LP). Cameras in the visible range qualitatively monitor the evolution of the plasma pulse.

A brief description of the diagnostics techniques with the salient information follows.

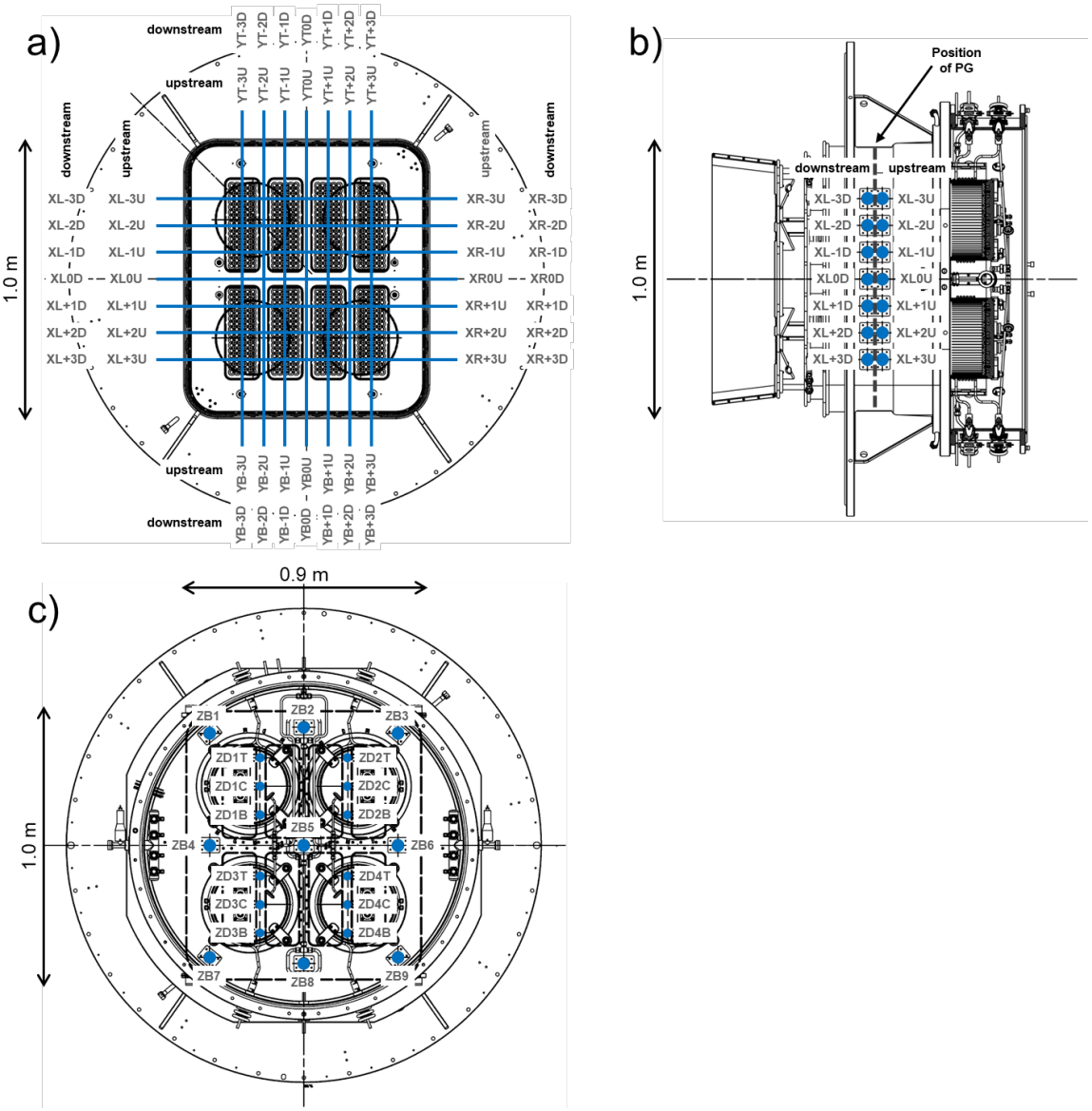

Figure 3.4: Arrangement of the diagnostic ports at the ELISE ion source [58] and the relative nomenclature. *a)* Front view of the ports and paths of the lines of sight highlighted; *b)* lateral view (left side) of the upstream and downstream ports; *c)* View of the back of the source where the ports on the back of the driver and on the backplate are shown.

Optical emission spectroscopy

OES is a diagnostic based on the spectral analysis of the light spontaneously emitted by the plasma. At ELISE, the experimental apparatus consists of lens heads which collect the light in a collection cone spreading up from 5.5 mm, i.e. the aperture size of the lens heads, to approximately 8 mm along the path from the lens head to the opposite port opening where a black dump is installed to avoid reflections (see figure 3.4). The light collected is conveyed through fibers to multi-channel spectrometers (PLASUS EMICON MC system, $\lambda = 180 \ldots 880$ nm, sampling rate <15 Hz). The signal is line-of-sight (LOS) integrated, namely it is not possible to have spatial resolution along the LOS. Several lines of sight are anyway installed to have spatial resolution perpendicularly to the LOS orientation. To provide the absolute intensity of the spectral lines in the interested spectral range, OES requires an absolute calibration of the entire setup. The emissivity of one specific line ε_i, i.e. the number of photons emitted per time, is calculated from the signal counts s_i by

$$\varepsilon_i = \frac{\mathrm{Calib}_i \, s_i}{l_{\mathrm{pl}} \, t_{\mathrm{exp}}} \tag{3.1}$$

where Calib_i is the calibration factor for the specific line i, l_{pl} is the plasma length and t_{exp} is the exposure time. The calibration factor is different for every combination of fiber, spectrometer channel and spectral line because the signal transmissivity of the fibers, the sensitivity of the chip over the spectral interval and the chip itself can be different for every LOS.

The standard set of lines or bands for which the emissivity is automatically calculated are the Balmer lines H_α, H_β, H_γ, Fulcher band of molecular hydrogen ($d^3 \rightarrow a^3$), the caesium line at 852 nm (resonant transition $6^2\mathrm{S}_{1/2} \rightarrow 6^2\mathrm{P}_{3/2}$), the atomic oxygen line at 777 nm ($5^2\mathrm{S}_2 \rightarrow 5^2\mathrm{P}_{1\ldots3}$), and three copper lines around 515 nm ($4^2\mathrm{D}_{5/2} \rightarrow 4^2\mathrm{P}_{3/2}$, $4^2\mathrm{P}_{1/2} \rightarrow 4^2\mathrm{D}_{3/2}$ and $4^2\mathrm{P}_{3/2} \rightarrow 4^2\mathrm{D}_{5/2}$)[58]. The rotational and vibrational structure of the molecular Fulcher band can not be resolved, thus a detailed evaluation, i.e. determination of the rotational and vibrational temperature, is not possible with this spectrometers. The most intense emission is the one of the Balmer lines and the error bars for the absolute emission is of about 6% on H_α and H_β and of about 12% on H_γ [59]. The emission of the Balmer lines and the Fulcher band can be used, coupled with population models [60] to backward calculate the plasma parameters.

The intensity ε_{pq} of an emission line between two states $p \rightarrow q$ is correlated to the population density n_p of the excited state p by the respective transition probability A_{pq}, i.e. $\varepsilon_{pq} = n_p A_{pq}$. Population models predict the population density of excited

states, i.e. n_p, of atoms and molecules depending on plasma parameters, such as the temperatures of the considered species as well as the electron density and temperature, together with the transition probabilities and cross-sections of the involved processes. The types of population model that are appropriate for the description of the plasma in the ELISE ion source are collisional radiative (CR) models, which are generally applied to plasmas with a collision rate too high for corona models and too low for the (local) thermodynamic equilibrium (LTE) [60].

As an example for the case of atomic H, the density n_p of a state p (see rate equation 3.2) is given by the different process populating or de-populating the state p, e.g. by spontaneous emission from or into another state q (in red), excitation or de-excitation via electron collisions from or into a state q (in blue), radiative or three-body recombination (in green) and ionization (in orange).

$$\frac{d(n_p)}{dt} = \sum_{q>p} A_{qp} n_q - \sum_{q<p} A_{pq} n_q + n_e \left(\sum_{q \neq p} X_{qp} n_q - \sum_{p \neq q} X_{pq} n_p + (\alpha + \beta n_e) n_+ - S_p n_p \right) \tag{3.2}$$

where A_{ij} is the transition probability for spontaneous emission from i to j, X_{ij} are the rate coefficients for excitation or de-excitation by electron collision, n_e is the electron density, α and β are the rate coefficients for radiative and three-body recombination of the positive ion H^+ with density n_+, and S_p is the rate coefficient for ionization of the state p. In the plasma in the ion source molecular hydrogen and heavier particles are present as well as atomic hydrogen, thus several additional excitation channels chemical reactions must be included in the model to correctly describe the population density of the excited states.

The rate equations for all excited states included into the collisional radiative model form a set of coupled ordinary differential equations (ODE). In this work this set of ODE is solved and the population density of the states is determined by direct integration using the flexible package YACORA [61]. Two different CR models are used, namely for atomic and molecular hydrogen.

For the H_2 molecule in YACORA the excited levels up to the electron state p=10 are considered, where p is the principal quantum number. Vibrational and rotational levels are not considered. The reactions considered for the H_2 model are:

- Electron collision from the ground state and inverse reactions.
- Excitation through electron collision between states and inverse reactions.
- Spontaneous emission.

- Ionization.

More details for the H_2 model implemented in YACORA are presented in reference [61].

The processes included in YACORA for the atomic hydrogen model, thus relevant to calculate the state density for the Balmer transition, are listed in table 3.2.

Short form	Process	Reaction
	excitation by e^- collision	$H(q) + e \rightarrow H(p > q) + e$
	de-excitation by e^- collision	$H(q) + e \rightarrow H(p < q) + e$
	spontaneous emission	$H(q) \rightarrow H(p < q) + h\nu$
H	ionization	$H(q) + e \rightarrow H^+ + 2e$
H^+	three body recombination of H^+	$H^+ + 2e \rightarrow H + e$
		$H^+ + e \rightarrow H + h\nu$
H_2	H_2 dissociation	$H_2(\nu) + e \rightarrow H(1) + H(p > 1) + e$
	H_2^+ dissociation	$H_2^+ + e \rightarrow H^+ + H(p) + e$
H_2^+	H_2^+ dissociative recomb.	$H_2^+ + e \rightarrow H + H(p)$
H_3^+	H_3^+ dissociative recomb.	$H_3^+ + e \rightarrow H_2 + H(p)$
$H^+ + H^-$	mutual recomb. H^+	$H^+ + H^- \rightarrow H(p) + H$
$H_2^+ + H^-$	mutual recomb. H_2^+	$H_2^+ + H^- \rightarrow H(p) + H_2$

Table 3.2: Overview of the reactions included in the CR model for the hydrogen atom. The short form is used to refer to the relative process in the following figures. References the different processes are listed in reference [61].

An example of emission calculated with YACORA with typical densities and temperatures for the species listed in table 3.3 is shown in figure 3.5 for the driver region in *a)* and for the expansion region in *b)*.

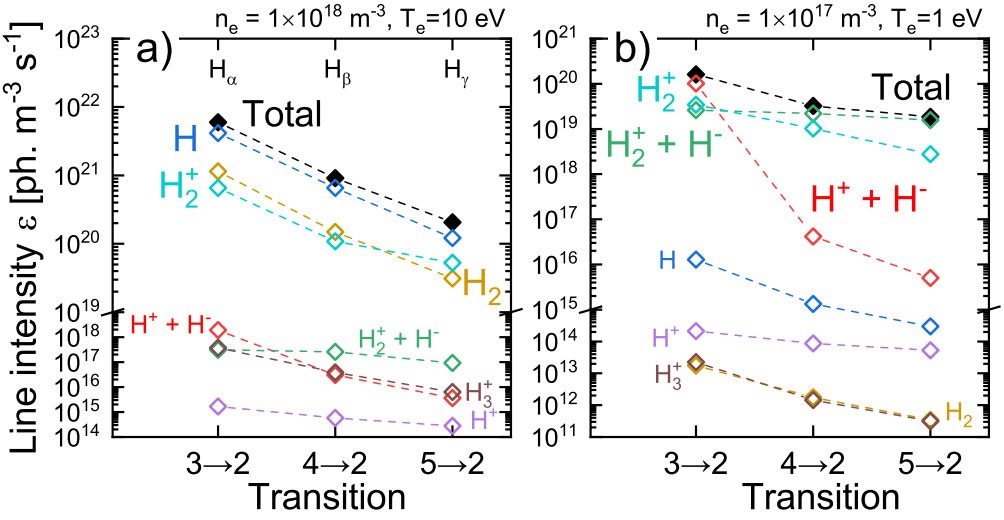

Figure 3.5: Emission for H calculated with YACORA [61] for the driver region in panel *a)* and for the expansion region in panel *b)*. The densities and species used are listed in table 3.3.

Species	Density		Temperature	
	Driver	Exp. Region	Driver	Exp. Region
e	$1 \cdot 10^{18}\,\mathrm{m}^{-3}$	$1 \cdot 10^{17}\,\mathrm{m}^{-3}$	10 eV	1 eV
H	$4 \cdot 10^{18}\,\mathrm{m}^{-3}$	$4 \cdot 10^{18}\,\mathrm{m}^{-3}$	0.8 eV	0.8 eV
H_2	$2 \cdot 10^{19}\,\mathrm{m}^{-3}$	$2 \cdot 10^{19}\,\mathrm{m}^{-3}$	0.1 eV	0.1 eV.
H^-	$1 \cdot 10^{14}\,\mathrm{m}^{-3}$	$5 \cdot 10^{16}\,\mathrm{m}^{-3}$	0.8 eV	0.8 eV
H^+	$5 \cdot 10^{17}\,\mathrm{m}^{-3}$	$5 \cdot 10^{16}\,\mathrm{m}^{-3}$	0.8 eV	0.8 eV
H_2^+	$2 \cdot 10^{17}\,\mathrm{m}^{-3}$	$2 \cdot 10^{16}\,\mathrm{m}^{-3}$	0.2 eV	0.2 eV
H_3^+	$2 \cdot 10^{17}\,\mathrm{m}^{-3}$	$2 \cdot 10^{16}\,\mathrm{m}^{-3}$	0.2 eV	0.2 eV

Table 3.3: Species temperature and density used to calculate the line intensity of H_α, H_β and H_γ for different processes as shown is figure 3.5. The molecular density is calculated with the ideal gas law $p = n_{H_2} k_B T_{H_2}$ with a pressure of 0.3 Pa and T_{H_2} from reference [62]; the atomic density is calculated from the molecular one assuming an atomic to molecular density ratio of $n_H/n_{H_2} = 0.2$

The excited states H^* connected to different particle species (e.g. H, H_2, H^+, etc.) or different excitation channels relevant for the line intensity of H_α, H_β and H_γ and the Fulcher band emission in the driver and expansion region are different:

- **Driver**: due to the high electron temperature, i.e. $T_e \approx 10$ eV, the most relevant excitation channel for atomic hydrogen emission is direct electron collision excitation from the atomic ground state. Molecular radiation is mainly caused by direct excitation of H_2. Thus, as shown in figure 3.5*b)* the emission is due to ionization (≈70%), H_2 dissociation (≈20%) and dissociative recombination (≈10%), i.e. the driver plasma is an ionizing plasma.

- **Expansion region**: the low electron temperature and electron density in the expansion region results in a negligible role of excitation processes, thus relevant processes are the recombining ones. The emission is mainly due to mutual neutralization of H^+ and H_2^+ with H^- (≈75%) and dissociative recombination (≈25%). The relative contribution of the processes to the total emission depends on the transition, e.g. mutual neutralization of H^+ with H^- feeds solely $p = 3$, i.e. the upper state of the H_α transition [63]. The impact of mutual neutralization on the other emission lines is due to population redistribution. The relative contribution of the different channels in the expansion region is shown in figure 3.5 *b)*.

The analysis of the emission of atomic hydrogen, especially in the expansion region, is not straight-forward because the plasma parameters, which mostly affect the emission, e.g. negative ion and positive ion density, are partially unknown or vary simultaneously.

In this work, the determination of the plasma parameters is performed only in the driver region and two methods are used:

- Line ratio method: in this case the knowledge of the electron temperature is a prerequisite of the analysis. Only the direct ionization process is taken into account for the calculation of the population density for the atomic H and only the dissociation process is taken into account for the calculation of the population density for the H_2 molecule. Then the emission of H_α for example is given by:

$$\varepsilon(H_\alpha) = A_{3\rightarrow 2} n_3 = n_H n_e X^H_{3\rightarrow 2}(n_e, T_e = 10\,\mathrm{eV}), \tag{3.3}$$

  and for the Fulcher band:

$$\varepsilon(\mathrm{Fulcher}) = A_{d^3\rightarrow a^3} n_{d^3} = n_{H_2} n_e X^{H_2}_{d^3\rightarrow a^3}(n_e, T_e = 10\,\mathrm{eV}), \tag{3.4}$$

  where A is the transition probability between the states and $X(n_e, T_e)$ is the effective emission rate coefficient calculated with the collisional-radiative model [64]. In equations 3.3 and 3.4 only excitation from the respective ground states is assumed.
  The electron density is estimated from the ratio

$$\frac{\varepsilon(H_\alpha)}{\varepsilon(H_\beta)} = \frac{X^H_{3,2}(n_e, T_e = 10\,\mathrm{eV})}{X^H_{4,2}(n_e, T_e = 10\,\mathrm{eV})} \tag{3.5}$$

  where the effective emission ratio $\varepsilon(H_\alpha)/\varepsilon(H_\beta)$ between the absolute line intensity is determined experimentally by using OES. For a fixed electron temperature, i.e. 10 eV in the driver, the electron density is obtained by comparing the ratio predicted by the model and the experimental one obtained by OES. Once the electron density n_e is known, the ratio between atomic and molecular density n_H/n_{H_2} is obtained from the ratio $\varepsilon(H_\gamma)/\varepsilon(H_{\mathrm{Fulcher}})$ as:

$$\frac{n_H}{n_{H_2}} = \frac{\varepsilon(H_\gamma)}{\varepsilon(H_{\mathrm{Fulcher}})} \cdot \frac{X^{H_2}_{d^3\rightarrow a^3}(n_e, T_e = 10\,\mathrm{eV})}{X^H_{5\rightarrow 2}(n_e, T_e = 10\,\mathrm{eV})} \tag{3.6}$$

  where the rate coefficient X are known from the CR model and the line emission ratio $\varepsilon(H_\gamma)/\varepsilon(H_{\mathrm{Fulcher}})$ is obtained experimentally by OES measurements.
  With this method, electron density and dissociation degree are retrieved with a relative error of about 20% [59].

- Absolute evaluation method: in this method all the excitation channels that affect the excited state population density are considered. Once the absolute line emission is known, the particle species densities are varied until a good matching is achieved between experimental line emission and calculated one. A relative error is estimated of about 30%.

Cavity ring-down spectroscopy

CRDS allows the determination of line-of-sight integrated negative ion densities, both in hydrogen and deuterium [47]: the system is based on the measurement of the decay time of a pulsed laser light (ns scale) inside a mirror cavity due to the light absorption by negative ion photo-detachment. The negative ion density is proportional to the difference between the inverse of the decay times measured in vacuum and the inverse of the decay time measured with additional plasma absorption. The range of measured values when the source is in a good Cs conditioning status is between $10^{16}\,\mathrm{m}^{-3}$ and $10^{17}\,\mathrm{m}^{-3}$ measured at 2 cm distance from the PG at the diagnostic ports XL+2U and XL-2U, i.e. along the center of the beamlet groups. The lower detection limit of the diagnostic is about $10^{14}\,\mathrm{m}^{-3}$. Typically, no significant differences in density between the two LOS is observed [47]. The relative error bars assigned to the negative ion density is about 10%.

Tunable diode laser absorption spectroscopy

In general, TDLAS is an active diagnostic method for measuring particle densities using a wavelength-tunable laser with single mode emission to induce absorption for a specific transition [48]. In ELISE this method is applied to measure the LOS-averaged ground state density of atomic Cs: the transition used in this case is $6^2\mathrm{S}_{1/2} \rightarrow 6^2\mathrm{P}_{3/2}$ [48]. Typical values measured at 2 cm distance from the PG at the diagnostic port XL+2U and XL-2U are between $1 \cdot 10^{14}\,\mathrm{m}^{-3}$ and $1 \cdot 10^{15}\,\mathrm{m}^{-3}$ [65]. No significant differences in density between the two LOS were observed. The error bar on the absolute value is about 10% of the absolute value.

Langmuir probes

Langmuir probes are devices consisting of one or more electrodes to which an electric potential is applied. In this work the Langmuir probes consist of one cylindrical electrode (the probe tip) with a biasing voltage applied to the probe tip against the metallic walls of the ion source. A current–voltage characteristic, i.e. I-V curve,

is measured. Generally, according to the voltage range applied to the probe tip, a different regime is found:

- Ion saturation regime: the voltage applied to the probe is much lower than the plasma potential ϕ_{plasma}, thus the current measured is due to positive ions accelerated towards the probe. Therefore the current measured in this region is negative.

- Transition regime: by increasing the probe voltage, also electrons, according to their energy distribution function, are collected on the probe tip. For a certain value of voltage applied to the probe tip, the so-called floating potential ϕ_{float}, the net current measured is zero, thus the net flux of charged particles is zero. If the electron velocity distribution is Maxwellian, the electron current increases exponentially with increasing biasing voltage applied at the probe tip.

- Electron saturation regime: for $V > \phi_{\text{plasma}}$, positive ions are repelled from the probe tip and electron collected.

The three different regime are illustrated in figure 3.6*a)* for the case of the black curve. In case of an electron-ion plasma, i.e. a plasma consisting of electrons and positive ions as charged particles, the current measured at the electron saturation regime is much higher than the one at the ion saturation regime, because the electron velocity is much higher than the ion velocity due to the lower mass. The increase of the current at the extreme regimes is due to the establishment of a sheath around the probe tip for $V < \phi_{\text{plasma}}$ and $V > \phi_{\text{plasma}}$, namely the effective collection area of the probe is larger than the probe surface.
For a voltage applied $V = \phi_{\text{plasma}}$ no sheath is established at the probe tip, thus the flux of charged particles at the probe is given only by the thermal flux. In the transition regime the current collected is due to electrons, positive ions and negative ions. For Maxwellian-distributed electrons (in velocity), the electron current is given by:

$$I_e(V) = A_p e n_e \frac{1}{4}\sqrt{\frac{8k_B T_e}{\pi m_e}} e^{\left(\frac{e(V-\phi_{\text{plasma}})}{k_B T_e}\right)}, V < \phi_{\text{plasma}}. \tag{3.7}$$

The contribution of electrons to the current in the transition region is dominant, due to the higher velocity given by the higher mass. Thus the total current in the transition region can be assumed as $I_e(V)$ of equation 3.7. The plasma potential is

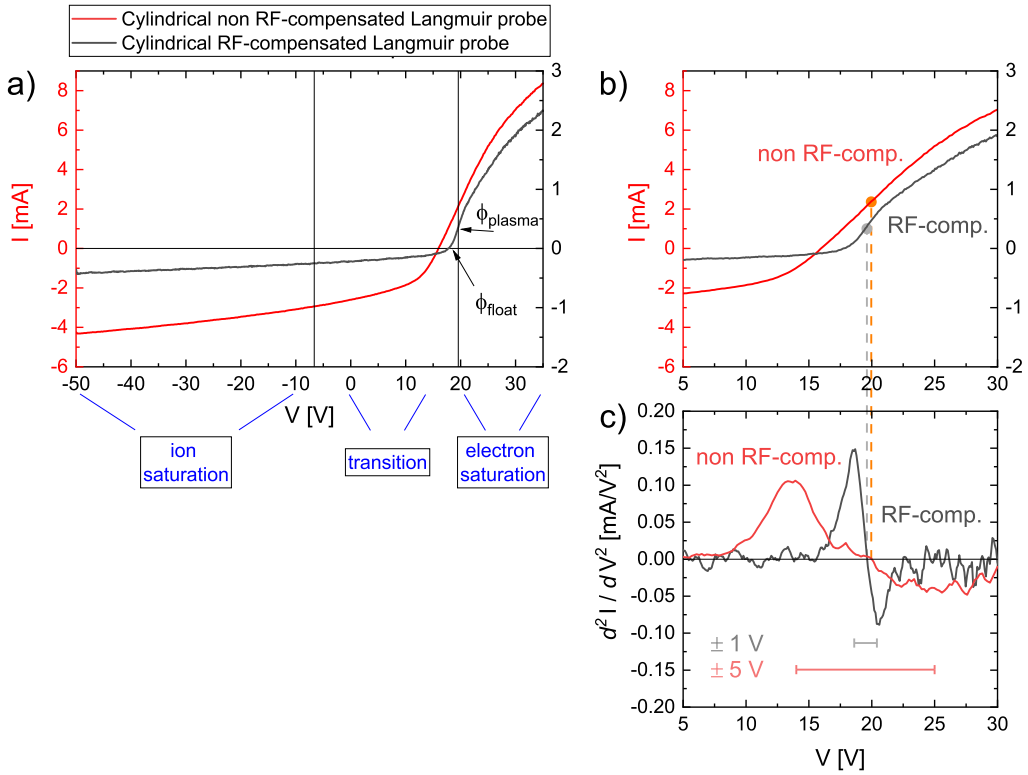

Figure 3.6: *a)*: two I-V characteristics measured with an RF-compensated cylindrical LP (black) and with a non RF-compensated cylindrical LP (red), the plasma properties are not the same. The thee regime of the I-V curve are drawn for the case of the black curve. *b)*: detail of *a* with the indication of the plasma potential. *c)*: second derivative of the I-V curve done with respect of the potential. The zero crossing of the curve indicates the plasma potential, the error on the absolute value is given by width between the maximum and the minimum of the curves.

the voltage for which the slope is at the maximum, or alternatively, the zero point of the second derivative of the I-V curve:

$$\frac{d^2(I_e(V))}{dV^2} = A_p e n_e \frac{1}{4}\sqrt{\frac{8k_BT_e}{\pi m_e}}\left(\frac{e}{k_BT_e}\right)^2 e^{\left(\frac{e(V-\phi_{\text{plasma}})}{k_BT_e}\right)}, \tag{3.8}$$

$V = \phi_{\text{plasma}}$ if and only if $\frac{d^2(I_e(V))}{dV^2} = 0$.

By using the zero of the second derivative, the value of plasma potential can be determined from a probe IV characteristics as shown in figure 3.6*c)*. The electron temperature T_e can be calculated either by applying an exponential fit to equation 3.7 or by calculating the electron energy probability function (EEPF) and applying a linear fit to the logarithm of it [66]. In both cases the error bar is about 0.7 eV of the absolute value measured.

In this work the theory used to retrieve the positive ion density from the I-V curve is the orbit motion limited (OML) theory [67]. This theory assumes a collisionless large (much larger than the probe radius) sheath where positive ions follows an orbital

motion around the probe tip and they can eventually impinge on the probe. The current I as a function of the potential applied to the probe is [67]:

$$I(V) = A_p n_+ e \frac{\sqrt{2}}{\pi} \left(\frac{e(V_s - V)}{M} \right)^{1/2} \tag{3.9}$$

with V_s denoting a temporary space potential used for fitting, A_p is the probe surface area, n_+ is the positive ion density, e is the electron charge and M is the effective ion mass. In the plasma under investigation, positive ions are assumed to be distributed as 40% of H^+, 40% of H_2^+ and 20% of H_3^+, thus the effective ion mass is 1.8 atomic mass unit. The positive ion density retrieved by fitting the ion branch with equation 3.9, can differ from the actual positive ion density in the plasma due to the approximation introduced in the theory and due to the uncertainty about the positive ion density composition. Typical values for the positive ion density are between $1 \cdot 10^{16}\,\mathrm{m}^{-3}$ and $2 \cdot 10^{17}\,\mathrm{m}^{-3}$. The relative error assigned to the positive ion density is between 5% and 10%, whereas the absolute error can be higher than a factor of two [68]

In an RF-generated plasma, the plasma potential oscillates with the RF frequency, i.e. about 1 MHz at ELISE, namely much faster than the acquisition rate for the I-V characteristics. Thus, the I-V curves measured without RF-compensation of the probe are an average of the current over the RF oscillations [69]. The compensation method applied at ELISE is passive compensation [70] via a compensation electrode, i.e. an electrode located close to the probe tip with a much larger area than the probe tip, which is floating in the plasma. Hence, the potential of the compensation electrode follows the RF oscillations. A transformer keeps the potential difference between tip and compensation electrode constant.

LP currently installed at ELISE are two cylindrical double probes used as non-RF compensated single probes and one movable RF-compensated cylindrical probe. The double LP are inserted from the diagnostic port XR+3U and XR-3U and the probe tip is parallel to the filter field lines. The movable RF-compensated LP is inserted from the port YT+1U also probing the plasma at about 2 cm distance from the PG: the probe tip can move in a vertical span of about 20 cm between 98 mm (position above the bias plate) to 313 mm from the upper wall (center of the upper beamlet group). A technical drawing illustrating the position of the probe tips on the upper part of the source is shown in figure 3.7. The probe tips are made of tungsten. The non RF-compensated LP has a tip length of 10 mm and diameter of 300 μm whereas the movable RF compensated LP has a length of 3 mm and diameter of 200 μm. The remaining part of the probe body is covered with an insulting material, i.e. ceramic.

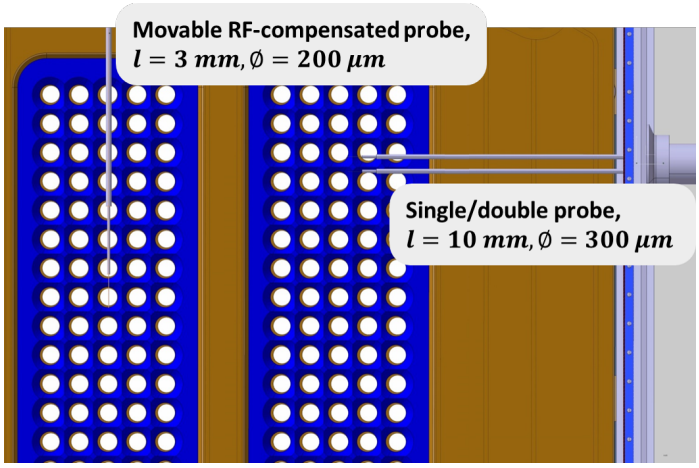

Figure 3.7: Technical drawing of the probe tips positioned on the upper part of the source. In this drawing, the movable probe is completely extended.

An example of I-V curve measured with the RF-compensated LP in black and with the non RF-compensated LP in red is shown in 3.6*a)*; the plasma properties of the region investigated by the two probes are different. A comparison between RF-compensated and non RF-compensated I-V curves is shown in figure 3.6 for the electron branch in *b)* and for the corresponding second derivative in *c)*. The plot in *b)* shows that the I-V curve measured with a non-RF compensated probe is distorted by the averaging of the current in this regime. Consequently, the plasma potential ϕ_{plasma} can not be reliably determined in the case of non RF-compensated LP. In the case of RF-compensated LP with an error of about 0.5 V-1 V on the absolute value can be assigned.

The presence of negative ions influences the shape of the I-V characteristics since negative ions contribute to the net current collected. For example, the net flux of particles at the plasma potential, where no sheath is established, is now due to the fluxes of three particle species:

$$I(\phi_{\text{plasma}}) = eA_p(\Gamma_e + \Gamma_{H^-} - \Gamma_+) \tag{3.10}$$

where A_p is the probe surface area. For the case of the negative ion sources under discussion, the temperatures of the charged species are similar, i.e. $\sim$1 eV, close to the plasma grid, thus the flux of negative ions becomes similar or higher than the electron flux if the electronegativity, i.e. $\alpha = n_{H-}/n_e$, is $n_{H^-}/n_e \gtrsim \sqrt{m_{H^-}/m_e} = 43$ (or 61 for deuterium negative ions). At the measuring position of the probe, i.e. 2 cm axial distance from the PG, the negative ion flux can give a relevant contribution to the current, in this case the I-V curve is symmetric with respect to plasma potential and

$\phi_{\text{plasma}} \approx \phi_{\text{float}}$ (e.g. see I-V curve shown in blue in figure 7.5, page 129). When the I-V curve is strongly asymmetric with respect to the plasma potential, e.g. black I-V curve of figure 3.6, then the negative particle branch of the I-V curve is dominated by the electron flux. Nevertheless, the electronegativity of the plasma at the meniscus is high and the value can be estimated by taking into account the ratio between the co-extracted electrons I_{EG} and the extracted negative ions I_{ext}, which is lower than one in a well conditioned source (as the ITER requirement is generally fulfilled in the ion source), thus:

$$j_{\text{EG}}/j_{\text{ext}} \propto \frac{n_e v_e}{n_{H^-} v_{H^-}} \approx \frac{n_e}{n_{H^-}} \sqrt{\frac{T_e/m_e}{T_{H^-}/m_{H^-}}} < 1 \Rightarrow \frac{n_{H^-}}{n_e} > \sqrt{\frac{m_{H^-}}{m_e}} = 43 \qquad (3.11)$$

by assuming a $T_e \approx T_{H^-}$; for deuterium, with the same calculation $\frac{n_{D^-}}{n_e} > 61$. It is possible to retrieve a value for the electron density from the I-V curve at the measuring position, but due to the high amount of negative ions and the variation of them with the operational parameters, e.g. magnetic field strength, the current at the plasma potential $I(\phi_{\text{plasma}})$ is given instead of the electron density. For the tip dimensions of the movable RF compensated LP at ELISE and a given electron temperature, the conversion factor between $I(\phi_{\text{plasma}})$ and electron density is given in table 3.4. The calculation is performed as if only electrons are present in the plasma as negatively charged species.

Table 3.4: Example of conversion between $I(\phi_{\text{plasma}})$ and n_e for T_e =1 eV and T_e =2 eV. Values calculated for the RF-compensated LP at ELISE by assuming a plasma where only electrons are present as negatively charged species.

$I(\phi_{\text{plasma}})$	T_e	n_e
1.0 mA	1 eV	$1.95\,10^{16}\text{m}^{-3}$
2.0 mA	1 eV	$3.90\,10^{16}\text{m}^{-3}$
4.0 mA	1 eV	$7.80\,10^{16}\text{m}^{-3}$
7.0 mA	1 eV	$1.36\,10^{17}\text{m}^{-3}$
10.0 mA	1 eV	$1.95\,10^{17}\text{m}^{-3}$
1.0 mA	2 eV	$1.38\,10^{16}\text{m}^{-3}$
2.0 mA	2 eV	$2.76\,10^{16}\text{m}^{-3}$
4.0 mA	2 eV	$5.51\,10^{16}\text{m}^{-3}$
7.0 mA	2 eV	$9.65\,10^{16}\text{m}^{-3}$
10.0 mA	2 eV	$1.38\,10^{17}\text{m}^{-3}$

3.2.2 Beam diagnostic techniques

Diagnostic systems used for multi-aperture beams are mainly based on spectroscopy and on power density measurement techniques.

Spectroscopic diagnostics are based on the spectral analysis of the beam emission and are LOS averaged. Thus, a localized measurement of beam properties is not directly possible. In general, the measurements need to be supported by modeling codes for the light emission using as input the beam intensity, the background gas profile, and on the characteristics of the optical system. Power density measurement techniques are based on the measurement of the beam power density deposited onto a surface. The power density is retrieved by infra-red or visible cameras looking at the surface or by thermocouples installed on the surface. If placed close to the grid system, where the power density is high, i.e. for single beamlet analysis, the limited total power load that these devices can withstand limits the operational scenario either in term of beam-on time or in term of beam energy.
At the ELISE test facility, the total extracted negative ion current I_{ext} is measured electrically as the net current impinging on any surface downstream of the EG. Installed on the beam side are a tungsten wire calorimeter (TWC), beam emission spectroscopy (BES), and a diagnostic calorimeter which allows for measurements of the deposited power by water calorimetry (WC) and infra-red (IR) calorimetry. The total accelerated current is measured by the IR calorimetry and water calorimetry. The beam diagnostics are shown in figure 3.8 [71].
Since the beam is measured by BES and by the diagnostic calorimeter at large distances from the GG, single beamlet measurements are not possible due to the large beamlet overlap occurring at such axial distances. The beam divergence can be considered a fixed value once space charge compensation [55] occurs at a small distance from the GG (see section 2.5), thus preventing the sudden increase of beamlet divergence due to electrostatic repulsion of the beam particles. Space charge compensation depends on the background gas pressure (about 0.01-0.05 Pa at ELISE) and the beamlet current density.

Tungsten wire calorimeter

The tungsten wire calorimeter allows for a qualitative monitoring of the beam shape during the extraction phase [71]. It consists of a frame of 100 tungsten wires drawn vertically and horizontally perpendicularly to the beam direction positioned at 1.8 m downstream of the GG. The diameter of the tungsten wires is 0.3 mm and they are spaced by 20 mm. The beam passes through it and heats the wires: the emission is recorded by a visible camera to monitor the temporal evolution of the beam shape. This diagnostic is not absolutely calibrated thus providing only qualitative images of

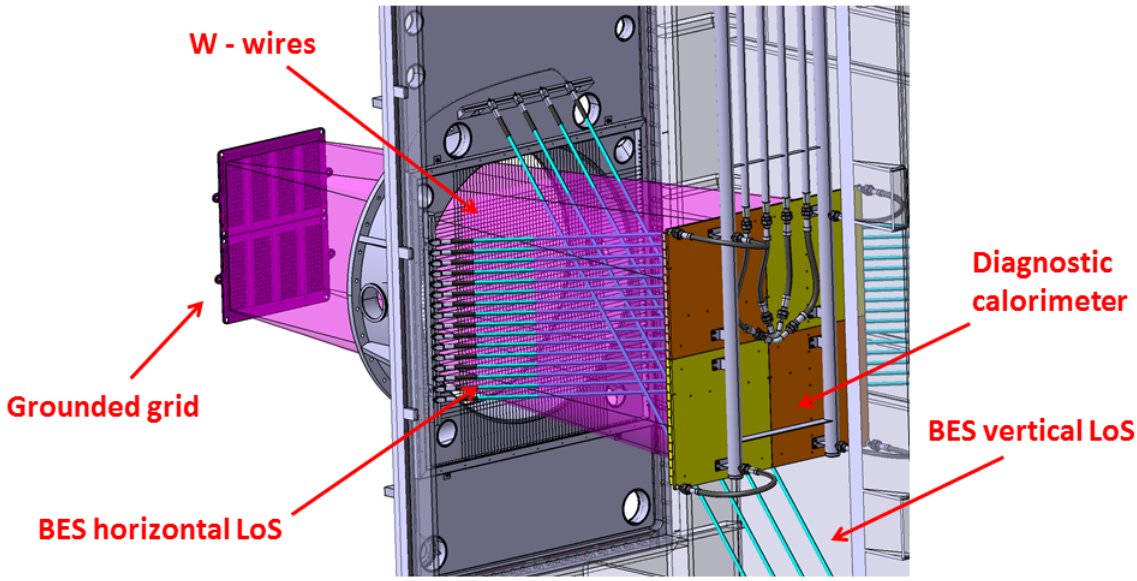

Figure 3.8: Overview of the beam diagnostic systems at ELISE [71]: the tungsten (W) wire calorimeter, the two arrays of lines of sight (LOS) of the BES diagnostic and the diagnostic calorimeter on the right. On the leftmost side of the figure, the downstream side of the grounded grid is sketched.

the beam power distribution.

Beam emission spectroscopy

At about 2.7 m downstream from the GG, 20 BES LOS (see figure 3.8)[71] intercept the beam, providing local but line-integrated measurements of beam divergence, intensity and stripping losses. The BES diagnostic is based on the Doppler shift effect of the H_α or D_α Balmer line produced by the impact of the accelerated beam particles with background particles [72]. The most relevant reactions for the production of H_α on the beam side are [72]:

$$\underline{H^-} + H_2 \rightarrow \underline{H^0(n=3)} + H_2 + e$$

$$\underline{H^0} + H_2 \rightarrow \underline{H^0(n=3)} + H_2$$

$$\underline{H^-} + H_2 \rightarrow \underline{H^0} + 2H^0(n=3)$$

where the fast particles are underlined; the processes are the same in case of deuterium. The arrangement of the 20 LOS is shown in figure 3.8: 16 LOS are looking along the horizontal direction with a vertical spacing of 5 cm while four LOS are looking vertically with a horizontal spacing of 16 cm. The higher resolution along

the vertical direction is desirable to identify the effect of the vertical plasma drift on the beam profile. Each LOS consists of a telescope placed inside the tank: the light collected by the optical head is then conveyed through an optical fiber to a high-resolution Acton spectrometer equipped with a CCD camera (the dispersion is 7 pm/pixel for a total spectrum of 8 nm). The optical head axis has an angle $\vartheta = 50$ degrees with respect to the beam direction and the radiation emitted is Doppler shifted of the quantity:

$$\lambda_{Doppler} = \frac{(1 + \beta \cos \vartheta)}{\sqrt{1 - \beta^2}} \lambda_0 \tag{3.12}$$

where $\beta = v/c$ represents the particle velocity and λ_0 is the wavelength for the unshifted H_α or D_α line. A typical BES spectrum is shown in figure 3.9(a) where three main features are distinguishable: the unshifted H_α peak on the left, the so-called stripping peak caused by negative ions neutralized by collisions with the background gas before being fully accelerated, i.e. upstream the GG, and the Doppler shifted H_α peak on the right. The beam divergence is estimated from the half width at one e-folding of the Doppler peak, also taking into account the apparatus profile of the spectrometer and the opening angle of the telescopes [73]; the Doppler peak integral is proportional to the local but LOS averaged beam current density and to the background gas density. The signal collected by each LOS originates from different rows of beamlets, every row alternately deflected left or right due to the deflection magnets. Due to the LOS tilting, the signal is collected at different distance from the GG depending on the position of the beamlet along the LOS. LOS averaging and collection of light from different beamlet rows increase the broadening of the Doppler peak resulting in a increased value of divergence, which is not representative of the single beamlet divergence but rather an averaged value over the beam. To retrieve a realistic value for the single beamlet divergence from the Doppler peak width the analysis must be combined with modeling activities and simulations [74]. The BES diagnostic is absolutely calibrated but the beam length is not exactly known thus is not possible to retrieve a value for the absolute emission intensity; quantitative comparisons among LOS are anyway possible. In figure 3.9*b)* and 3.9*c)* the vertical and horizontal beam profile given by Doppler peak integral and the LOS averaged beam divergence (retrieved by the Doppler peak width) are shown, respectively.
The vertical profile of the Doppler peak integral highlights the presence of two areas with high intensity: these are the vertical projection of the top and bottom beam segments originating from the top and bottom grid segments, respectively. In correspondence to the higher current density a lower divergence measured is observed in

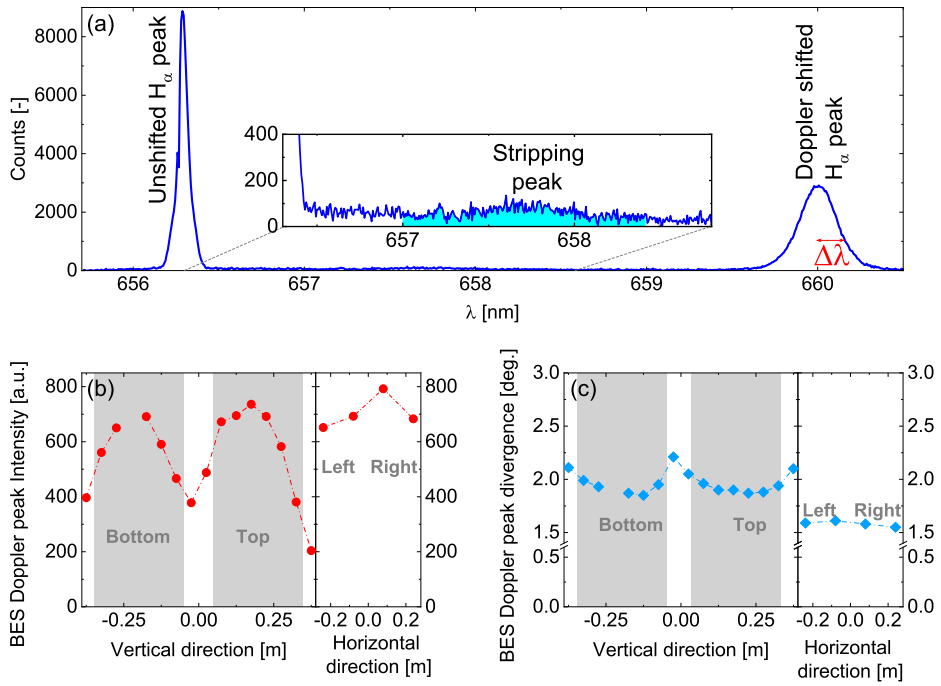

Figure 3.9: (a) Example spectrum from the horizontal LOS 10 positioned at +7.5 cm from the geometrical center of the beam: at 656.28 nm the H_α unshifted peak is visible while the Doppler shifted peak is placed at a wavelength shift proportional to the total HV applied. Between these two peaks, the so-called stripping peak is visible. (b) Vertical and horizontal profiles of the Doppler peak integral. (c) Vertical and horizontal profiles of the divergence retrieved from the Doppler peak width. In (b) and (c) the shaded areas correspond to the vertical projection of the beamlet groups. The LOS positioned at -22.5 cm is not available. Shot 27115 performed in hydrogen at 0.3 Pa filling pressure, 180 kW total RF power for an extracted current of I_{ext}=18.7 A with 6 kV extraction and 30 kV acceleration voltage; I_{PG}=1.6 kA + external strengthening magnets (1.9 mT) [73].

figure 3.9*c)*. The LOS between the top and the bottom beam segments, in a portion of volume not directly illuminated by apertures, measure a low intensity with high beam divergence indicating that the beam in that region is weak and formed by highly divergent particles due to the overlap of beamlets located on the edges of the beam segments. The beam is not centered with respect to the zero of the scale but slightly displaced downwards due to the vertical deflection caused by the filter field.

For a D^- extracted current density of 286 A/m^2 (ITER target), the beamlet divergence, defined as half width at one e-folding of the angular particle distribution, predicted at ELISE by the IBSIMU code [75][76] is 14.4 mrad (19.5 mrad for an H^- extracted current density of 329 A/m^2). The simulations are performed with a perpendicular particle velocity of 1 eV [77], 10 kV of extraction voltage, and 50 kV of acceleration voltage. In case of good beam optics, the beam divergence measured by BES diagnostics is around 1.4 to 2 degrees (24 to 35 mrad) measured by the vertical

BES LOS both in hydrogen and in deuterium. For the horizontal LOS, the measured divergence is usually higher because the overlap of multiple rows of beamlets, each one horizontally deflected alternately left or right by the deflection magnets, causes an artificial broadening of the line-integrated Doppler peak. The vertical LOS, instead, measure the beam averaging top and bottom beam segments including also the area between the segments, thus collecting highly divergent particles. The effect of the beamlet overlapping on the broadening of Doppler peak is shown in reference [74] calculated for the Batman Upgrade test facility [15][78].

Diagnostic calorimeter

The beam is stopped at 3.5 m downstream of the GG by a diagnostic calorimeter [71] that can withstand high (maximum 3 MW/m^2) power density for about 10 s every $\approx$ 150 s (adapted to the duty cycle of the extraction phases possible at ELISE) [79]. The diagnostic calorimeter is designed in order to perform calorimetric and thermometric measurements of the beam power deposited onto it. The calorimeter is made of four actively-cooled copper plates of 60 cm $\times$ 60 cm each: a water calorimetry technique is applied to assess separately the power deposited into each plate. 900 copper blocks of 3.8 cm $\times$ 3.8 cm surface area each, are brazed onto the beam facing surface of the copper plates through channels characterized by an high thermal resistivity. In this way the heat stays in the blocks during the pulses and it is cooled down by the water channel after the extraction phase. The scheme of the 30 $\times$ 30 blocks is displayed in figure 3.10*a)*.

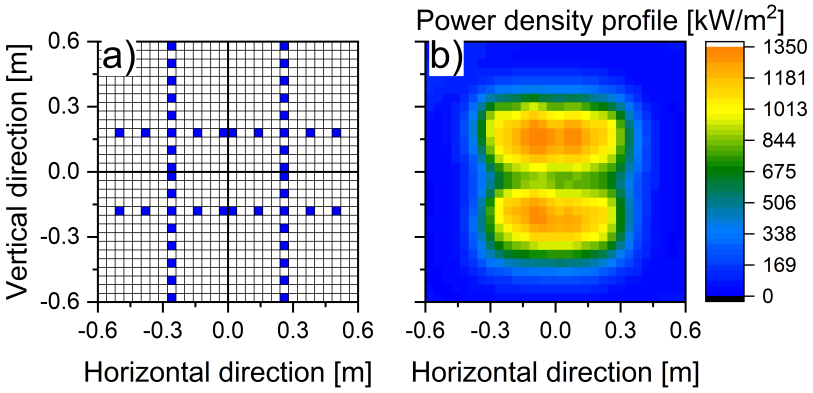

Figure 3.10: (a) Schematic of the 900 block composing the calorimeter surface; indicated in blue are the blocks in which the 48 thermocouples are embedded. (b) 2D power density profile of the beam: the spatial resolution (30 $\times$ 30) is given by the block dimension. Data of shot 27115 performed in hydrogen at 0.3 Pa filling pressure, 180 kW total RF power for an extracted current of I_{ext} = 18.7 A with 6 kV extraction and 30 kV acceleration voltage I_{PG} = 1.6 kA + external strengthening magnets (1.9 mT).

A 2 mm gap divides each block from the neighboring ones. This design has been chosen in order to keep the power deposited by the beam in the blocks independent from the adjacent ones, being able to treat each block as a single independent element. 48 thermocouples are embedded into as many blocks of the calorimeter (the thermocouple pattern is shown in figure 3.10*a)* with blue squares) to measure the absolute temperature. To decrease the reflectivity of the beam-facing side of the diagnostic calorimeter, the surface is covered with a MoS_2 coating [79]. A high resolution (640×480 pixels) FLIR A655sc infra-red (IR) micro-bolometer camera placed outside the vacuum chamber is looking at the diagnostic calorimeter through a ZnSe window with anti-reflective coating. Although the camera has a high resolution, the actual experimental spatial resolution for a 2D map of the beam power deposited onto the calorimeter is given by the 30×30 calorimeter blocks. The block temperature increase ΔT due to the beam power deposition is assessed from the measured radiation through a calibration procedure [73] based on the determination of the surface emissivity by comparing the IR measurement with the thermocouples. An example of 2D power density profile is shown in figure 3.10*b)*. The temperature increase ΔT is proportional to the deposited beam power P,

$$P = \frac{c_{\mathrm{Cu}}\, m\, \Delta T}{t_B}, \tag{3.13}$$

where m is the mass of the single copper blocks, c_{Cu} is the heat capacity of copper and t_{B} is the beam-on time. For the case shown in figure 3.10*b)*, the power deposited in 9.5 s extraction phase for the block with the highest temperature increase is (1.96 ± 0.06) kW, the total power deposited onto the calorimeter is 586 kW. From the total HV (36.2 kV) and the total extraction area (985 cm^2), an accelerated averaged current density of 164 $\mathrm{A/m}^2$ is calculated.

A validation of the total power averaged over the calorimeter surface measured by IR analysis is done through a comparison with the water calorimetry measurement also averaged over the diagnostic calorimeter. The comparison of the total accelerated current density (obtained dividing the averaged power density by the applied HV) deposited onto the diagnostic calorimeter measured by IR calorimetry and by water calorimetry [71] is shown in figure 3.11 for about five thousand pulses, both in hydrogen and deuterium.

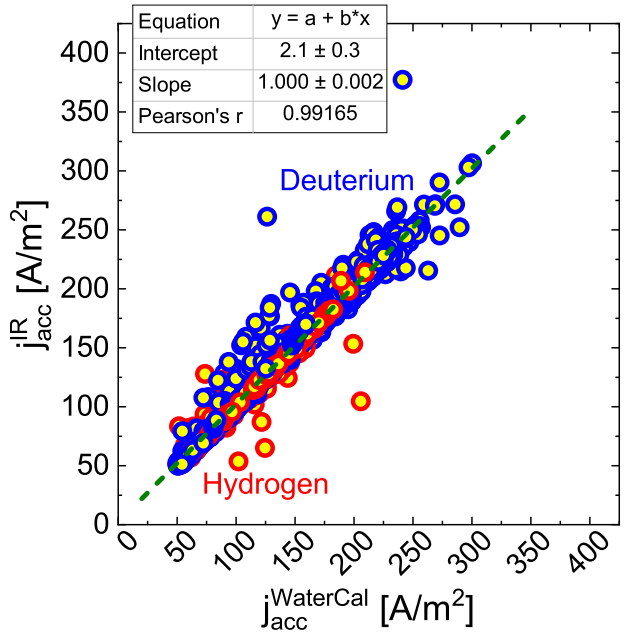

Figure 3.11: Comparison between the accelerated current density j_{acc} as measured by water calorimetry and by IR calorimetry. The pulses are done between January 2017 and July 2018, both in hydrogen and deuterium. A linear fit is applied to the whole data set: the resulting slope is 1.000 ± 0.002 and the intercept is 2.1 ± 0.3.

A linear fit of the whole data set is performed and the results are shown in figure 3.11. The linear fit is not forced to zero to check for the presence of an offset between the two measurements: the offset is 2.1 A/m^2, which is very small compared to the typical value measured ($\leq 5\%$). By considering the error bars of both diagnostics, i.e. $\pm 5\%$ of the IR calorimetry and $\pm 10\%$ of the water calorimetry, the offset is compatible with the measurement error. The goodness of the fit is given by Pearson's r coefficient and it is very good in this case, being the value close to one. The very good agreement between the two measurements allows the estimation of j_{acc} retrieved by IR calorimetry to be validated. For the averaged accelerated current j_{acc} over the calorimeter surface, IR calorimetry and water calorimetry are equivalent but, as shown in figure 3.10*b)*, IR calorimetry is preferable because it gives a spatial resolution of 4 cm.

The main general characteristics of the beam power density profile can be observed in figure 3.10*b)*: the beam is divided in two parts, the top and bottom beam segments which usually differ in intensity and width. For each beam segment, the four beamlet groups are barely visible; the two central beamlet groups are more intense due to the overlap of the neighboring groups. In the filter field configuration with the magnetic field directed from left to right (as in figure 3.1) the beam is shifted downwards and the displacement, being usually between 2 cm and 10 cm at the calorimeter, depends on the strength of the filter field, on the total high voltage applied to the grids and on the isotope (H or D) (see section 2.5).

The 2D map of the beam power deposited onto the calorimeter provides a qualitative

insight on the beam profile: a fitting routine is applied in order to retrieve quantitative information on the beamlet group vertical and horizontal width, intensity and on the vertical position of the beam segments [73]. The fitting formula is a sum of eight bi-dimensional Gaussian functions that represent the eight rectangular beamlet groups: the fitting function as a function of the vertical and horizontal coordinates (y and x in the equation, respectively) is reported in equation 3.14 and a schematic of the fitting function with the output parameters is shown is figure 3.12*b)*.

$$f(x,y) = \sum_{i=1}^{4} A_i e^{-\frac{(x-x_{0,i})^2}{2(\sigma_x^{\mathrm{top}})^2} - \frac{(y-y_{\mathrm{top}})^2}{2(\sigma_y^{\mathrm{top}})^2}} + \sum_{i=5}^{8} A_i e^{-\frac{(x-x_{0,i})^2}{2(\sigma_x^{\mathrm{bot}})^2} - \frac{(y-y_{\mathrm{bot}})^2}{2(\sigma_y^{\mathrm{bot}})^2}} \tag{3.14}$$

The horizontal position of the Gaussians $x_{0,i}$ is fixed and it corresponds to the horizontal center of the beamlet group on the GG (see 3.12(a)), since no horizontal deflection of the entire beamlet group is forseen or observed, and it corresponds to the geometrical center of the beamlet groups on the GG. The vertical positions of the top and bottom beam segments (y_{top} and y_{bot}) are free parameters due to the vertical deflection of the beam caused by the filter field. The vertical and horizontal width (σ_y and σ_x) of the Gaussian are assumed identical for the four beamlet groups in each beam segment because no inhomogeneity among beamlet groups belonging to the same beam segment is expected. The amplitude of each Gaussian function is described by the free parameters A_i, with $i = 1 \ldots 8$. The error assigned to the fit outputs σ_x, σ_y, y_{top} and y_{bot} is calculated to be $\approx 1.5\,\mathrm{cm}$ whereas the peak intensity of the Gaussians representing the beamlet groups (A_i, $i = 1 \ldots 8$) has an error bar of about 5% [73]. The schematic representation of the fitting function superimposed to a power density profile is shown in figure 3.12*b)*. In this model, the integral of the the Gaussian function describing one beamlet group is proportional to the accelerated current carried by the beamlets belonging to that beamlet group. The integral is calculated by integrating each Gaussian function to infinity, thus including beam losses outside the calorimeter surface ($\leq$10% or negligible in the majority of the cases) which can occur in case of high beam divergence or high beam deflection caused by a strong filter field. The accelerated current can be calculated for each beamlet group and in the case of the top beam segment it is

$$I_{\mathrm{acc}}^{\mathrm{top}} = V_{\mathrm{top}}^{\mathrm{fit}} = \int_{-\infty}^{+\infty}\int_{-\infty}^{+\infty} \left(\sum_{i=1}^{4} A_i e^{-\frac{(x-x_{0,i})^2}{2(\sigma_x^{\mathrm{top}})^2} - \frac{(y-y_{\mathrm{top}})^2}{2(\sigma_y^{\mathrm{top}})^2}} \right) dxdy = 2\pi \sum_{i=1}^{4} A_i \sigma_x^{\mathrm{top}} \sigma_y^{\mathrm{top}} \tag{3.15}$$

and the corresponding case for the bottom is $I_{\mathrm{acc}}^{\mathrm{bot}} = V_{\mathrm{bot}}^{\mathrm{fit}} = 2\pi \sum_{i=5}^{8} A_i \sigma_x^{\mathrm{bot}} \sigma_y^{\mathrm{bot}}$.

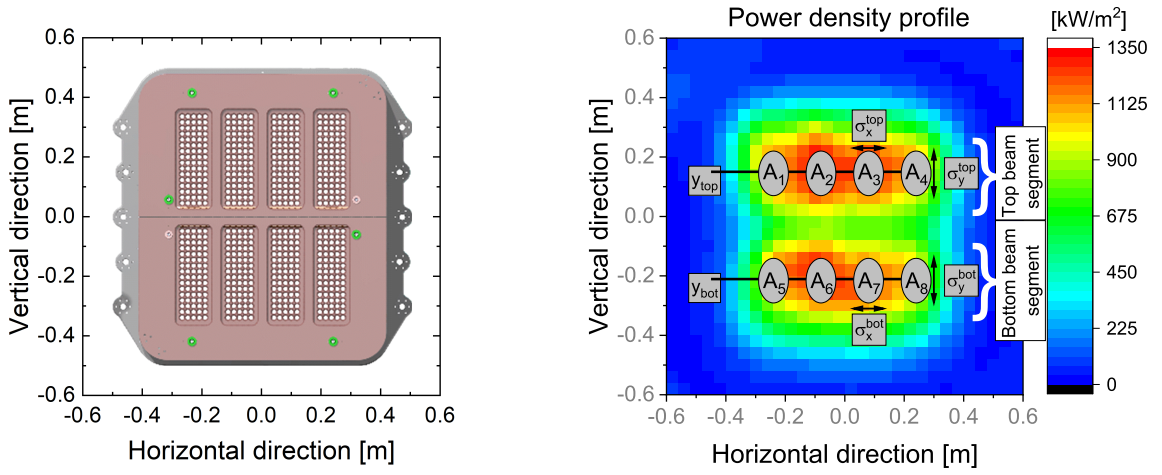

(a) (b)

Figure 3.12: *a)* Aperture arrangement on the PG. *b)* Schematic of the fitting function applied to the 2D map of the power density on the calorimeter. The parameters of the fitting function are superimposed to power density profile. The top and bottom beam segments enclose the beamlet groups located on the top and on the bottom side of the calorimeter, respectively.

3.2.3 Electrical measurements

Electrical measurements are performed on several surfaces of the source and grid system. The two segments of the bias plate are electrically connected to the source wall, thus sharing the same potential, but electrical measurements of the current impinging on the bias plate are possible. The currents measured on the two segments of the

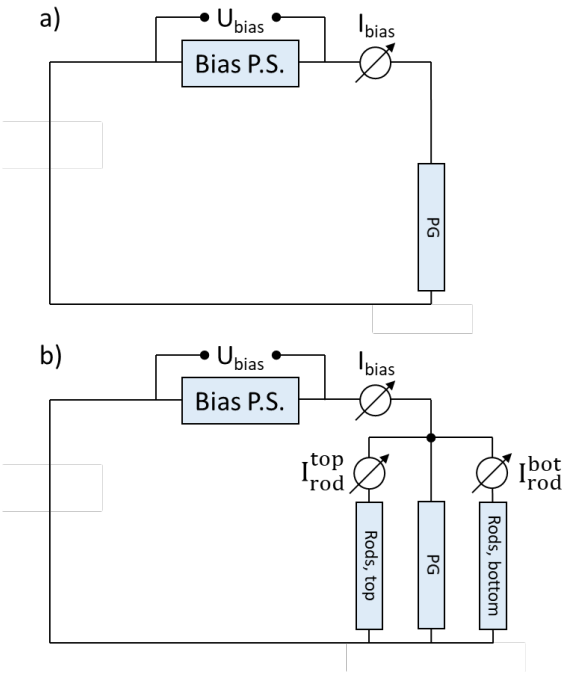

Figure 3.13: Simplified electrical scheme of PG biasing mechanism. In *a)* in the case without rods and in *b)* with rods connected to the PG potential. The plasma is represented as a resistor. The measured currents are reported in figure.

bias plate, i.e. $I_{\mathrm{BB}}^{\mathrm{top}}$ and $I_{\mathrm{BB}}^{\mathrm{bot}}$, are due to the flux of positive ions: the plasma potential is higher than the source wall potential, thus positive ions are accelerated onto the bias plate and negative charges are repelled.
The plasma grid is biased positively with respect to the source walls to modify the charged particle fluxes at the PG surface. To avoid large current drawn over the PG, e.g. during the plasma ignition, the bias power supply is controlled in current I_{bias}. The potential applied to the PG, i.e. U_{bias}, is given as a unique value for the entire grid.
The configuration with the potential rods (see next section, page 60) electrically connected to the PG, and thus to the bias power supply, is different: the sum of the currents collected on the potential rods and on the PG is equal to I_{bias}, additionally the currents collected on top rod segment and on the bottom rod segment are measured separately as $I_{\mathrm{rod}}^{\mathrm{top}}$ and $I_{\mathrm{rod}}^{\mathrm{bot}}$, respectively. A scheme of the PG biasing is shown in figure 3.13: the effect of the plasma on the components, i.e. PG and rods, is schematized as a resistor, which can have positive or negative value. Without rods, the current collected on the PG is equivalent to I_{bias}, whereas with rods the current measured on the PG is given by $I_{\mathrm{bias}} - I_{\mathrm{rod}}^{\mathrm{top}} - I_{\mathrm{rod}}^{\mathrm{bot}}$.
Downstream of the PG other electrical measurements are performed: the total drain current I_{drain} is the total current electrically measured and it includes co-extracted electrons, negative ions, stripped electrons and all the charged particles accelerated by the HV power supply. The extracted negative ion current I_{ext} is the current collected downstream of the EG, i.e. current on ground potential. The electrically measured currents on the two segments of the EG, $I_{\mathrm{EG}}^{\mathrm{top}}$ and $\mathrm{I}_{\mathrm{EG}}^{\mathrm{bot}}$, are assumed to be electrons impinging on the EG. The currents measured on the two segments of the GG, $I_{\mathrm{GG}}^{\mathrm{top}}$ and $I_{\mathrm{GG}}^{\mathrm{bot}}$, are due to stripped and secondary electrons and highly divergent negative ions.

3.3 Present status of ELISE operations

Cs conditioning is necessary to reach high extracted ion current and a low co-extracted electron current, which are temporally stable up to one hour pulse due to a low and stable work-function at the PG. Cs conditioning consists in a series of short pulses (20 s plasma and 9.5 s beam) to create a suitable Cs reservoir on the inner surfaces of the source and to redistribute Cs [80]. The conditioning phase ends when the negative ions reach the highest value with the lowest amount of electrons possible.

The Cs conditioning procedure is performed after an opening phase of the ion source and it can last up to two-three weeks; a re-conditioning procedure is repeated every operational day and it can last up to 2 hours [80]. A daily Cs conditioning phase is needed to deposit fresh Cs and to recover a low PG work function after deposition of impurities over night [81]. The Cs ovens are activated at the beginning of each operational day and switched-off in the evening.
The transition from a Cs-free source to a Cs-conditioned source has a strong impact on the beam profile [82]: with the low extracted current density typical of a Cs-free source the normalized perveance (see section 2.5) is low, thus the beam divergence is poor; with the increase of the extracted current density the perveance improves and consequently, the beam optics improves. Due to the plasma drift, the plasma density is higher on the upper part of the ion source thus an adequate amount of Cs is present on the upper part of the source earlier in the conditioning phase than in the bottom part: in an intermediate phase of the conditioning, the beam profile shows a good divergence on the upper part whereas the bottom beam divergence is still poor [82].
Different Cs conditioning techniques have been developed, such as the Cs over-conditioning technique [80]. In long pulses, for which the Cs over-conditioning technique is usually applied, the extracted negative ion current density of the first beam blip is reduced, but the Cs redistribution improves the stability of the extracted current density for the following blips. An example of long pulse where the over-conditioning technique is applied is shown in figure 3.16: the extracted current density and, consequently, the accelerated current density of the first beam blip are reduced, but the following blips are stable in extracted current density (see left-hand side of figure 3.16).
The ELISE test facility offers the possibility to test physical measures, that improve the source performance such as the reduction of the co-extracted electrons or the pulse stability for long pulses to reach the ITER requirements [83]. Two of these measures are the installation of external permanent magnets [84] and the installation of the so-called potential rods [80].

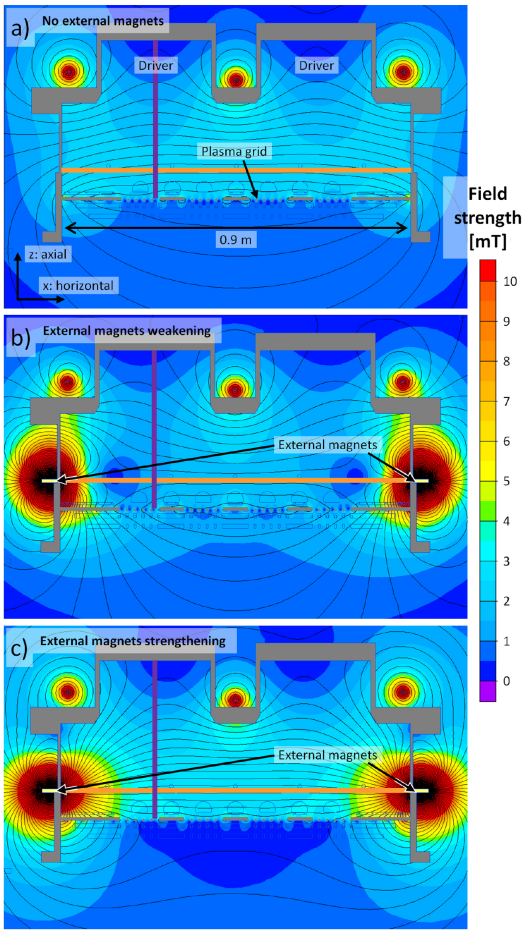

Figure 3.14: 2D map of the magnetic field (horizontal cut) for the case of $I_{PG} = 2.5\,kA$ without external permanent magnets (a), with weakening magnets (b) and with strengthening magnets (c)[84].

Investigations at BATMAN showed that the topology and the strength of the filter field influence the source performance especially about the co-extracted electron current [85] thus a similar investigation is performed at ELISE with external permanent magnets installed sideways the source walls to change the field topology. The external permanent magnets are installed at 7.5 cm axial distance from the PG; the main component of the magnet magnetic field is parallel to the filter field. Two configurations have been tested: the case with external magnets strengthening the filter field and the case weakening the filter field. In figure 3.14 the color plots of the magnetic field map in the case without external magnets (a), in the weakening configuration (b) and in the strengthening configuration (c) are shown.

The magnetic field topology, with the creation of magnetic-free areas or magnetic mirrors, modifies the transport of magnetized particles towards the lateral walls, thus affecting the Cs redistribution as well as the plasma parameter distribution. As reported in ref. [84] the best configuration to reduce the co-extracted electrons and stabilize the co-extracted electrons for long pulse is the strengthening one.

The potential rods, positioned as shown in figure 3.15, are metallic water-cooled vertical plates positioned upstream of the bias plate and between the aperture groups (6 rods in total, three from the top and three from the bottom). The potential rods can be biased differently with respect to the neighboring surfaces, namely the PG and bias plate, to modify the fluxes of charged particles onto the rods, thus modifying the plasma parameters and the transport of Cs close to the PG. Depending on the potential applied to the rods with respect to the plasma potential, the fluxes

of electrons from the driver region can be modified, thus the potential rods can also have an indirect effect on the diamagnetic drift. The configuration that gives the best performance is the case in which the rods and PG are biased at the same potential [80]. The potential rods improve the long pulse stability by decreasing, symmetrizing and stabilizing the co-extracted electron current. It has been observed that the Cs conditioning takes longer with the potential rods installed [80].

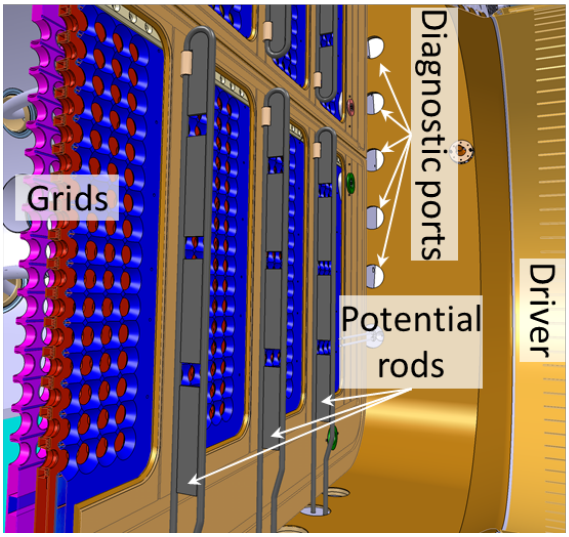

Figure 3.15: CAD view of the bottom part of the expansion region with potential rods installed. Courtesy of Markus Fröschle.

For long pulses the co-extracted electron current is unstable in time as can be shown in figure 3.16, i.e. it increases blip by blip. The cause of the temporal instability of the co-extracted electron current is the degradation of the PG work function.

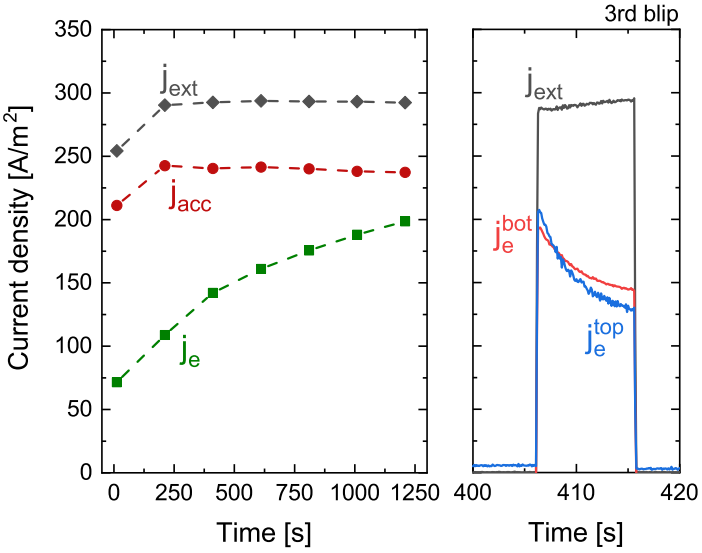

Figure 3.16: Best long pulse in hydrogen (1200 s with 8 beam blip). Parameters: H, P_{RF} =74.5 kW/driver, 0.3 Pa, U_{ext}=10.6 kV. Right: time-trace of the third beam blip [19].

In deuterium, for identical RF power applied in the drivers the atomic density is higher compared to hydrogen, because the dissociation degree is higher. Thus, the atomic flux onto the plasma grid is higher, implying an higher emission of negative ions from the PG [86]. In the expansion region, electrons, which are the only magnetized particle species, are affected by the $\times B$ drifts. Consequently, the ambipolar field affects the deuterium positive ions, whose velocity is lower for the same applied ambipolar field compared to the hydrogen positive ions due to the double mass, i.e. $v \propto \sqrt{m}$. Thus, a better uniformity of the positive ion density is expected and observed in the expansion region. A detailed study of the isotope effect is carried out in ref. [86] for the BATMAN ion source. In deuterium operations, compared to the hydrogen case, the dynamics of the co-extracted electron are much more unstable, thus a reduction of the applied RF power and of the extraction voltage is necessary. In figure 3.17, the comparison between the extracted current densities

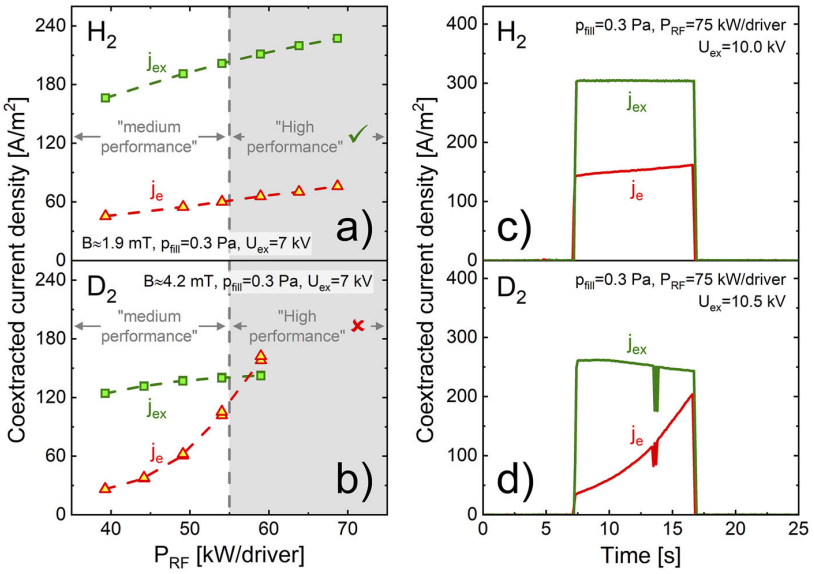

Figure 3.17: Isotope effect between hydrogen and deuterium. *a)* and *b)*: extracted negative ion and co-extracted electrons as a function of the RF power. *c)* and *d)*: time traces of the extracted negative ion current and the co-extracted electron current for a short pulses [87].

With the tools of IR calorimetry and BES spectroscopy divergence the beam is characterized segment-wise in terms of accelerated current, vertical and horizontal width. Typically, the beam is characterized by a symmetric top-bottom accelerated current, i.e. the beam segment values differ less than 10%, but the bottom beam segment is characterized by a larger width and a higher beam divergence with respect to the top beam segment.

4 Plasma characterization

This chapter presents the results of the characterization of the ion source plasma at ELISE, which is carried out by combining different plasma diagnostics and electrical measurements on the ion source. The characterization is firstly carried out in the driver region where plasma parameters, such as electron temperature T_e and density n_e and ratio between atomic and molecular hydrogen n_H/n_{H_2}, are retrieved by combining OES diagnostics with the collisional radiative model based on YACORA. The effect of the the RF power P_{RF} and of the magnetic filter field I_{PG} on the driver plasma is studied in section 4.1 at the ITER-relevant pressure of 0.3 Pa. In the same section, the symmetry of the plasma emission between drivers is studied for the first time. Relevant for the particle flux at the PG is that the plasma parameters are identical in the four drivers, thus the plasma generation is symmetric and it is not the cause of the plasma vertical asymmetries observed at the PG.
In the expansion region the plasma drift strongly affects the plasma both in terms of plasma density (electrons and positive ions) and local sheath ($U_{\mathrm{bias}} - \phi_{\mathrm{plasma}}$) at the PG. An example of the effect of the drift forces on the plasma emission is shown in figure 4.1: prompted by a variation of RF power coupled in only one pair of driver, the plasma parameters at the PG vary at all the vertical positions investigated and, consequently, the plasma emission varies as well. At t =5 s both RF generators apply the same RF power to the plasma, i.e. $\approx$ 40 kW/driver. At t =9 s only the upper pair of drivers apply a higher RF power, i.e. 60 kW/drivers, and the effect on the emission is then visible with a different magnitude for all the LOS close to the PG. Finally, at t =16 s, the bottom pair of drivers apply an RF power of 57 kW/drivers and the effect is now visible mainly for the LOS located at center and at the bottom of the ion source. The influence of the plasma drift is not straightforward and the plasma parameters at the PG depend on the vertical position. Despite of the example here reported, in section 4.2 the behavior of the plasma close to the PG is studied combining different diagnostics available with the purpose to study the plasma in terms of the

electron, positive ion and negative ion density and the plasma-wall potential interface.

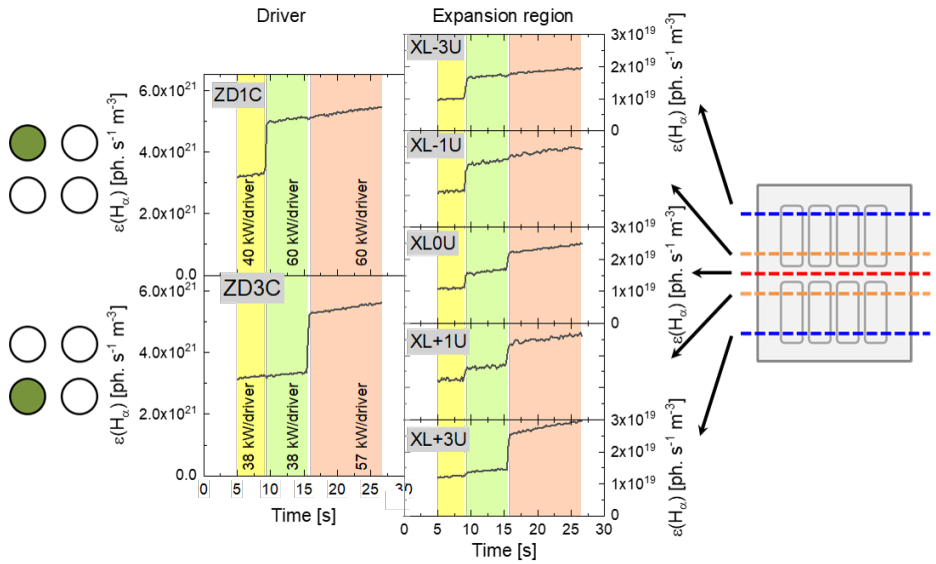

Figure 4.1: Emission of H_α measured in the two drivers (left) and in the expansion region (right). The RF power is step-wise increased in the two drivers at two different times. Hydrogen at p_{fill} =0.4 Pa, I_{PG}=1.6 kA + external strengthening magnets (1.9 mT), namely a magnetic field of at 2 cm axial distance from the PG.

The evolution of the aforementioned plasma properties as a function of the magnetic filter field and the biasing of the PG especially regarding the vertical symmetry, i.e. top and bottom of the ion source, is fundamental to identify the reasons for the vertical asymmetry of the co-extracted electrons and how much it affects the negative ion beam.

4.1 Plasma properties in the driver region

In this section the operational parameters influencing the plasma in the driver region are described: the applied RF power, which influences the electron density and atomic flux towards the PG, and the magnetic filter field, which affects the charged particle diffusion from the driver region towards the PG and the particle flux at the PG.
The applied RF power determines the RF field and consequently the collision frequency of electrons with the background gas: the higher the frequency of ionizing collision, the higher the electron density in the plasma. With increasing RF power, the electron density increases whereas the electron temperature is not affected. As a consequence of the electron density increase, the rate of the dissociation processes, which are driven by electron collisions, increases. The result is an increase of the

atomic to molecular ratio, i.e. n_H/n_{H_2}. The same mechanism here described applies for discharges performed with deuterium gas.

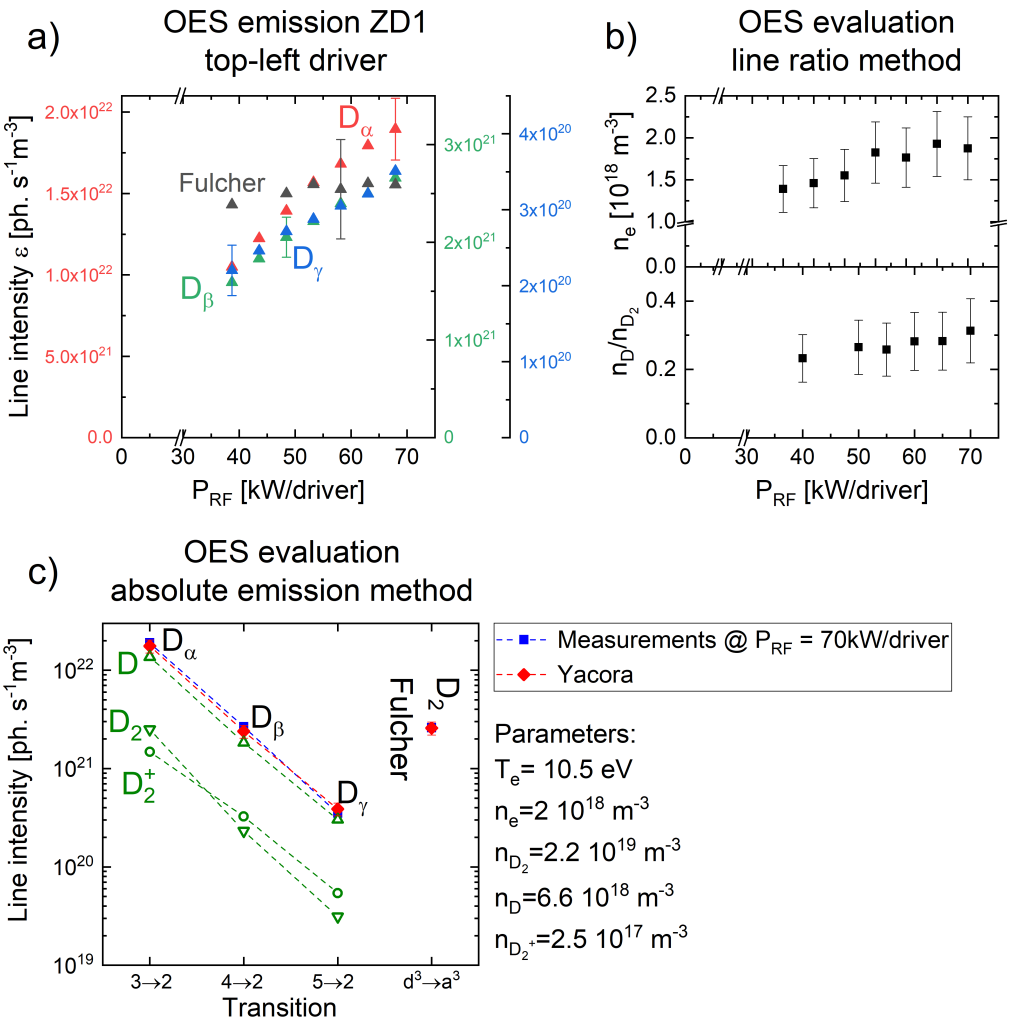

Figure 4.2: *a)* emission of the Balmer lines D_α, D_β, D_γ and of the Fulcher band measured by OES with the relative error bars. The scale for Fulcher is the green one, i.e. first scale on the right. Parameters of the scan: D, p_{fill}=0.3 Pa, I_{PG}=4 kA corresponding to a field of 4.2 mT at 2 cm axial distance from the PG. *b)* evaluation of the plasma parameters using the line ratio method assuming an electron temperature of 12.5 eV. *c)* comparison of measured and calculated Balmer line emission and Fulcher emission with the relative contribution to the total intensity of the excitation channels. The plasma parameters, which are reported sideways the figure, are obtained by using the absolute emission methods.

The LOS measuring along the axis of the driver probes an area which includes the driver region and the expansion region, but the plasma emission in the driver is at least two order of magnitude more intense than the one in2 the expansion region (see figure 3.5), thus the contribution of the expansion region can be neglected. The

Balmer lines and Fulcher band emission are measured in the driver by OES and then used to evaluate the electron density n_e and the atomic to molecular density ratio n_D/n_{D_2}. In figure 4.2*a)* the Balmer line intensity and the Fulcher molecular emission are shown as a function of the RF power per driver (the power applied to the plasma by each driver is the same): the emission linearly increases with RF power for D_α, D_β and D_γ. The trend of the Fulcher band emission with the RF power is constant within the error bar: this can be explained by considering that the effective rate coefficient for the Fulcher transition is decreasing [88] with increasing electron density thus resulting in a roughly constant emission. The electron density and the atomic to molecular density ratio n_D/n_{D_2} calculated with the line ratio method (see section 3.2.1, 37) are shown in figure 4.2*b)* under the assumption of an electron temperature in the driver of 12.5 eV. The error bars on n_e and n_D/n_{D_2} are about 20% derived by statistical propagation of the error bars. The electron density increases with increasing RF power. The atomic to molecular density ratio also slightly increases and reaches the value of 0.32 at $P_{\mathrm{RF}} = 70\,\mathrm{kW/driver}$. For the case with P_{RF} = 70 kW/driver the evaluation is, in addition, carried out by using the absolute emission method (see section 3.2.1, 37) combined with YACORA calculations as shown in figure 4.2*c)*. The input parameters of the model giving the best matching with the experimental emission within 15% error bar are $n_{D_2} = 2.2 \cdot 10^{19}\,\mathrm{m^{-3}}$, $n_D = 6.6 \cdot 10^{18}\,\mathrm{m^{-3}}$, $n_{D_2^+} = 2.5 \cdot 10^{17}\,\mathrm{m^{-3}}$, $n_e = 2 \cdot 10^{18}\,\mathrm{m^{-3}}$, T_e=10.5 eV. The YACORA calculation gives a ratio of $n_D/n_{D_2} = 0.3$ which is in agreement with the value calculated with the line ratio method. The error bars on the densities are about 30% of the absolute value.
The plasma emission in the driver is mainly, i.e. ≈90%, given by direct ionization. The electron and atomic density as well as positive ion density linearly increase with the applied RF power. Thus, the particle flux from the driver to the expansion region increases with RF power.
The magnetic filter field influences the charged particle diffusion perpendicularly to the magnetic field lines. In the case of the ELISE plasma in the drivers, neither electrons nor positive ions are magnetized, thus the effect observed on the plasma is due to the diffusion properties of the plasma in the expansion region. The electron diffusion gets reduced with increasing magnetic field strength, thus effecting the electron density in the driver region. Consequently, the Balmer line intensity measured by OES in the drivers is affected by the magnetic field strength: the emission of H_β for three different power scans performed in hydrogen at I_{PG} =0 kA, 1.8 kA and 2.5 kA is shown in figure 4.3*a)*. The line intensity in the driver increases by increasing the filter

field strength, which is proportional to I_{PG}. The diffusion of the plasma perpendicularly to the magnetic field lines is reduced thus resulting in an increase of electron density n_e measured in the driver region. Consequently to the higher electron density, the atomic to molecular density ratio n_H/n_{H_2} increases. The analysis performed with the OES absolute emission method is shown in figure 4.3*b)*, where in the top part the electron density is shown and in the bottom part the corresponding atomic to molecular density ratio is plotted.

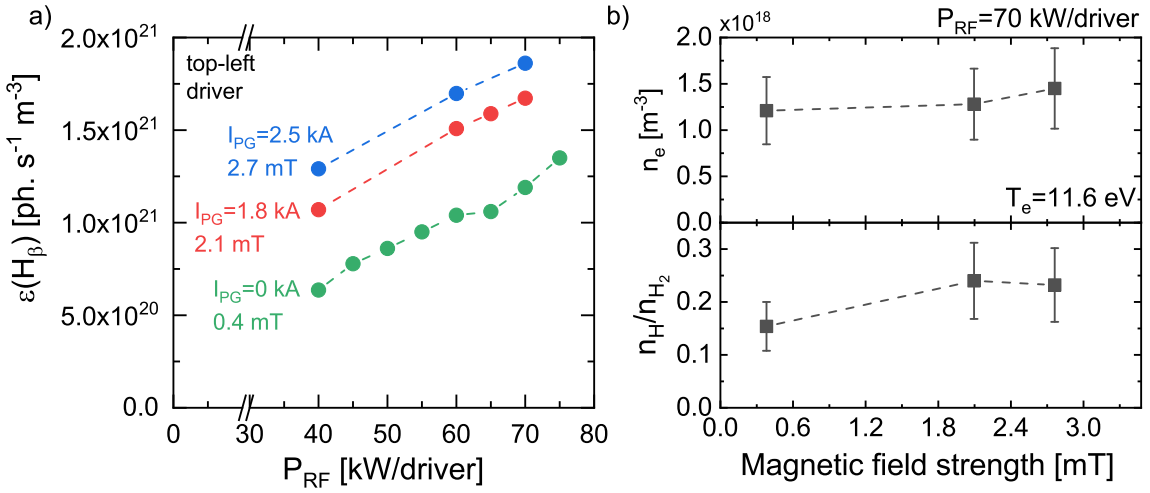

Figure 4.3: *a)* Line intensity of the Balmer line H_β measured by OES with the relative error bars during an RF power scan for different values of magnetic field strength. Parameters of the scan: H, p_{fill}=0.3 Pa. *b)*: evaluation of n_e and n_H/n_{H_2} using the absolute emission method. Values plotted as a function of the magnetic field strength at 2 cm axial distance from the PG.

In the above considerations, the analyses are carried out for one driver (ZD1, the top-left driver in figure 3.4). Differences in the emission are not observed between left and right drivers or between top and bottom drivers, when using the same RF power setting of the generators. This is experimentally observed in figure 4.4*a)*, where the emission of H_α measured on the top left driver ZD1 is plotted as a function of the emission measured on the bottom left driver ZD3. The gray shaded area is the experimental uncertainty of 10% around the bisector line (shown in black). The pulses shown are about 4000 pulses performed between 2017 and of 2019. The data points include a wide range of operational parameter variations in RF power, magnetic field for the two isotopes. The intensity of the H_α line is in most of the case identical, within the 15% error bars, between top and bottom drivers, thus, when the RF power set is the same between the two generators, the top and bottom drivers couple the same RF power to the plasma. The symmetry is tested also between left and right

drivers, i.e. connected with the same RF generator. In figure 4.4*b)* the emission measured in the right driver is plotted as a function of the emission measured in the left driver for the top pair of drivers (left-hand side of figure 4.4*b)*) and the bottom pair of drivers (right-hand side of figure 4.4*b)*). The emission is, also in this case, the same within the 15% error bar, thus the power coupled in the drivers powered by the same generator is distributed equally between left and right drivers. The comparison is performed on the Balmer line emission, which is determined by the plasma parameters, thus if the line emission measurements in the drivers are the same within the error bars, the plasma parameters are the same for each driver.

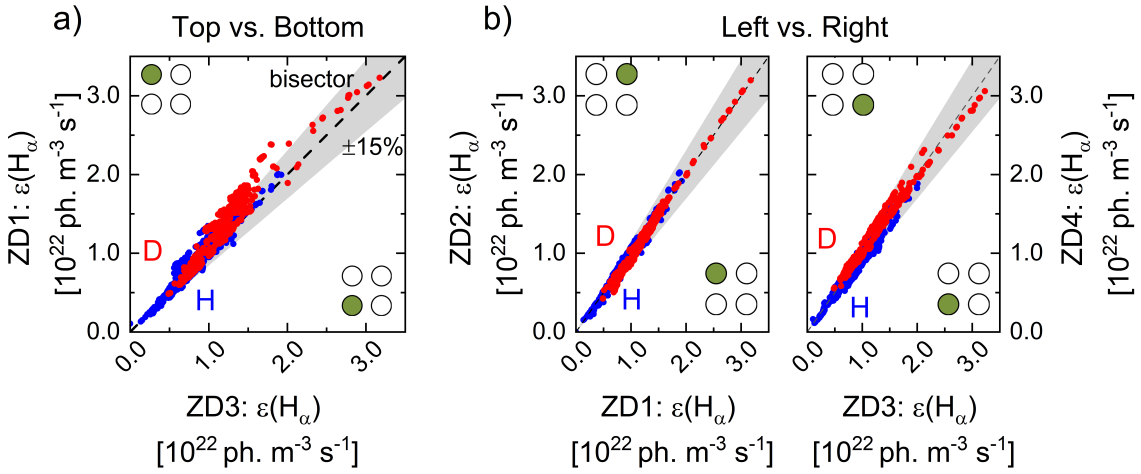

Figure 4.4: *a)* OES H_α emission measured in the driver ZD3 (bottom-left driver) as a function of the OES H_α emission measured in the driver ZD1 (top-left driver). Red points for deuterium pulses and blue points for hydrogen pulses. The black dashed line and the grey shaded represent the bisector and the ±15% error bar, respectively. *b)* OES H_α line intensity measured on the drivers on the right as a function of the line intensity measured on the drivers on the left. On the left part of the figure the top pair of drivers is shown whereas on the right part the bottom pair of drivers. The black dashed line and the grey shaded represent the bisector and the ±15% error bar, respectively.

The biasing of the PG and the extraction phase do not affect the OES emission measured in the driver (not shown here) because the effect on the plasma parameters is localized in the vicinity of the PG.

4.2 Plasma properties close to the extraction region

The plasma generated in the drivers diffuses into the expansion region and the plasma drift strongly modifies the charged particle fluxes towards the PG. The magnetic filter

field, as discussed in the introduction (see section 2.4), reduces the diffusion perpendicularly to the field lines and consequently the flux of charged particles towards the PG. The only magnetized particle species are the electrons and the magnetic filter field directly influences the electron, whose temperature T_e strongly decreases. The evolution of the electron temperature measured with the RF-compensated Langmuir probe at the center of the beamlet group as a function of the magnetic filter field strength is plotted in figure 4.5*a)*. Without magnetic field, i.e. at I_{PG}=0 kA and without the external magnets, the electron temperature is about 8 eV, slightly lower than in the driver region. The temperature decreases to about 2 eV for magnetic field strength higher than 1 mT.

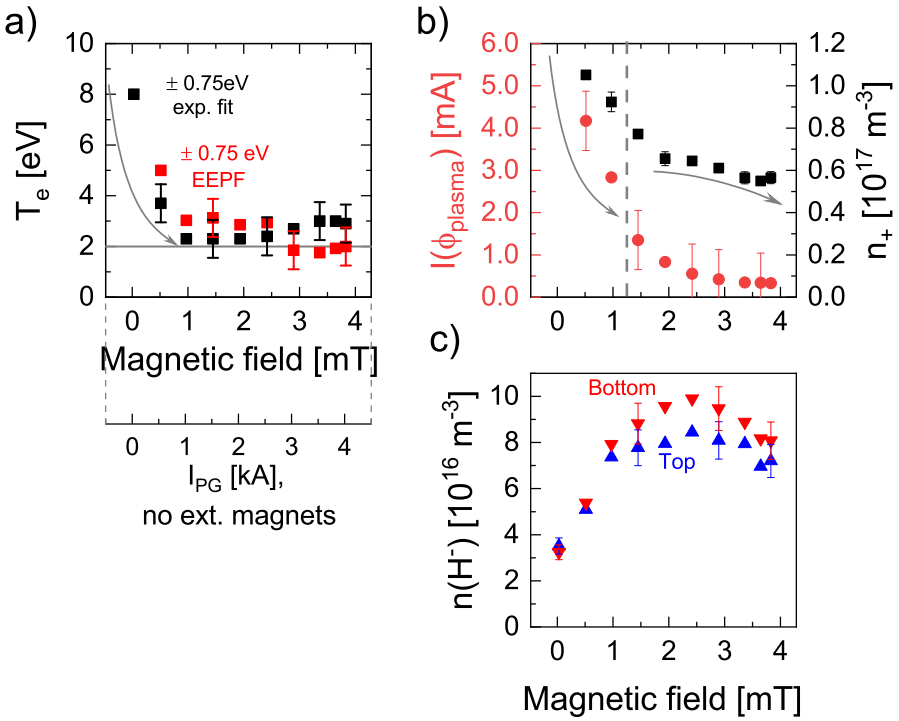

Figure 4.5: *a)* Electron temperature obtained from the IV curve measured by the RF-compensated movable probe positioned at 307 mm, i.e at the center of the upper beamlet group. T_e is calculated with two methods: with the EEPF and with the exponential fit on the IV curve. In both cases the error bar is about 0.75 eV. *b)* Current at the plasma potential (red) and positive ion density (black) measured by the RF-compensated movable LP measurements. *c)* Negative ion density measured by CRDS for the two LOS available. Values plotted as a function of the magnetic field strength measured at 2 cm axial distance from the PG. Parameters: H, p_{fill}=0.3 Pa, P_{RF} =60 kW/driver, I_{bias} =35 A, no external magnets, potential rods installed.

The reduction of the positive ion density and of the electron flux with increasing magnetic filed strength is shown in figure 4.5*b)*, where the current at the plasma po-

tential, i.e. $I(\phi_{\text{plasma}})$), and the positive ion density n_+ are shown in red and black, respectively. At 3.8 mT the flux of electrons, which is proportional to $I(\phi_{\text{plasma}})$, asymptotically decreases to a value that is about 10 times lower than without magnetic field. At strong magnetic field values the probe characteristic is symmetric with respect to the plasma potential, thus the plasma is ion-ion. For a magnetic field strength higher than 1 mT, the electron temperature can be considered constant, thus the decrease observed in the quantity $I(\phi_{\text{plasma}})$ is caused by a decrease of the electron density. The evolution of the positive ion density shows an initial decrease of about 40% at 1.9 mT and a further decrease at higher values of magnetic filter field strength. The relative variation of $I(\phi_{\text{plasma}})$ and the positive ion density are different with the variation of the magnetic field because surface-produced negative ions becomes relevant, thus quasi-neutrality is kept by means of surface-produced negative ions and electrons are strongly reduced.

Negative ion production by surface production is relevant when the electron stripping process (see figure 2.6) in the plasma is reduced, namely for low electron density and low electron temperature. The trend of the negative ion density measured by CRDS is shown in figure 4.5*c)*: up to 1.9-2.4 mT, the negative ion density measured by CRDS increases. For a magnetic field higher than 2.4 mT, the negative ion density decreases. A possible explanation for the negative ion density reduction at high magnetic field is connected with the reduction of positive ion density: the emission of negative ions from the PG is hindered due to a lack of space charge compensation of positively charged particles in the plasma. A possible reduction of the atomic density may also concurrently take place thus reducing the emission of negative ions: it is not possible to exclude this possibility with the actual diagnostic setup because it is not possible to measure the atomic flux or the atomic density.

The plasma emission is strongly affected by the magnetic field strength: in figure 4.6 the line emission of H_β is shown for the different OES LOS available in the expansion region as a function of the magnetic field strength. The H_β intensity is at maximum without magnetic filter field applied and it decreases of about 50% for a magnetic filter field strength of 1 mT. Between 1.3 mT and 2.5 mT the emission is constant whereas it steadily decreases for values higher than 2 mT. The above mentioned description is valid for all the LOS shown in figure 4.6 except for the horizontal LOS XL-1 positioned at a vertical position of +100 mm from the ion source center: in this case the H_β line intensity steadily decreases with increasing magnetic field strength. The plasma emission at low values of magnetic field, i.e. lower than 1.2 mT, is dominated by ionizing processes due to the the high electron density and temperature. Thus a

decrease of line intensity is directly correlated with a decrease of electron density in the plasma. For magnetic field values higher than 1.2 mT, the emission is dominated by recombining processes. Thus, the line emission is correlated to the positive ion density and to the negative ion density in the plasma.
To determine to which extent each excitation channel contribute to the total line intensity, OES measurements have to be combined with collisional radiative models.

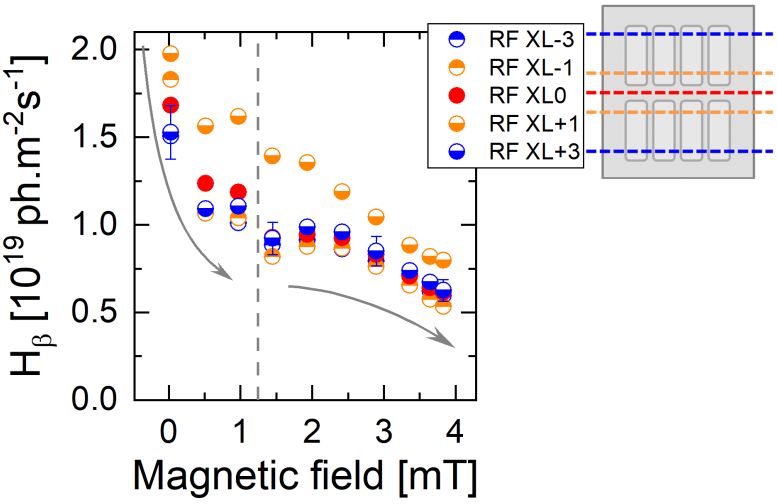

Figure 4.6: H_β emissivity from OES in the expansion region as a function of the I_{PG} current. Same parameters of figure 4.5.

Indications on the charged particle flux on the ion source segments can be drawn by using the electrical measurements on the bias plate segments and on the potential rods. The current I measured on these components is proportional to the flux of particles Γ and to the area A of the components, i.e. $I = eA\Gamma$. Thus, the current measured on these components is determined by the potential applied compared to the plasma potential, i.e. source potential for the bias plate and U_{bias} for the rods, and by the charged particle density. In figure 4.7*a)* and in figure 4.7*b)*, the bias plate current I_{BB} and the rod current I_{rod} for the top and bottom segment of the ion source are plotted as a function of the magnetic filter field strength, respectively. The bias plate current show a lower absolute value without magnetic field than for the case at 1 mT. For magnetic field values higher than 1 mT, the current steadily decreases. The values for the top and bottom segment are close in absolute values. The rod current shows a different behavior for the two parts, i.e. top and bottom. The current measured on the upper potential rods shows a low value without magnetic field, then it increases up to the maximum value at 1.5 mT and then it decreases with increasing magnetic filter field. The current measured on the lower potential rods is instead roughly constant with applied magnetic field whereas for the case at 0 mT the current

collected coincide with the one measured on the top segment.
The bias plate is at source potential, i.e. at 0 V with respect to the PG potential, thus positive ions in the plasma where $\phi_{\text{plasma}} \geq 10\,\text{V}$ are accelerated into it. Electrons can reach the bias plate, and then contribute to the bias plate current, only if they have an energy comparable to the difference between plasma potential ϕ_{plasma} and wall potential: this is the case for the pulse performed without magnetic field, where energetic electrons (≈8 eV see figure 4.5*a)*) can reach the bias plate and contribute to the current thus decreasing the I_{BB} absolute value. For a magnetic field higher than 0.9 mT the electron contribution is no longer relevant, due to the low T_e, and a decrease of I_{BB} is related to a decrease of positive ion density. The trend of the current in the two segments is comparable, but at high magnetic field value $I_{\text{BB}}^{\text{top}}$ is higher than $I_{\text{BB}}^{\text{bot}}$ of about 30%: the plasma drifts influences the positive ion distribution thus resulting in an asymmetric current on the bias plate segments.

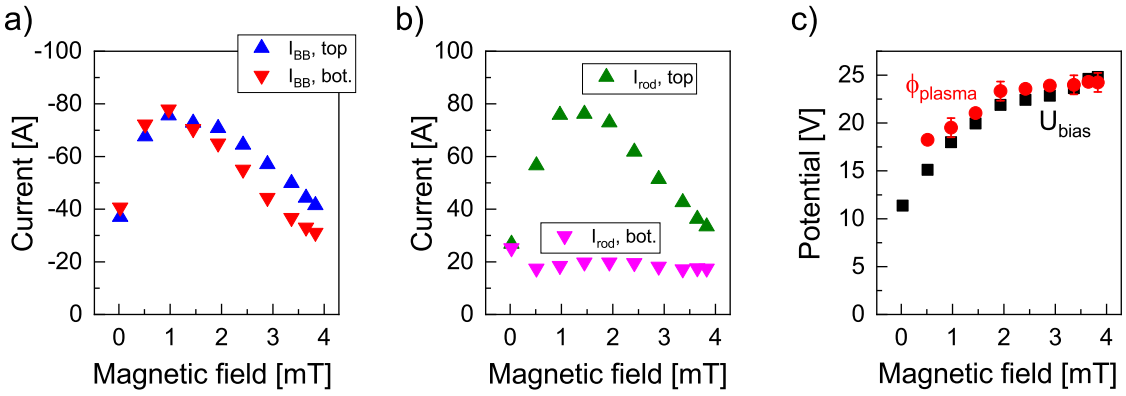

Figure 4.7: *a)* Current collected on the bias plate segments (top in blue, bottom in red) and in *b)* current collected on the rod segments (top in green, bottom in pink) as a function of the magnetic field strength. *c)* Plasma potential and U_{bias} as a function of the magnetic field strength. The plasma potential is calculated from the RF-compensated movable LP measurements at the top of the ion source whereas U_{bias} is given by the bias power supply. Same parameters of figure 4.5, values measured during the RF only phase, $I_{\text{bias}} = 35\,\text{A}$.

The current collected on the PG is given by $I_{\text{plasmaPG}} = I_{\text{bias}} - I_{\text{rods}}$. In the case shown in figure 4.7*b)*, $I_{\text{bias}} = 35\,\text{A}$, i.e. $I_{\text{rod}} > I_{\text{bias}}$ and the current collected on the I_{plasmaPG} is negative, thus given by collection of positive ions at the PG and/or emission of negative ions from the PG surface. The interpretation of the current will be discussed in section 4.2.1. The relevant point in figure 4.7*b)* is the strong asymmetry in current between top and bottom rod segment, which illustrates the strong asymmetry of electron flux between top and bottom side of the ion source, being $I_{\text{rod}}^{\text{top}}$ between two and four times higher than $I_{\text{rod}}^{\text{bot}}$. Without magnetic field the currents measured

on the rod segment coincide and then depart as the magnetic field is applied: without magnetic field, plasma drifts are not established and the flux of particles from the driver towards the PG, which is top-bottom symmetric as demonstrated in section 4.1, gives a current collected on the rods which is symmetric. The asymmetric behavior of the rod current is caused by less effective collection of electrons at the bottom of the ion source: possible reasons are a low electron density at the bottom of the source and/or a higher (compared to the top) plasma potential, thus resulting in a different potential drop at the rods $U_{\text{bias}} - \phi_{\text{plasma}}$.
In figure 4.7*c)* the evolution of the PG and rod potential, i.e. U_{bias}, is shown as a function of the applied magnetic field strength. The plasma potential ϕ_{plasma} measured by the movable RF-compensated LP at the center of the beamlet group is shown as well in figure 4.7*c)*. U_{bias} steadily increases with increasing the magnetic field strength. Due to the fixed current drawn by the biasing power supply, i.e. I_{bias}, the PG potential is close to the plasma potential, i.e. $\phi_{\text{plasma}} \approx U_{\text{bias}}$. Without magnetic field, the electron density and temperature in the plasma are high and consequently the electron flux towards PG and rods is high, thus the potential applied by the bias power supply is low, i.e. U_{bias}=12 V. To collect the same current at higher magnetic field, when n_e and T_e are strongly decreased, the power supply applies a higher potential, i.e. U_{bias}=25 V at 3.8 mT. The U_{bias} follows the plasma potential ϕ_{plasma} and the difference between the two is determined by the equilibrium of fluxes of the charged species, namely flux of electrons collected at the PG, flux of positive ions collected at the PG and flux of negative ions emitted from the PG (surface emission).

4.2.1 Effect of the potential rods on the plasma

The installation of the potential rods improved the symmetry of the co-extracted electrons and the stability for long pulses [80]. In figure 4.8, the effect of the installation of the potential rods on the bias plate current I_{BB} is shown for two pulses with similar operational parameters, with a slightly higher I_{PG} for the case shown in *a)*, i.e. a filter field of 2.3 mT instead of 2.2 mT. For the magnetic field strength under investigation, I_{BB} is proportional to the flux of positive ions since the contribution of electrons can be neglected. For the case shown in *a)* an asymmetry between top and bottom is clearly visible on the bias plate current, being $I_{\text{BB}}^{\text{top}}$ about 60% higher than $I_{\text{BB}}^{\text{bot}}$. In figure 4.8*b)* and *c)*, the time-trace of the bias plate current and the time-trace of the rod current are plotted: in this case, with the potential rods installed, the current on the bias plate segments is top-bottom symmetric thus showing an improvement

on the positive ion density symmetry. On the other hand, $I_{\mathrm{rod}}^{\mathrm{top}}$ is about four to five times higher than $I_{\mathrm{rod}}^{\mathrm{bot}}$. Since all potential rods are at the same potential U_{bias}, a top-bottom asymmetry of the plasma potential would cause an asymmetric current onto the rods. A similar effect on the current can be given however, by a different electron density between top and bottom of the source. On this point, measurements of the electron density and of the plasma potential are necessary to understand which is the cause, or causes, of the rod current asymmetry.

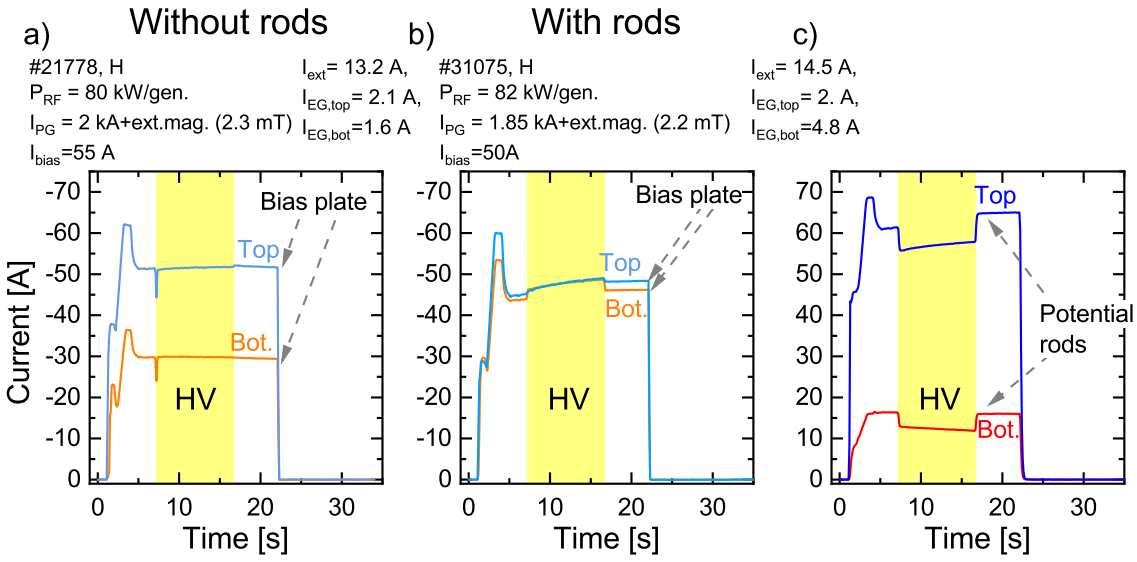

Figure 4.8: Bias plate current measured for each segment, pulse performed without potential rods installed in *a)* and at similar setup parameters with potential rods in *b)*. In *c)* the rod current for the two segments is shown in blue for the upper rods and in red for the lower rods.

For the case with the potential rods at PG potential, i.e. at U_{bias}, the results of a careful analysis on the current balance in the three electric component are shown in the following. For each electric component the net current is measured ($I_{\mathrm{rod}}^{\mathrm{top}}$ and $I_{\mathrm{rod}}^{\mathrm{bot}}$) or calculated ($I_{\mathrm{plasmaPG}} = I_{\mathrm{bias}} - I_{\mathrm{rod}}$). As already mentioned, the current on the PG results from charged particle fluxes integrated over the PG surface. The particle fluxes contributing to the net current are electrons onto the PG ($e\Gamma_{\mathrm{e}}$), positive ions collected on the PG ($(-e)\Gamma_{+}$) and negative ions emitted from the PG surface ($e(-\Gamma_{H^-})$). The total current I measured on a surface is then:

$$I = A(e\Gamma_{\mathrm{e}} + (-e)\Gamma_{+} + e(-\Gamma_{H^-})) = Ae(\Gamma_{\mathrm{e}} - \Gamma_{+} - \Gamma_{H^-}) \tag{4.1}$$

where A is the surface of the PG not covered by bias plate; the area of the apertures is not included. A positive net current represents the case where the flux of electrons is

the dominant contribution to the current while a negative net current represents the case where the fluxes of positive ions and negative ions are the dominant contribution to the current. In the latter case, it is not possible to distinguish the emission of negative ions from the collection of positive ions.
The rod current ($I_{\mathrm{rod}} = I_{\mathrm{rod}}^{\mathrm{top}} + I_{\mathrm{rod}}^{\mathrm{bot}}$) is here assumed to be dominated by electrons collected on the surface of the potential rods: this hypothesis is supported by the orientation of the rods, i.e perpendicular to magnetic field lines, thus intercepting the electrons gyrating along the field lines.

To gain a deeper insight on which contribution determines the current at the rods

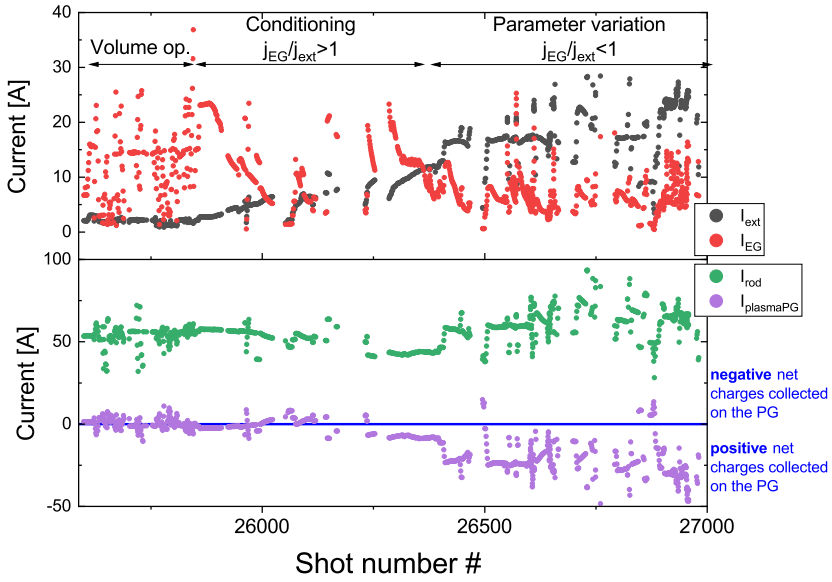

Figure 4.9: Evolution during the conditioning phase of the extracted ion current I_{ext} in black, of the co-extracted electron current I_{elec} in red, of the current on the rods I_{rod} in green and of the current collected on the PG I_{plasmaPG} in purple.

and at the PG, I_{rod} and I_{plasmaPG} are studied along with the evolution of the source performance, i.e. co-extracted electrons and extracted negative ion current, during a Cs conditioning phase starting from a non caesiated source (the ion source was not completely Cs-free because the walls and the grids were not cleaned). In figure 4.9 the trend of the extracted negative ions I_{ext}, the co-extracted electron current I_{elec}, the current collected on the rods I_{rod} and the current measured on the PG $I_{\mathrm{plasmaPG}} = I_{\mathrm{bias}} - I_{\mathrm{rod}}$ are shown. The value of I_{bias} is chosen by the operator and it is usually in a range between 5 A and 80 A. The value are given for the RF-only phase.

During the volume operation phase, electrons are the dominant negatively charged species thus I_{elec} is much higher than I_{ext}. In this phase, $I_{\text{bias}} \approx I_{\text{rod}}$ being then the current almost entirely collected on the rods while I_{plasmaPG} is almost zero, suggesting that the flux of electrons and positive ions are balanced. The Cs conditioning phase is characterized by a steady decrease of the co-extracted electrons with an increase of the extracted negative ion current. At the end of the conditioning phase I_{plasmaPG} is negative, i.e. the emission of negative and/or the collection of positive ions are relevant contributions to the current measured at the PG: when surface-produced negative ions are efficiently produced, the flux of negative ions emitted from the PG plays a relevant role in the current balance. By assuming an emitted negative ion current density from the PG of 400A/m^2 [50] (for ideal PG caesiation) and a PG surface[11] of approximately 0.13 m^2, the estimated negative ion emitted current is of -50 A. The value obtained is of the same order of magnitude of the current I_{plasmaPG}.
In the last phase, when the source is conditioned and parameter variations are performed, the current I_{plasmaPG} is negative and shows variations with the source performances. The few points where $I_{\text{plasmaPG}} > 0$ are performed with a $I_{\text{bias}} \geq 80\,A$, thus in a strongly electron attracting regime.
To demonstrate that the current I_{plasmaPG} is correlated to the negative ion density and to the positive ion density, I_{plasmaPG} is plotted as a function of the extracted current I_{ext} and of I_{BB} in figure 4.10*a)* and *b)*, respectively. The last two quantities are related to the negative ion density and to the positive ion density, respectively. The color scale indicates the ratio $I_{\text{EG}}/I_{\text{ext}}$ of each pulse: the gray points indicate cases in volume operation, i.e. without Cs (these pulses are additionally encircled in red in figure 4.10*a)* and *b)*), or with an electron-ion ratio higher than one, i.e. bad Cs conditioning.
For volume operation, the current collected on the PG is around 0 A. With increasing positive ion density, i.e. the current measured on the bias plate I_{BB}, the current collected on the PG is more negative as shown in 4.10*a)*. In figure 4.10*b)* the current I_{plasmaPG} is plotted as a function of the extracted current I_{ext}, which is proportional to the negative ion density n_{H^-} in the plasma. With the improvement of the performances, i.e. with increasing extracted current, the current collected at the PG decreases to -60 A. In both figures only a few points are at $I_{\text{plasmaPG}} \geq 0$ A, for a well conditioned source and high extracted negative ion current and high positive ion flux

[11] $8\times[(0.32\,\text{m} \times 0.09\,\text{m})\text{-}(5\times16\times\pi\ (0.007\,\text{m})^2)] = 0.132\,\text{m}^2$ where 8 is number of beamlet groups, the first parenthesis is the beamlet group surface (0.32 m is the beamlet group height and 0.09 is the beamlet group width) and the second parenthesis the aperture surface, to be subtracted.

onto the PG. Those pulses are performed with a strong biasing of the PG, i.e. with $I_{\mathrm{bias}} \geq 80\,\mathrm{A}$. The proportionality factor between I_{plasmaPG} and I_{ext}, I_{BB} include the area where those current are calculated, namely the extraction area for I_{ext}, the PG surface for I_{plasmaPG} and the bias plate surface for I_{BB}. Moreover also the acceleration of charged particles in the sheath influences the current collected on the bias plate and on the PG.

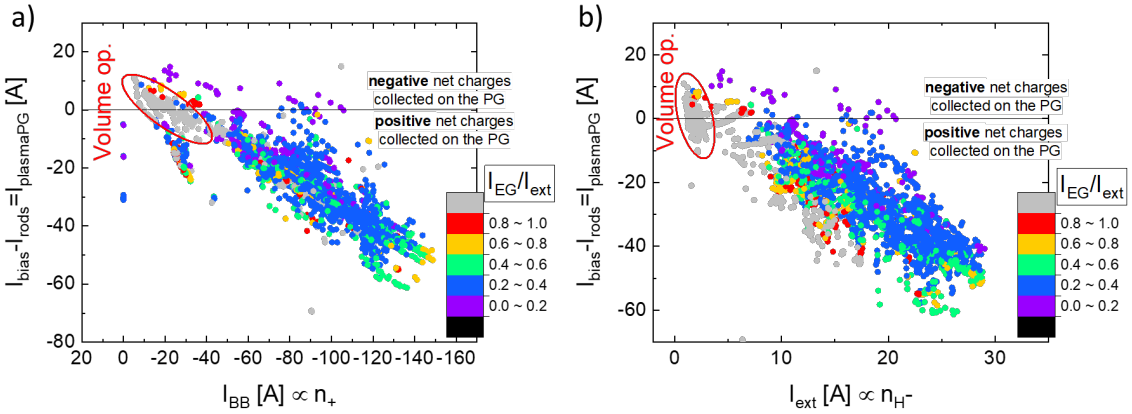

Figure 4.10: The current collected on the PG I_{plasmaPG} as a function of the current measured on the bias plate I_{BB} in *a)* and as a function of the extracted negative ion current I_{ext} in *b)*. In the plots 6800 pulses performed since the installation of the rods in June 2017 are shown in a color scale that indicate the ratio $I_{\mathrm{EG}}/I_{\mathrm{ext}} \leq 1$, namely with a low amount of co-extracted electrons. The gray points indicate cases in volume operation, i.e. without Cs, encircled in red in figure 4.10*a)* and *b)*, or with an electron-ion ratio higher than one, i.e. bad Cs conditioning.

The present results demonstrate that in presence of the potential rods the electrons are collected preferentially on the rods and the emission of negative ions and collection of positive ions are the dominant contribution for the current collected on the PG I_{plasmaPG}.

A scheme of the working principle of the rods in comparison with the situation without potential rods is shown in figure 4.11. The current collected on the rods decreases during the HV phase with respect the the RF phase on both rod segments as shown in figure 4.8*c)*. During the HV phase, negative ions are extracted at the PG apertures and it can be assumed that these are partially substituted by electrons to keep the quasi-neutrality of the plasma. Thus, the flux of electrons to the PG is increased and the current collected on the PG increases (see equation 4.1) which in turn gives a decrease of the current measured on the rods, since the bias power supply draws the same current I_{bias} over the pulse length.

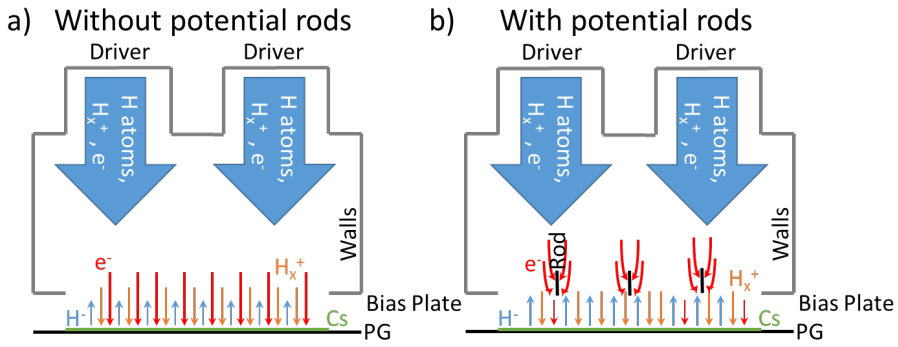

Figure 4.11: Scheme of the working principle of the potential rods. *a)*: without potential rods the flux of electrons, positive ions and emission of negative ions contribute to the PG current which is equal to I_{bias}. *b)*: with potential rods the current measured at the PG is not I_{bias}. The flux of positive ions and negative ions is the relevant contribution to I_{plasmaPG}.

As a general behavior, e.g. see figure 4.8*c)*, the current collected on the rod segment is not symmetric: $I_{\text{rod}}^{\text{bot}}$ is about 10%-20% of $I_{\text{rod}}^{\text{top}}$ and, at the same time, the co-extracted electrons on the bottom EG segments $I_{\text{EG}}^{\text{bot}}$ is usually higher and more unstable compared to the one one the top EG segment $I_{\text{EG}}^{\text{top}}$. These two experimental observations suggest that U_{bias} is not adequate to reduce the electron density on the bottom half of the ion source. Concerning the potential rods, having three different power supplies, one for each biased element (PG, top rods and bottom rods) would be beneficial to adjust the biasing to the local plasma properties and even increase it, if necessary, during the extraction phase.

4.2.2 Local plasma parameters and co-extracted electrons

In this section the relation between electron flux, determined by the electron density and the sheath at the PG, i.e. $\phi_{\text{plasma}} - U_{\text{bias}}$, and the co-extracted electron current is investigated. The main tool is the movable RF-compensated Langmuir probe, whose results, namely positive ion density n_+, current at the plasma potential $I(\phi_{\text{plasma}})$ and plasma potential ϕ_{plasma}, are correlated with the co-extracted electron current I_{EG}. The measurement domain of the movable Langmuir probe is a vertical stripe of plasma of about 20 cm height and few tens of mm width around the probe tip. The probe can reach the center of the third beamlet group from the left on the top of the ion source (see figure 3.7).

The results of the probe are obtained at about 2 cm axial distance from the PG, thus no information whether a double well is formed (due to the emission of negative ions, see section 2.4.3) and the depth of the well is accessible. Localized LP results are compared with the co-extracted electron current, which is integrated over a grid segment.

The plasma properties measured by the LP are different for RF and HV phase: in figure 4.12 the profiles of the positive ion density n_+, the current at the plasma potential $I(\phi_{\text{plasma}})$ and the plasma potential ϕ_{plasma} are shown in *a)*, *b)* are *c)*, respectively, for the RF phase and the HV phase. In every subfigure the dashed vertical lines indicates the bias plate position whereas the yellow shaded area is the extraction area given from the edge of the uppermost aperture to the edge of the lowermost aperture. During the RF phase, the positive ion density is between 0.8 and $1.2 \cdot 10^{17}\text{m}^{-3}$ in front of the bias plate, then n_+ shows a dip in correspondence to the PG, but the value is then recovered above the extraction area, where the density of about $1.1 \cdot 10^{17}\text{m}^{-3}$. The profile of the current at the plasma potential $I(\phi_{\text{plasma}})$, shown in figure 4.12*b)*, is characterized by a high value in front of the bias plate, i.e. 2 to 4 mA, which then decreases above the extraction area. The lowest value measured during the RF phase is reached at about 200 mm, i.e. in the center of the beamlet group.

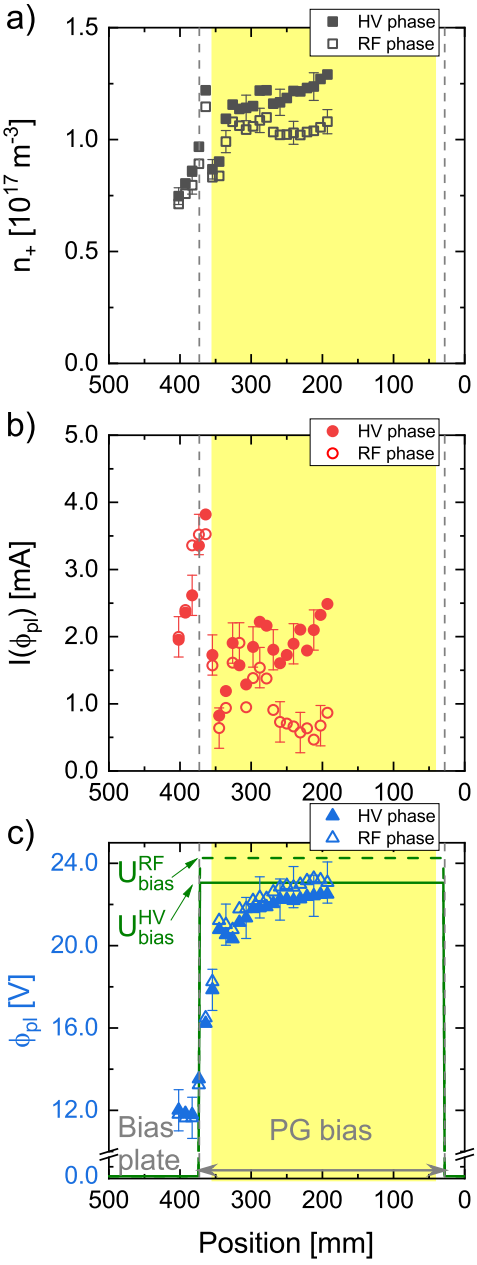

Figure 4.12: Vertical profile of the positive ion density in *a)*, of the $I(\phi_{\text{plasma}})$ in *b)* and of the plasma potential ϕ_{plasma} in *c)*. The dashed gray lines indicate the edges of the bias plate and the yellow shaded area the extraction area defined by the edges of the uppermost and lowermost apertures in the beamlet groups. Empty symbols indicate the RF phase while full symbols the HV phase.

The decrease of $I(\phi_{\text{plasma}})$ above the extraction area in comparison with the bias plate shows the beneficial effect of the PG biasing on the electron density in the vicinity of the extraction area.

The plasma potential ϕ_{plasma} above the bias plate is about 12 V and it increases to approximately 1-2 V lower than U_{bias} above the PG.

During the HV phase, $I(\phi_{\text{plasma}})$ at 200 mm is two times higher than during the RF phase and the positive ion density increases of about 20%. ϕ_{plasma} and U_{bias} are lower during the HV phase of about 1 V than during the RF-only phase.

To study the correlation between electron flux towards the PG and co-extracted electrons, the fluxes of charged particles at the PG need to modified by acting on the PG biasing, i.e. on the bias current I_{bias}. The positive ion density n_+, the current at the plasma potential $I(\phi_{\text{plasma}})$, and the sheath variation, i.e. $U_{\text{bias}} - \phi_{\text{plasma}}$ are shown in figure 4.13 as a function of the I_{bias} current.

For what concerns n_+ and $I(\phi_{\text{plasma}})$ measured during the RF phase, no variation of the measured quantities is observed within the error bars for the investigated range of I_{bias} whereas both quantities decrease with I_{bias} during the HV phase. As shown in 4.13*c)*, U_{bias} increases with I_{bias} and ϕ_{plasma} has a similar trend as U_{bias} (not shown). However, the quantity $U_{\text{bias}} - \phi_{\text{plasma}}$ increases. The PG sheath is electron repelling but it gets less electron attracting with increasing I_{bias}.

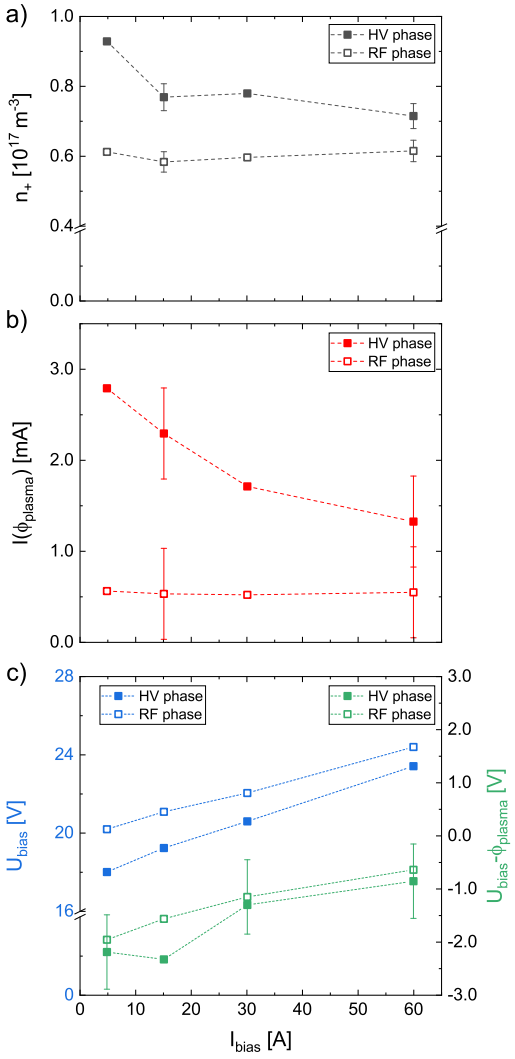

Figure 4.13: Positive ion density n_+ in *a)*, current at the plasma potential $I(\phi_{\text{plasma}})$ in *b)* and in *c)* U_{bias} in blue and $U_{\text{bias}} - \phi_{\text{plasma}}$ in green as a function of I_{bias}. The scan was performed in H at $p_{\text{fill}} = 0.3$ Pa and $I_{\text{PG}} = 1.6$ kA (1.5 mT) without ext. magnets, P_{RF}=60 kW/driver, $U_{\text{ext}} = 9$ kV, $U_{\text{acc}} = 45$ kV. Empty symbols show the measurements performed during the RF-phase and full ones during the HV phase.

As it can be seen by comparing *b)* and *c)*, $I(\phi_{\text{plasma}})$ (mainly given by electron density) decreases with increasing $U_{\text{bias}} - \phi_{\text{plasma}}$ only for the measurement performed during the HV phase. Since $I(\phi_{\text{plasma}})$ and n_+ are unchanged during the RF phase, then the plasma composition at the measurement position is unchanged. On the other hand, the plasma and PG potential are influenced, thus it can be concluded that the particle flux at the PG is modifies, but the plasma composition is not affected by the different flux at the PG. This is not the case with extraction, since a variation of the charged particle density is observed with a variation of the sheath properties.

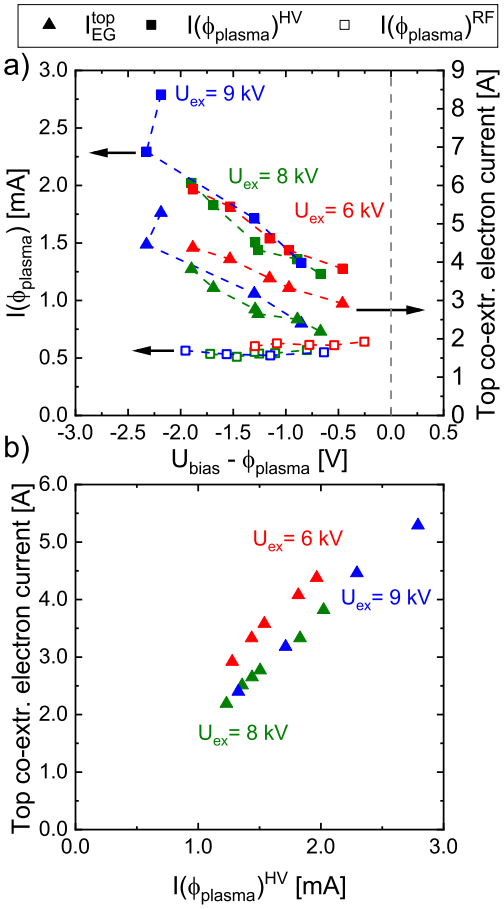

Figure 4.14: *a)* Current at the plasma potential $I(\phi_{\text{plasma}})$ and co-extracted electron current as a function of $U_{\text{bias}} - \phi_{\text{plasma}}$. Empty symbol for the RF phase and full symbols for the HV one. *b)* Co-extracted electron current $I_{\text{EG}}^{\text{top}}$ as a function of $I(\phi_{\text{plasma}})^{\text{HV}}$ for the extraction voltage U_{ext}=6 kV, 8 kV and 9 kV.

On the plasma side, a variation of electron density is observed with a different PG sheath during the HV phase. The next step consists on studying the evolution of the co-extracted electron current. In figure 4.14*a)* the evolution of $I(\phi_{\text{plasma}})$ and of the co-extracted electron current on the upper EG segment $I_{\text{EG}}^{\text{top}}$, i.e. on the same ion source side as the movable LP, is shown as a function of the PG sheath $U_{\text{bias}} - \phi_{\text{plasma}}$. The scan is performed at 6 kV, 8 kV and 9 kV extraction voltage, which are typical values used during the experimental campaigns at ELISE. $I(\phi_{\text{plasma}})$ measured during the RF phase (empty symbols) is not influenced by the potential difference at the PG, whereas during the HV phase it decreases with decreasing $U_{\text{bias}} - \phi_{\text{plasma}}$. The co-extracted electron current shows a similar trend as $I(\phi_{\text{plasma}})^{\text{HV}}$. To check this correlation, in figure 4.14*b)* the co-extracted electron current is plotted as a function of the $I(\phi_{\text{plasma}})^{\text{HV}}$: the two quantities are linearly correlated, thus demonstrating that the co-extracted electrons are correlated with the electron density measured in the plasma during the HV phase. The electron density decreases if the PG sheath, i.e.

$U_{\text{bias}} - \phi_{\text{plasma}}$, gets closer to the electron attracting regime.

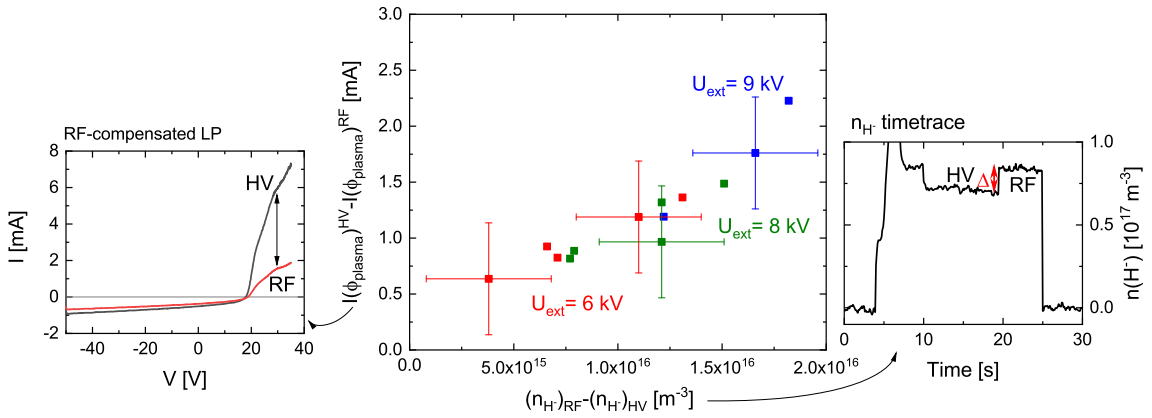

Figure 4.15: Variation of $I(\phi_{\text{plasma}})$ due to the HV phase as a function of the variation of negative ion density $n(H^-)$ during the HV phase. The I_{bias} scan is repeated for three different values of extraction voltage U_{ext}=6 kV, 8 kV and 9 kV.

Locally, the increase of $I(\phi_{\text{plasma}})$, which is assumed to be determined mainly by the electron density in plasma, during the HV phase with respect to the RF phase is caused by an increase of electron density in the plasma due to the extraction of negative ions. This is quantitatively demonstrated in figure 4.15, where the relative increase of $I(\phi_{\text{plasma}})$ in the HV phase is plotted as a function of the amount of negative ions removed by the HV phase, i.e. $n(H^-)^{\text{RF}} - n(H^-)^{\text{HV}}$.

4.3 Vertical symmetry of the plasma parameters

The vertical symmetry is studied by changing the plasma drift, i.e. by acting on the magnetic filter field, hence on the I_{PG} direction. A dedicated experimental campaign was performed with reversed I_{PG} current, namely I_{PG} flowing vertically from the top to the bottom of the PG, thus the direction of the filter field is reversed. The external magnets have been turned accordingly, thus the resulting magnetic field is turned. This campaign is performed to investigate the following points:

- Possibility to investigate the plasma properties with the movable RF-compensated LP with reversed filter field, i.e. virtually at the bottom of the ion source.
- Possibility to study the Cs distribution, namely whether the amount of Cs is sufficient at the bottom half of the source to sustain the performance with the plasma parameters of the top half of the ions source when the drift direction is reversed.

- Possibility to check the grid alignment on the two halves of the grid segments. If the grid system has a systematic misalignment between two grids, either between the PG and the EG or between the EG and the GG, then this can explain observed differences between the beam divergence of the top and bottom beam segment[12]. In case of such misalignment, the beam properties would be similar when reversing the I_{PG} current.

The two different configurations of the I_{PG} are in the following called *standard* and *reversed* whereas *top* and *bottom* refer to the vertical position of the segments. Figure 4.16 shows a comparison of the two filter field configurations: the 2D maps of the beam power density and the BES divergence profiles are shown in *a)*, the time-traces of the extracted negative ion current and the co-extracted electron current for the two EG segment are shown in *b)* and time traces of the currents on the potential rods in the top ans bottom segment are shown in *c)*. Since the first pulse after turning the I_{PG}, the beam turns upside-down; the asymmetry between peak intensity is almost the same in the two configurations as well as the different beam width between segments. In the reversed configuration the accelerated current is slightly higher at the top beam segment (=standard bottom beam segment). There are about 1.4 A of difference in the total accelerated current, mainly lost in the standard top (=reversed bottom). The standard bottom, compared to the reversed top, has a slightly higher accelerated current by reversing the filter field. The beam, which is displaced downwards of about 4.5 cm in the standard configuration, is displaced upwards of about 0.5 cm in the reversed configuration. Thus, a displacement of about 2 cm between the ion source and the calorimeter over 3.5 m distance is estimated experimentally.
The total extracted negative ion current I_{ext} is lower of about 1 A in the reversed configuration, namely about 5% difference between the two cases. The asymmetry of the co-extracted electrons measured in the two EG segments (see figure 4.16*b)*) is reversed and the difference between the two configurations is at maximum of 0.5 A, i.e. about 10% difference between configurations. The rod segment current (see figure4.16*c)*) is also top-bottom reversed with a difference of about 4% for $I_{\mathrm{rod,top}}$ compared to $I_{\mathrm{rod,bot}}$ in the reversed configuration. $I_{\mathrm{rod,bot}}$ decreases of about 25% with respect to $I_{\mathrm{rod,top}}$ in the reversed configuration. The strong asymmetry between top and bottom rod segment is still present, though.

[12]The differences between top and bottom beam segments concern the peak intensity and the beam vertical and horizontal width. The differences, which are mentioned here and in the introduction, are discussed in chapter 5.

The immediate turn of the aforementioned quantities indicates that the Cs distribution plays a minor role in the plasma and beam asymmetry compared to the plasma drifts for a well conditioned source and for short pulses. A full Cs redistribution due to different plasma properties would take up to several days, thus the effect of the new magnetic field configuration on the beam would take place over a longer time scale.

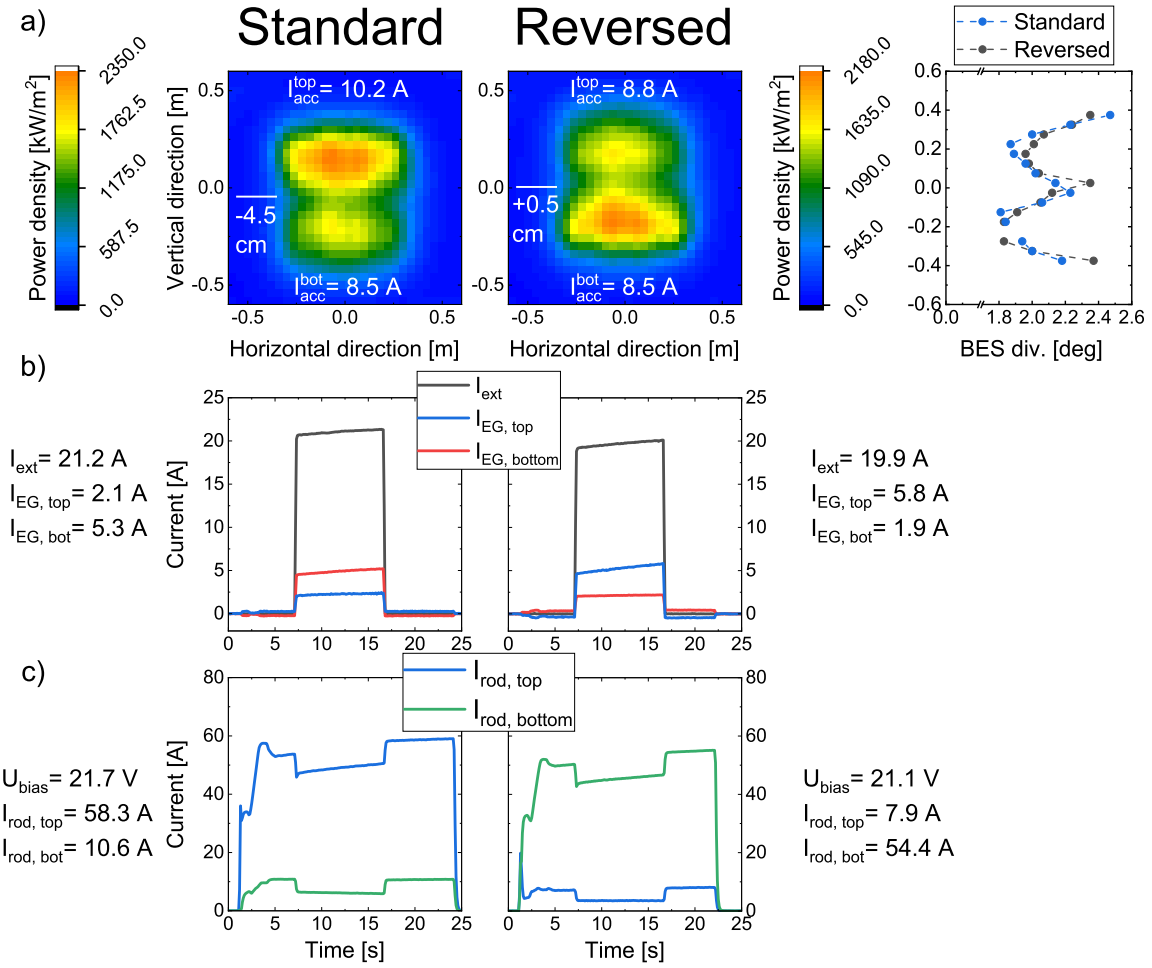

Figure 4.16: *a)* 2D map of the beam power density in the standard configuration (left), in the reversed configuration (center) and divergence profiles (right). *b)* Extracted negative ion current (black), and co-extracted electron current measured on the EG segments (top in blue and bottom in red). *c)* Time-trace of the current collected on the rods (top in blue, bottom in green) for the two configurations. The values of the currents are reported side-wise the figure, for the rods value only the value measured during the RF phase are reported. H, $p_{\mathrm{fill}} = 0.3\,\mathrm{Pa}$, $P_{\mathrm{RF}} = 60\,\mathrm{kW/driver}$, $U_{\mathrm{ext}} = 8\,\mathrm{kV}$, $U_{\mathrm{acc}} = 40\,\mathrm{kV}$, $I_{\mathrm{bias}} = 35\,\mathrm{A}$ and $I_{\mathrm{PG}} = 1.6\,\mathrm{kA}$ + external strengthening magnets ($1.9\,\mathrm{mT}$).

These experimental observations, instead show that the source performance as well as the beam characteristics are the same but turned upside-down, thus leading to the

conclusion that the amount of Cs present is sufficient to have similar performances in the two configurations for short pulses. Concerning the alignment of the grid system, this investigation does not highlight the presence of any misalignment.

4.3.1 Vertical homogeneity of the plasma parameters

The plasma drifts affect the plasma properties along the vertical direction not only between beamlet groups but also within the beamlet groups, thus the plasma parameter profiles over the spatial domain of the movable Langmuir probe are studied in the two filter field configurations. The positive ion density n_+ and the plasma potential ϕ_{plasma} profiles are shown in figure 4.17: in this case the reversed top is plotted as standard bottom case to ease the comparison between the top and bottom plasma parameters. The measurements are performed during the RF phase. The positive ion density n_+ is lower in front of the bias plate than directly in front of the PG. On both sides of the ion source the positive ion density is higher of about 20% at the edge of the ion source, i.e. at $\pm$ 350 mm, than at the center of the beamlet groups, i.e. $\pm$ 200 mm. On the upper segment half, the positive ion density has a dip at about +350 mm. The positive ion density is almost symmetric on the two source sides, but no dip in present on the bottom side. The effect of the plasma drift is visible comparing the positive ion density above the bias plate: in the top n_+ is almost 50% higher than on the bottom side.

The plasma potential shows an increase above the PG due to the PG biasing on both sides of the source. On the upper side of the source (between +350 mm and +200 mm) the plasma potential gradually increases and reaches the maximum at +200 mm, instead at the bottom ion source side the plasma potential profile is flat over the extraction area.

By comparing the plasma potential with the PG potential in figure 4.17 it can be seen that the PG sheath is strongly electron attracting in the upper part of the extraction system. This is a possible explanation for the high current measured on the top rod segment: with such an electron attracting sheath the electrons are collected preferentially at potential rods and PG. In the bottom half, the plasma potential is close to the PG potential thus electrons are less efficiently collected on the potential rods and on the PG compared to the top ion source side. To verify that the asymmetry the rod current is mainly caused by the plasma potential asymmetry, the vertical profile of $I(\phi_{\text{plasma}})$ is shown in figure 4.18. The quantity $I(\phi_{\text{plasma}})$ shows an initial increase between +400 mm and +380 mm, i.e. corresponding to the edge of the bias plate. Above the PG, the electron density shows a dip at about +350 mm similarly

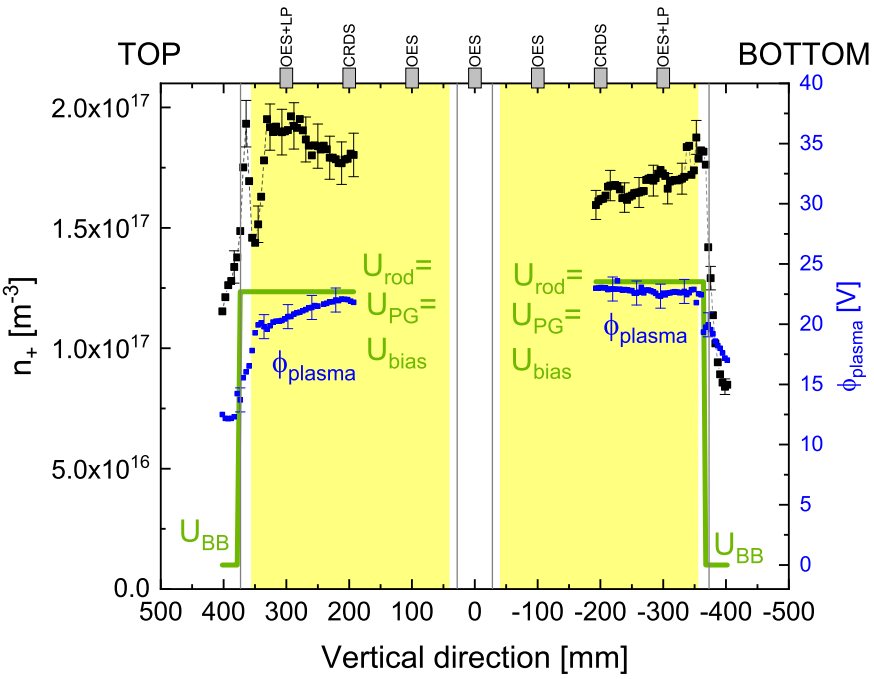

Figure 4.17: Positive ion density profile (black points) and plasma potential profile (blue points) obtained from the movable RF compensated LP. The measurements of the top half are performed in the standard configuration whereas the one of the bottom in the reversed configuration. Only the RF phase is shown. The green line shows the wall potential: 0 V above the bias plate and U_{bias} above the PG. The gray vertical lines depict the edges of the bias plate and the yellow shaded area shows the extraction area. Parameters: H, $p_{\mathrm{fill}} = 0.3\,\mathrm{Pa}$, $P_{\mathrm{RF}} = 60\,\mathrm{kW/driver}$, $U_{\mathrm{ext}} = 8\,\mathrm{kV}$, $U_{\mathrm{acc}} = 40\,\mathrm{kV}$, $I_{\mathrm{bias}} = 35\,\mathrm{A}$ and $I_{\mathrm{PG}} = 1.6\,\mathrm{kA}$ + external strengthening magnets (1.9 mT).

as for the positive ion density in figure 4.17. From the upper edge to the center of the beamlet group, the electron density decreases and it reaches a minimum at about +200 mm. On the bottom side of the ion source, the profile is monotonously decreasing from the center of the beamlet group to the lowermost edge of the ion source.

A possible reason for the dip in the positive ion density profile and on the $I(\phi_{\mathrm{plasma}})$ profile, see figures 4.17 and 4.18, can be related to the change of wall potential at the edge of the bias plate. The same is not observed at the same position at the bottom of the ion source, though. This effect seems to be related to the change of wall potential and to relatively high electron density: the phenomenon is still under investigation.

The plasma potential asymmetry causes an asymmetry in the electrons collected on the potential rods, thus the main reason behind the current asymmetry in the rod is due to the plasma potential asymmetry. Similarly as for the potential rods, where the sheath is strongly electron attracting, electrons are collected at the PG.

In the standard configuration of the filter field the vertical plasma drifts push the

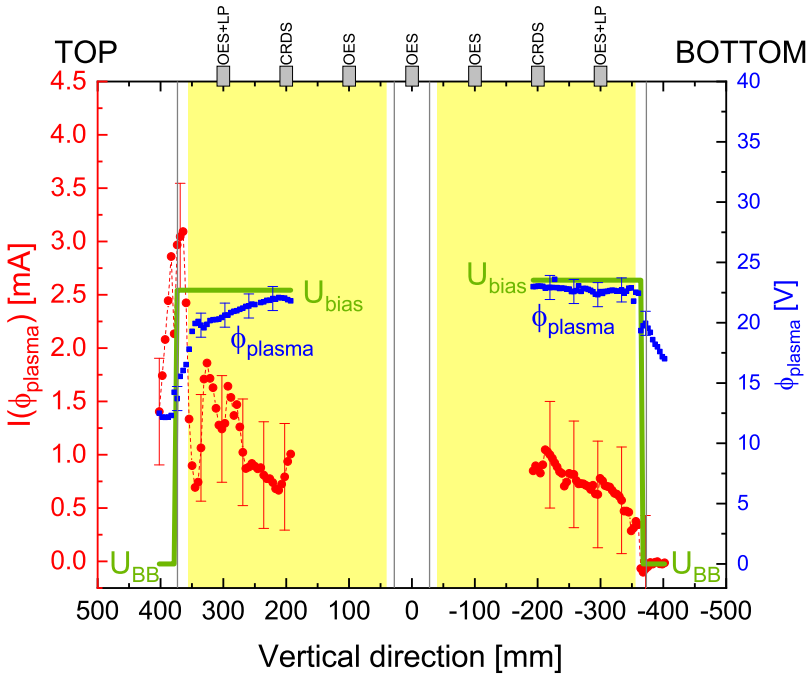

Figure 4.18: Profile of the current at the plasma potential $I(\phi_{\text{plasma}})$ (red points) and plasma potential profile (blue points) obtained from the movable RF compensated LP. The measurements of the top half are performed in the standard configuration and the one of the bottom side in the reversed configuration. Only the RF phase is shown. The green line shows the wall potential: 0 V above the bias plate and U_{bias} above the PG and at the rods. The gray vertical lines depict the edges of the bias plate and the yellow shaded area shows the extraction area. Same parameters of figure 4.17

plasma upwards, resulting in a lower electron density at the bottom of the ion source and a higher density in the top. Within the vertical extension of the ion source the parameters show a vertical gradient in the value density whereas positive ions are roughly flat in the measurement domain. Local quasi-neutrality is then given by the surface-produced negative ions.

4.3.2 Correlation with the co-extracted electrons

Two I-V curves measured in the standard and reversed configuration are shown in figure 4.19 for the RF phase and for the HV phase. In the upper part of the figure, the measurement is performed with the standard configuration at +200 mm position, i.e. at the center of the beamlet group. In the lower part of the figure the I-V curves measured with the reversed field at the same position are shown. The co-extracted electron current on the two EG segments is shown as well.

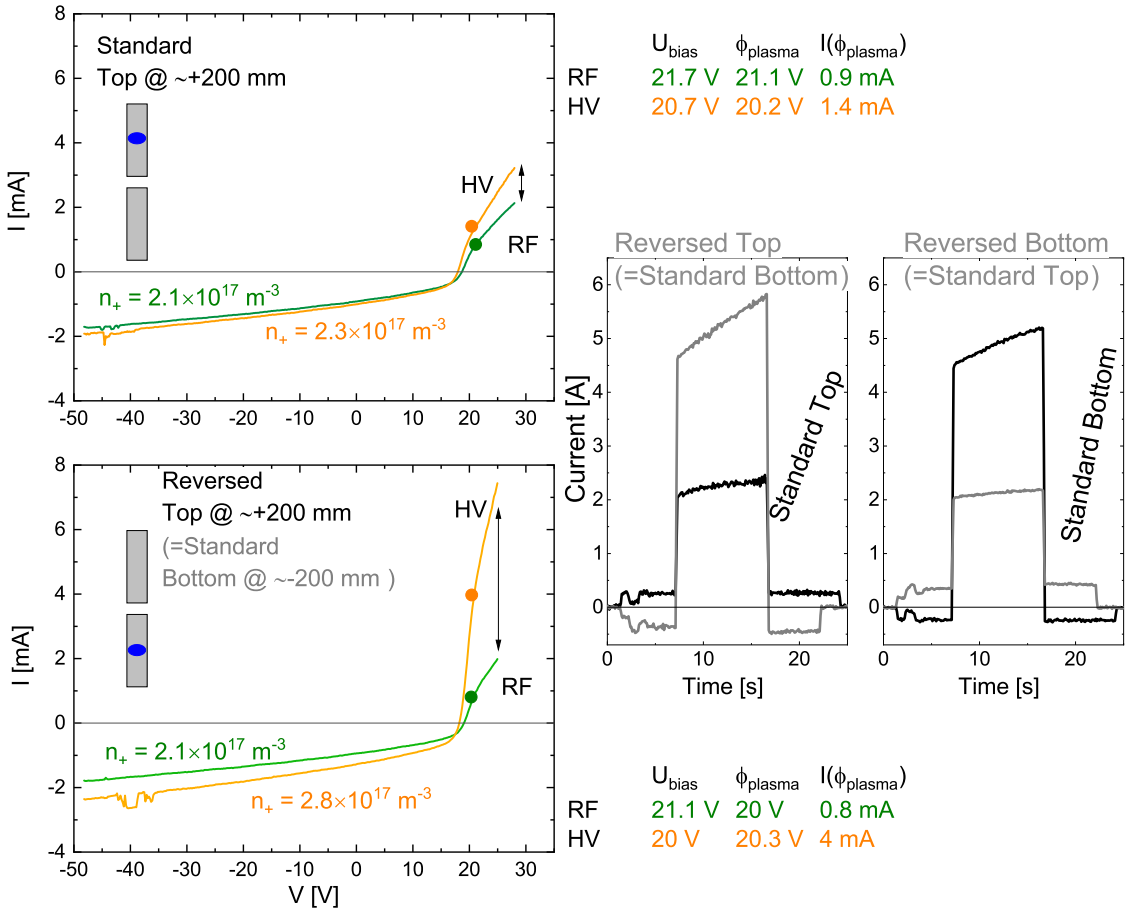

Figure 4.19: I-V curves obtained with the movable LP in the standard configuration (top) and in the reversed configuration (bottom). On the right, the time-traces of the co-extracted electron current on the EG segments in the standard configuration (black) and reversed one (gray) are shown. The values of ϕ_{plasma}, U_{bias}, $I(\phi_{\text{plasma}})$ and n_+ are reported for every case. Same operational parameters of figure 4.16

The I-V curves in the two configurations are similar during the RF phase, but a strong increase of the $I(\phi_{\text{plasma}})$ is measured during the HV phase in the reversed bottom. Under the assumption that $I(\phi_{\text{plasma}})$ is mainly determined by the electron flux on the LP, the increase of $I(\phi_{\text{plasma}})$ during the extraction phase is caused by an increase of electron density in the plasma. As demonstrated in section 4.2.2, the electron density measured during the HV phase is correlated with the co-extracted electron current: in this case the co-extracted electrons in the standard top are lower with respect of the reversed top (=standard bottom) which correlates with a higher value of $I(\phi_{\text{plasma}})$ in the corresponding configuration. The difference $U_{\text{bias}} - \phi_{\text{plasma}}$ is about $+1$ V, namely an electron attracting sheath at the PG, during the RF phase. When the HV is applied, the difference $U_{\text{bias}} - \phi_{\text{plasma}}$ is <1 V, thus PG and plasma are at the same potential, within the error bars. Thus, modifying the charged particle

fluxes at the PG. For what concerns the positive ion density, during the RF phase the values are the same within the error bars for top and bottom, thus confirming that the positive ion density is almost top-bottom symmetric as already shown with the symmetry of the bias plate current. During the HV phase, the positive ion density increases and the increase is slightly more pronounced at the bottom of the ion source (reversed configuration). The plasma drifts strongly affects the flux of electrons from the driver region into the PG, but the surface-produced negative ions generated at the PG are the major negatively charged species, thus reducing the electron density and, consequently, the electron flux towards the PG.

In order to study the symmetry of the electron density and of the co-extracted electron current, the relationship between current at the plasma potential and co-extracted electron current is investigated in more details and the results for the upper and lower half of the ion source are compared. Identical parameter variations have been performed for the standard filter field configuration and the reversed configuration: the comparison between co-extracted electron current $I_{\mathrm{EG,top}}$ and quantity $I(\phi_{\mathrm{plasma}})^{\mathrm{HV}}$ is shown in figure 4.20 for a magnetic field strength variation, i.e. I_{PG}, in *a)* and an I_{bias} variation in *b)*. For both parameter variations, the co-extracted electron current measured on the upper EG segment, i.e. where the probe is located, is roughly proportional to $I(\phi_{\mathrm{plasma}})^{\mathrm{HV}}$, which is mainly determined by the electron density in the plasma during the extraction phase. As shown in figure 4.20*a)*, the electron density in the plasma during the HV phase decreases with increasing the magnetic field strength. The decrease of $I(\phi_{\mathrm{plasma}})^{\mathrm{HV}}$ affects both sides of the ion source, but for the same magnetic field strength, the electron density is higher at the bottom of the ion source than at the top. The slopes are different for the two ion source halves, which is not significant since the co-extracted electron current is integrated over one grid segment whereas $I(\phi_{\mathrm{plasma}})^{\mathrm{HV}}$ is given for a localized portion of the palsma at the center of the beamlet group.

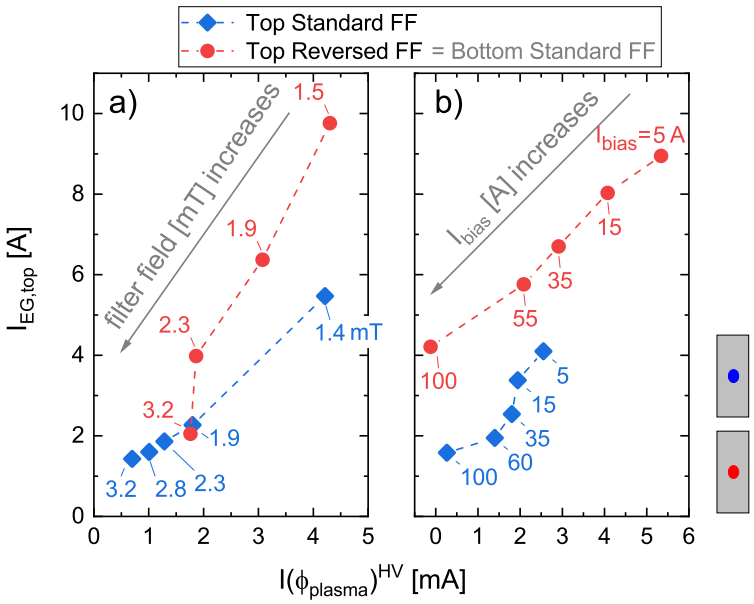

Figure 4.20: Co-extracted electron current $I_{\mathrm{EG,top}}$ as a function of $I(\phi_{\mathrm{plasma}})^{\mathrm{HV}}$ for a I_{PG} variation in *a)* and for a I_{bias} variation in *b)*. In blue points the measurements performed in the standard filter field configuration and in red the measurements performed with the reversed FF, equivalent to the standard bottom case. Value of the movable probe positioned at ≈+190 mm, i.e. center of the beamlet group. The scan was performed in H at $p_{\mathrm{fill}} = 0.3$ Pa, P_{RF}=60 kW/driver, $U_{\mathrm{ext}} = 8$ kV, $U_{\mathrm{acc}} = 40$ kV. In *a)* $I_{\mathrm{bias}} = 35$ A and in *b)*$I_{\mathrm{PG}} = 1.6$ kA + external strengthening magnets (1.9 mT).

For a variation of I_{bias}, $I(\phi_{\mathrm{plasma}})^{\mathrm{HV}}$ decreases, which is then correlated to a reduction of co-extracted electrons. For the same value of I_{bias} the electron density is higher in the bottom than in the top for all the cases except for $I_{\mathrm{bias}} = 100\,A$. Thus, a strong PG biasing reduces the electron density. For the same value of $I(\phi_{\mathrm{plasma}})^{\mathrm{HV}}$, the co-extracted electron current is almost the double in the bottom than in the top. The electron density is the plasma is significantly reduced when a strong filter field strength and a strong PG biasing are applied. Typically, for the same value of filter field or PG biasing the electron density measured at the top is lower than at the bottom. Nevertheless, the electron flux towards the PG is determined also by the PG sheath, i.e. $U_{\mathrm{bias}} - \phi_{\mathrm{plasma}}$, at the plasma grid.

In figure 4.21 the sheath $U_{\mathrm{bias}} - \phi_{\mathrm{plasma}}$ at the biased surfaces, i.e. PG and potential rods, is shown for the I_{bias} variation of figure 4.20*b)*. The values are shown for two positions: at the center of the beamlet group in *a)* and at the uppermost position above the PG in *b)*.

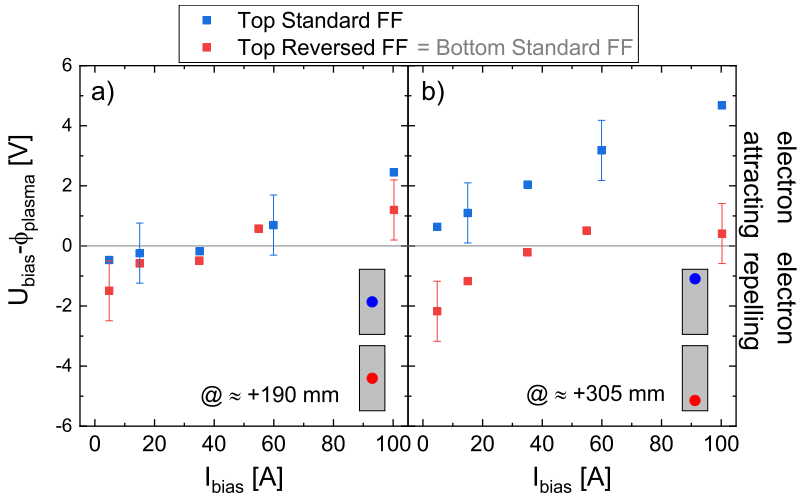

Figure 4.21: Sheath at the PG or rods $U_{\text{bias}} - \phi_{\text{plasma}}$ as a function of the I_{bias} current. Measurement performed at a different position: +190 mm (center of the beamlet group) in *a)* and at +305 mm (upper part of the beamlet group) in *b)*. Plotted in blue are the measurements performed in the standard FF configuration and in red the measurements performed with the reversed FF, equivalent to the standard bottom case. Measurement performed during the HV phase. The variation was performed in H at $p_{\text{fill}} = 0.3$ Pa, P_{RF}=60 kW/driver, $U_{\text{ext}} = 8$ kV, $U_{\text{acc}} = 40$ kV, $I_{\text{PG}} = 1.6$ kA + external strengthening magnets (1.9 mT).

At the center of the beamlet group (figure 4.21 *a)*) and for all investigated values of I_{bias} the sheath is identical, within the error bars, for top and bottom of the ion source. Instead, for the uppermost and the lowermost position of the ion source, i.e. at ± 305 mm, the trend is different: at the top, the PG and rod potential U_{bias} is always higher than the plasma potential ϕ_{plasma}, up to about 5 V higher for $I_{\text{bias}} = 100$ A, thus the PG sheath is electron attracting. In the bottom part of the ion source, the sheath at the PG and at the potential rods is electron repelling and only at high I_{bias}, i.e. 60 A - 100 A, the plasma potential is comparable to U_{bias}, all electrons can reach the biased surfaces. The comparison performed at different position indicates that the plasma potential profile is characterized by a vertical gradient, not only between the beamlet groups, but also within the beamlet groups. Moreover, the vertical asymmetry of the plasma potential at the uppermost and lowermost positions is enhanced at high value of PG biasing. Though, the co-extracted electron is reduced, since the sheath at the PG is electron attracting for all the investigated position except the lowermost one.

Increasing the RF power is a fundamental step to increase the extracted negative ion current, thus to fulfill the ITER requirement. With an RF power variation, it is possible to investigate the effect of the variation of the electron density, which increases with the RF power in the driver region (see figure 4.2) and consequently in the vicinity of the PG. Also the atomic density increases as well thus, if the work function is kept

constant, a higher atomic flux to the surface results in a higher emission of negative ions from the PG. In figure 4.22 the comparison between top and bottom of the ion source is performed for an RF power variation. $I(\phi_{\mathrm{plasma}})$ is shown in *a)*, $I(\phi_{\mathrm{plasma}})^{\mathrm{HV}}$ is shown in *b)* as well as the co-extracted electron current and the sheath $U_{\mathrm{bias}} - \phi_{\mathrm{plasma}}$ is shown in *c)* as a function of the RF power applied per driver. $I(\phi_{\mathrm{plasma}})$ slightly increases with RF power both at the top and at the bottom of the ion source. The values measured during the HV phase are higher than the corresponding values of the RF phase and the increase with respect to the RF phase is much more pronounced at the bottom of the source. The value of $I(\phi_{\mathrm{plasma}})^{\mathrm{HV}}$, mainly given by the electron density in the plasma, is roughly constant at the top whereas it increases at the bottom of the ion source. On the other hand, the co-extracted electron current linearly increases on both sides of the ion source, but with a different slope in the two cases. The sheath at the biased surfaces show a different behavior on the two ion source halves: at the top the sheath does not vary with RF power, namely the PG is always electron attracting, whereas at the bottom, the sheath is electron attracting for low RF power, i.e. 45 kW/driver, and electron repelling at 70 kW/driver.

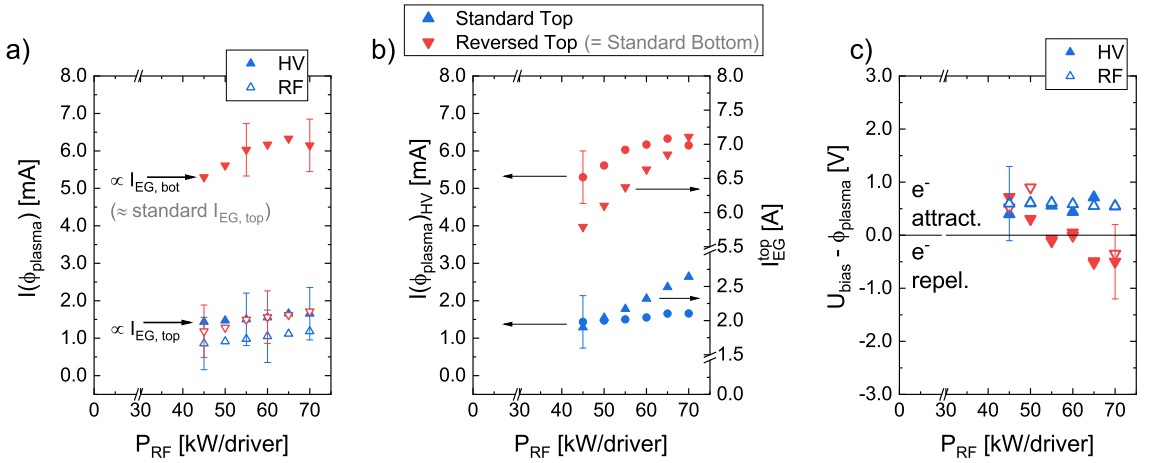

Figure 4.22: $I(\phi_{\mathrm{plasma}})$ in *a)*, $I(\phi_{\mathrm{plasma}})^{\mathrm{HV}}$ and co-extracted electron current in *b)* and sheath $U_{\mathrm{bias}} - \phi_{\mathrm{plasma}}$ in *c)* are plotted as a function of the RF power. The measurements are performed in the center of the beamlet group (at +190 mm) for the standard FF in blue and for the reversed FF (equivalent to the standard bottom) in red. The empty symbols refer to the RF phase and the full one to the HV phase. Parameters: H, $p_{\mathrm{fill}} = 0.3\,\mathrm{Pa}$, $I_{\mathrm{bias}} = 35\,\mathrm{A}$, $I_{\mathrm{PG}} = 1.6\,\mathrm{kA}$ + external strengthening magnets (1.9 mT), $U_{\mathrm{ext}} = 8\,\mathrm{kV}$, $U_{\mathrm{acc}} = 40\,\mathrm{kV}$.

At the top of the ion source the sheath is constant within the error bar, thus the flux balance at the PG is stable, namely an increase of electron flux due to a higher RF power is compensated by a higher emission of negative ions from the PG surface.

At the bottom, since the sheath at the PG is varying, the flux balance at the PG is varying, namely a higher electron flux is not compensated by a higher emission of negative ions from the PG into the plasma. A possible explanation for this difference between top and bottom of the ion source is a depletion of Cs at the bottom which causes a degradation of the PG work function.
The different sheath between top and bottom of the ion source influences the current collected at the rods: in figure 4.23 the current measured at the rods during the RF phase[13] is shown as a function of the RF power variation under discussion. The current on both rod segments increases with RF power, but with a different slope on the two segments.

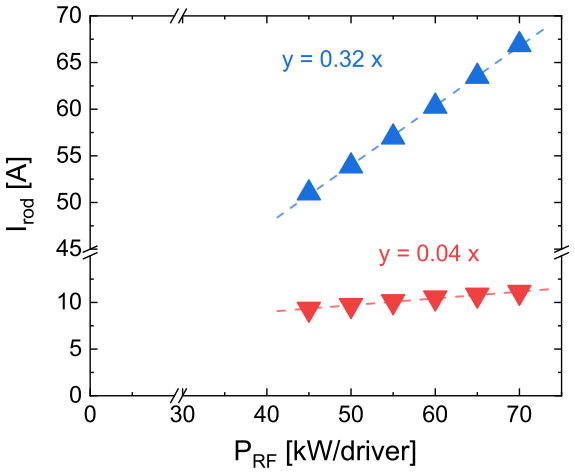

Figure 4.23: Rod current measured during the RF phase as a function of the RF power. Same RF power variation shown in figure 4.22.

4.4 Conclusions

The plasma in the driver region is characterized by an electron temperature T_e of approximately 10-13 eV and by an electron density n_e in the order of $10^{18}\mathrm{m}^{-3}$. In the driver region at these plasma parameters, dissociation of molecular hydrogen into atoms takes place. The intensity of the Balmer lines H_α, H_β and H_γ is mainly related to atomic ionization whereas the intensity of the Fulcher-α molecular band is related to molecular ionization. The electron density in the driver and, in turn, the dissociation degree are affected by variations of the RF power and of the magnetic filter field strength.
The plasma emission from the four drivers is identical, within the error bars, thus it

[13]The same reasoning holds also for the HV phase (not shown), but for simplicity only one phase is shown.

is possible to conclude that the plasma parameters are the same for the four drivers and that the flux of particles from the driver region is the same for all drivers. The magnetic field, necessary to reduce the electron temperature and density close to the extraction region gives rise to vertical plasma drifts that affect the vertical homogeneity of the plasma potential and of the charged species densities. When the magnetic field is stronger than about 1 mT at 2 cm from the PG, negative ion destruction mechanism via electron impact with energetic electrons is reduced. The emission of negative ions from the PG surface decreases even more the electron density close to the extraction region. If the magnetic field is too strong, the transport of positive ions from the drivers is reduced, thus reducing the positive ion density at the PG which can limit the emission of negative ions from the PG due to space charge limit. The presence of the potential rods at the PG potential modifies the net flux of charged particles at the PG: if the sheath at the rods is not electron repelling, electrons are preferentially collected at the rods, thus the emission of negative ions from the PG becomes a relevant contribution to the current measured on the PG. The positive ion flux averaged over the ion source halves is the same within 10% with the potential rods installed whereas for similar operational parameters without potential rods the top segment is about 60% higher than the bottom one. The current measured on upper potential rods is typically three to four time higher than the current measured on the lower potential rods. This asymmetry can be caused either by a local asymmetry of the electron density between top and bottom and/or by an asymmetry of the plasma potential.

The co-extracted electrons are correlated to the charged particle fluxes towards the PG apertures, namely to the density and to the particle velocity, which is in turn influenced by the sheath at the PG. The value of the co-extracted electron current, which is averaged over one half of the EG grid, is proportional to the electron flux integrated over the extraction apertures, thus an univocal relationship between localized plasma measurements and co-extracted electron current is not possible due to the different measurement domain. The amount of co-extracted electrons is proportional to the electron density in the plasma during the HV phase. The electron density in the plasma and, consequently, the co-extracted electron decreases when the plasma sheath at the PG is electron attracting.

A dedicated experimental campaign was performed with reversed polarity of magnetic filter field, thus with reversed plasma drifts. The plasma and beam properties immediately reacted on the change of filter field and the result is a substantial inversion (upside-down) of the beam symmetry and of the plasma properties, thus suggesting

that the amount of Cs present over the PG surface is sufficient in short pulses to have the same source performances, since no long-term Cs redistribution was needed.
Measurements with the movable RF-compensated Langmuir probe demonstrated a symmetry of the positive ion density between top and bottom of the ion source. The vertical profile of the electron density shows, on the other hand, a gradient over the vertical dimension of the surface, i.e. an higher electron density on the uppermost side of the source is observed compared to the lowermost side. The plasma potential profile shows that, on the upper half of the upper beamlet group, the PG sheath is strongly electron attracting whereas at the center of the upper beamlet group and on the bottom segment the plasma potential is, within the error bars, the same as PG potential. Comparing the centers of the top and bottom beamlet groups, minor differences in terms of plasma potential are observed, whereas at the uppermost and lowermost position of the ion source the plasma potential can be up to 4 V apart. Since the electron density in the plasma is similar between top and bottom of the ion source, the asymmetry of the plasma potential plays the major role in the asymmetry of the current measured on the potential rods.
In general and for the same operational parameters, the electron density in the plasma is higher at the bottom of the ion source than at the top and it decreases with increasing magnetic field strength and increasing the PG biasing, thus with a PG sheath that is electron attracting. As a consequence, the co-extracted electron current is reduced as well.

5 Beam characterization

The beam produced at the ELISE test facility originates from extraction and acceleration of negative ions from the source plasma. Beam diagnostics are fundamental tools to study the beam properties as a function of the operational parameters. The diagnostic setup is described in section 3.2.2 and it consists of BES diagnostics and IR calorimetry on the diagnostic calorimeter. The beam is described in terms of LOS-averaged beam divergence, i.e. averaging the beamlet divergence over different rows of beamlets, and in terms of power density at the level of the beam segments, thus with no insight on the single beamlet power density profile. The eligibility of the fitting routine used on the 2D power density profile is tested in section 5.1 as well as the crosscheck of IR calorimetry with BES results. The beam divergence shows a systematic difference in diverge between top and bottom beam segments. This asymmetry is studied in section 5.2 through a definition of local perveance defined at the level of the beam segment by using the localized information obtained by IR calorimetry. In section 5.3 the beam divergence optimization through the focusing of the electrostatic lens, namely the optimization of the acceleration voltage U_{acc} applied between EG and GG, is studied. An analysis of the current collected on the different beamline components is carried out in section 5.4.

5.1 IR calorimetry

The fitting routine discussed in section 3.2.2 is routinely used to evaluate the beam properties. The fitting function is tested to check the eligibility of the fit to represent a multi-beamlet beam measured at large distance from the grounded grid, synthetic 2D power density profiles are simulated and the limits of the applicability of the fit are studied.

5.1.1 Eligibility of the fitting routine

Synthetic profiles of the beam power density are simulated by assuming a Gaussian power distribution for each of the 640 beamlets at the exit of the grounded grid and projecting the beamlet onto the calorimeter. No beamlet deflection is taken into account. The width δ if the Gaussian beamlet profile is calculated as

$$\delta = \frac{1}{\sqrt{2}}\, d\, \tan\left(\vartheta_{1/e} \cdot \frac{\pi}{180}\right), \tag{5.1}$$

where $\vartheta_{1/e}$ is the divergence in degrees at one e-folding half width and $d = 3.5\,\mathrm{m}$ is the distance between grounded grid and diagnostic calorimeter. The factor $\frac{1}{\sqrt{2}}$ allows the conversion factor from the width in sigma (standard deviation of the distribution) to the e-folding half width. For every aperture i a Gaussian function $p_i(x, y)$ is used. The total power on the calorimeter $p(x, y)$ is

$$p(x,y) = \sum_{i=1}^{640} p_i(x,y) = \sum_{i=1}^{640} \frac{a_i}{2\pi\delta_x\delta_y} e^{\frac{-(x_i-x)^2}{2\delta_x^2} - \frac{(y_i-y)^2}{2\delta_y^2}}, \tag{5.2}$$

where a_i is the peak amplitude of the single Gaussian function describing the beamlet, x_i and y_i are the horizontal and vertical beamlet coordinates defined in the reference system of figure 3.12(a), and δ_x and δ_y are the horizontal and vertical beamlet widths. The following assumptions are taken:

- All the beamlets are circular ($\delta_x = \delta_y$);
- The peak intensity a_i is the same for beamlets belonging to the same beamlet group;
- Since the beamlet intensity is identical, single beamlet perveance is identical for beamlets in the same beamlet group. Thus, the beamlet divergence is assumed to be uniform inside a beamlet group;

Fluctuations are simulated by adding a random noise of $\pm 10\%$ on the resulting value of power density. The resolution of the synthetic profile is adapted to the experimental resolution of the blocks of the calorimeter.
By fitting the synthetic profiles, it is possible to correlate the behavior of the output parameters, i.e. beamlet group vertical and horizontal width, amplitude and vertical position, with the ones used as input for the simulation, such as the dependence between beamlet divergence ϑ and beamlet group widths σ_x and σ_y as shown in figure 5.1(a): σ_x and σ_y for the top and bottom beam segments obtained from the fitting

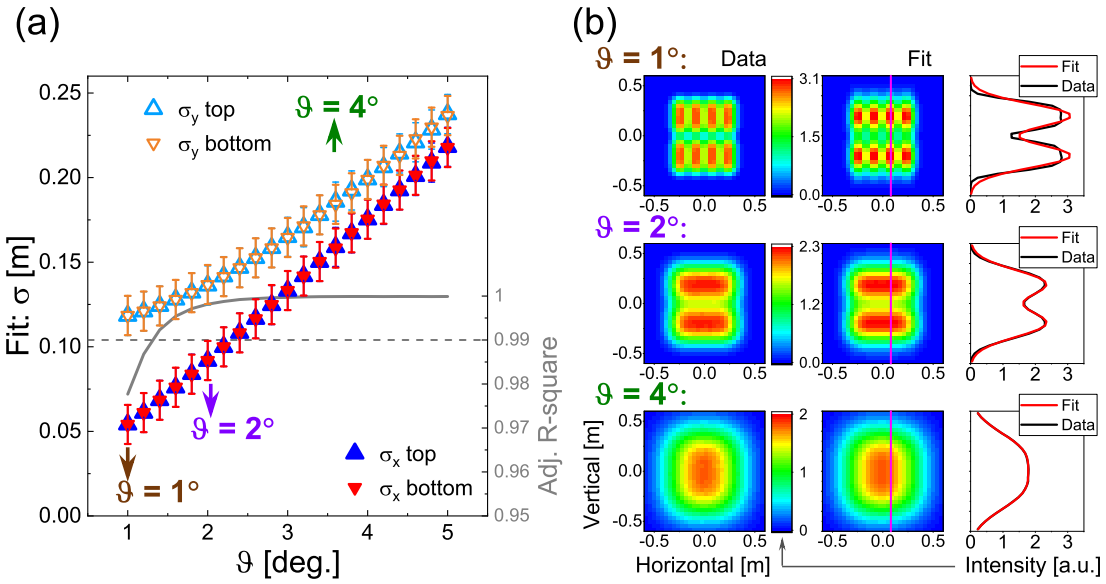

Figure 5.1: *a)* Vertical and horizontal beamlet group widths for the top and bottom segments calculated by the fitting routine as a function of the divergence used in the synthetic 2D map; the intensity and divergence are the same for all the beamlets. For the cases with 1, 2 and 4 degree divergence a plot of the synthetic data, of the fitted matrix and of the vertical profile is shown in panel *b)*. In *a)* the adjusted R-square calculated is shown on the right axis: the level of 0.99 indicates the minimum level accepted. Below 0.99 the simulated map is not properly reproduced by the fitting routine.

routine are plotted as a function of ϑ. In each simulation shown in figure 5.1(a), the intensity and the divergence are the same for all beamlets, thus the beam is horizontally and vertically symmetric with respect to the zero of the scale. The divergence varies from $\vartheta = 1$ degree to $\vartheta = 5$ degrees in steps of 0.2 degrees. While increasing the beamlet divergence, the width of the beamlet groups in the power density profile increases. The behavior of σ_y is linear for divergences higher than 2.5 degrees, whereas at lower divergences σ_y saturates around 0.12 m. The saturation is determined by the geometrical arrangement and size of the apertures. Only for small values of divergence the beam vertical width is determined by the geometrical arrangement of the apertures. The horizontal width σ_x always increases almost linearly with increasing divergence and does not show any saturation. In figure 5.1*a)* the adjusted R-square of the fit as a function of ϑ is shown on the right axis . The adjusted R-squared is an estimator of the goodness of the fit, and the threshold used to accept the result is 0.99.

In figure 5.1(b), the 2D maps and profiles from simulations with 1, 2 and 4 degrees divergence and the corresponding fits are shown: the synthetic 2D maps is shown in the first column, the fitted one is shown in the second column and in the third column

the vertical profiles taken on the line depicted in pink from the synthetic map and from the fitted one are displayed.
The overlap of Gaussian beamlets at the calorimeter plane gives a beamlet group profile that is not, in general, a Gaussian, especially for low divergences as shown in the figure 5.1(b) for the case at 1 degree: in this case, the beamlet group profile becomes flat in the central part, resulting in a rectangle rather than a bell-shaped curve. At 1 degree divergence the fitting procedure does not properly reproduce the synthetic map: the intensity (i.e. A_i in equation 3.14) is overestimated and the beam vertical width σ_y is underestimated. A different type of fitting function cannot be applied for the cases with divergence lower than 1.5 degrees, since the number of points would not be sufficient for a robust and reliable automatic evaluation of the IR 2D profile. Additionally, since the typical divergence measured by BES at ELISE is higher than 1.5 degrees (the minimal divergence observed at ELISE up to now at 0.3 Pa is 1.8 degree). The agreement between simulated profile and fitted one is good at divergence higher than 1.5 degrees, e.g. as shown for 2 and 4 degrees divergence in figure 5.1(b). At 4 degrees, where the beam segments cannot be distinguished because of the large overlap, the fitting routine reproduces the power profile correctly.
Up to this point, the test was performed on a homogeneous beam, i.e. all the beamlets have the same divergence and intensity. In reference [73] the fitting routine is tested on a larger set of simulations, where asymmetries of the beamlet divergence and beamlet intensity between beam segments, but also among beamlet groups, are introduced. The main results are reported in the following:

- The fit is capable to characterize the two beam segments independently from each other also in case of a large difference (3×) in intensity between the top and bottom beam segments. The fit recognizes successfully the beam segments also in case of a large difference in divergence between top and bottom.

- The fit outputs allow for a correct evaluation of the beam integral which is fundamental for the correct evaluation of the accelerated current carried by each beamlet group or beam segment.

- The fit correctly identifies the vertical position of the beam segments even in cases at high degree divergence. From the beam segment vertical position, the center of the beam can be deduced.

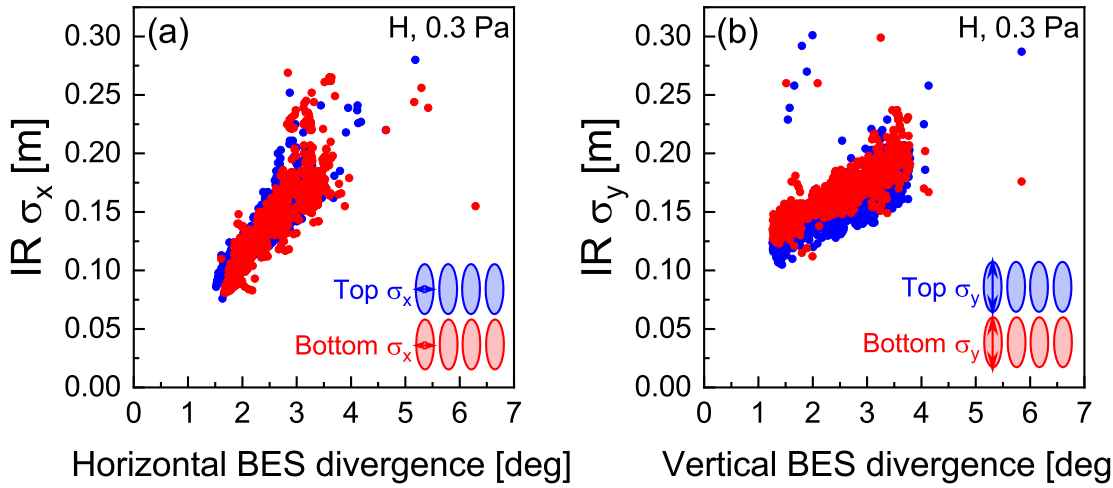

Figure 5.2: Comparison between IR calorimetry and BES. In (a) the horizontal width σ_x is plotted as a function of the BES horizontal divergence. In (b) the vertical width σ_y is plotted as a function of the BES vertical divergence. About 4000 pulses performed in hydrogen at 0.3 Pa between January 2017 and July 2018.

5.1.2 Crosscheck with BES diagnostics

Around 4000 hydrogen beam pulses performed at 0.3 Pa are used to crosscheck the IR calorimetry technique with the BES diagnostics regarding the correlation between the LOS averaged beamlet divergence and the beamlet group width. The beamlet group width σ from IR calorimetry is shown in figure 5.2 as a function of the beam divergence measured with BES, for the horizontal direction in (a) and the vertical direction in (b). The horizontal divergence from BES is the average of the divergence measured by three LOS looking at the center of the top and bottom beam segments, whereas the vertical divergence is an average of the values obtained from the two central vertical LOS.

In both the horizontal and vertical directions, there is good overall correlation between the beamlet group width estimated by IR calorimetry and the beam divergence from BES, proving that the beam width is, to a large extent, determined by the beam divergence. Nevertheless, the data points are scattered in a range of about 5 cm or more for the same beam divergence. For the horizontal direction, this can be explained by a horizontal non-homogeneity in beamlet intensity (a_i of equation 5.2) between the beamlet groups in each beam segment, whereas a vertical non-homogeneity within the beamlet groups can explain the scatter in vertical direction. The bottom vertical width σ_y (red points in figure 5.2(b)) is systematically larger than the top one for the same BES divergence of about 2 cm. This difference is real, since it is larger than the error bars on the widths. A vertical asymmetry is also observed on the horizontal BES

divergence: lower divergences are observed in the top beam segment with respect to the bottom one. Hence, it can be stated that there is a different divergence between the beam segment, which can be caused by a different localized perveance for the two beam segment. On this point a detailed investigation is performed in the following sections.

5.2 Beam perveance

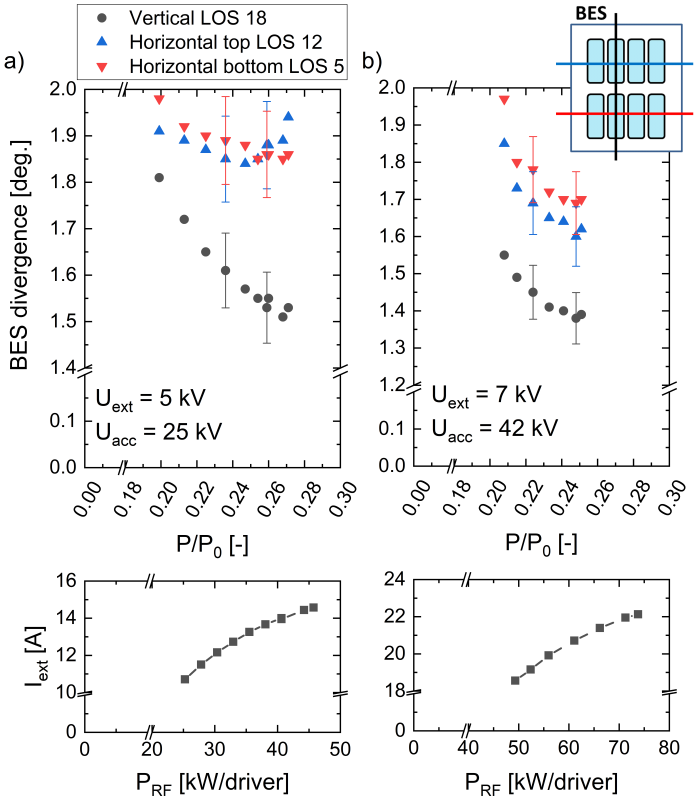

Figure 5.3: BES Divergence as a function of the normalized perveance P/P_0 for two different cases: in *a)* for U_{ext}=5 kV and in *b)* for U_{ext}=7 kV. The divergence is measured for one LOS located at the top of the beam (LOS 12, blue points), at the bottom of the beam (LOS 5, red points) and for one vertical (LOS 18, black points). For each case, the extracted current I_{ext} is shown as a function of the RF power P_{RF} at the bottom of the figure. H, I_{PG} =1.6 kA (1.5 mT), p_{fill} =0.3 Pa, I_{bias} =35 A.

The extracted current I_{ext} increases with increasing RF power P_{RF} and, consequently, the normalized perveance increases affecting the beam optics. In this section, when not specified otherwise, the value of normalized perveance is calculated considering the total extracted current density, thus neglecting possible non-uniformities of the beam between beam segments. In figure 5.3*a)* and *b)* the evolution of BES divergence

is shown for two RF power variations performed at U_{ext} =5 kV and 7 kV, respectively. The ratio $U_{\mathrm{acc}}/U_{\mathrm{ext}}$ is 5 for the case at U_{ext} =5 kV and 6 for the case at U_{ext} =7 kV, which is in both cases an optimal ratio for the electrostatic lens.
In both variations the vertical beam divergence decreases with increasing normalized perveance, demonstrating that the beam is in an under-perveant regime. The vertical LOS shown with black points, measures a lower divergence compared to the horizontal LOS, which are affected by the zig-zag effect caused by the deflection magnets (see section 2.5).
The lowest beam divergence is reached at a normalized perveance P/P_0 of about 0.27 for the case of U_{ext} = 5 kV and at 0.25 for the case at 7 kV. In both cases, the beam divergence of the vertical LOS does not reach a minimum: the perveance, which is determined by the extracted current I_{ext}, can in fact still increase, though with a lower rate since I_{ext} starts to saturate. In figure 5.3*a)* LOS 12, which is positioned approximately at the center of the top beam segment, shows a minimum at P/P_0 =0.25 and an increase of the divergence for higher values of P/P_0 which can only take place either if the localized perveance decreases and the localized divergence increases (under-perveant regime) or if the localized perveance increases and the localized divergence increases (over-perveant regime). The first can be excluded because it implies a decrease of extracted current for higher RF power, not observed experimentally..
The different evolution of the beam divergence for the two beam segments indicates that a single value of perveance for the entire beam is not appropriate to describe the beam segment. Qualitatively, the top beam segment is characterized by a higher value of localized perveance with respect to the bottom beam segment.
The effect of the different perveance in the two beam segments on the beam power density is studied by using the IR calorimetry results shown in figure 5.4. In panels *a)* and *c)* the left half of the 2D beam power density profile for three values of P_{RF} is shown for each scan. In panels *b)* and *d)* the vertical profiles along the center of the second beamlet group are shown. The 2D maps of the power density show an improvement of the peak intensity symmetry between top and bottom beam segments with increasing P_{RF} for both P_{RF} variations. The accelerated current symmetry calculated as $I_{\mathrm{acc}}^{\mathrm{top}}/I_{\mathrm{acc}}^{\mathrm{bot}}$[14] improves with RF power, being even turned, i.e. $I_{\mathrm{acc}}^{\mathrm{bot}} > I_{\mathrm{acc}}^{\mathrm{top}}$, for the highest value of P_{RF} in each scan. For the case at U_{ext}=5 kV the peak intensity of the top beam segment is roughly the same for P_{RF} =35 kW/driver and for

[14]The values of accelerated current I_{acc} for the beam segments are retrieved by applying the fitting to the 2D power density profiles.

P_{RF} =45 kW/driver whereas the highest peak intensity for the bottom beam segment in reached at P_{RF} =45 kW/driver. Thus, the top beam segment has reached the minimum of the perveance curve or even it is in an over-perveant regime, since the beam width is slightly higher, whereas the bottom beam segment is still under-perveant.

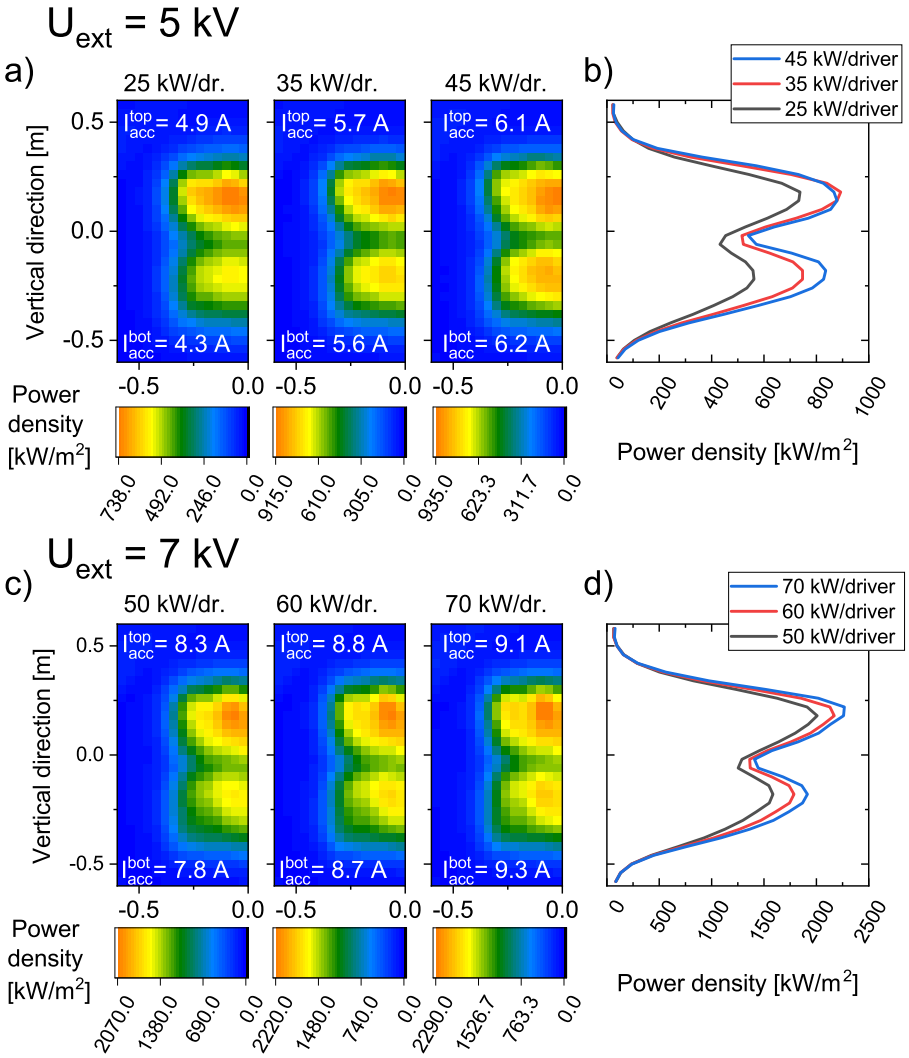

Figure 5.4: *a)* and *c)*: left half of the 2D beam power density map for three values of P_{RF}. *b)* and *d)*: vertical power density profile of the beam along the second beamlet group for three values of P_{RF}. *a)* and *b)* refer to the power scan done at U_{ext}=5 kV. *c)* and *d)* refer to the power scan performed at U_{ext}=7 kV. Same parameters of figure 5.3.

For the power variation performed at U_{ext}=7 kV the power density profiles are similar in shape for every RF power applied. At U_{ext}=7 kV, both beam segments are under-perveant. As for the case at U_{ext}=5 kV the peak intensity of both beam segments increases and the symmetry of the accelerated current improves with increasing RF power.

In general, at high RF power the accelerated current is almost top-bottom symmetric, i.e. $I_{\mathrm{acc}}^{\mathrm{top}} = I_{\mathrm{acc,bot}}^{\mathrm{bot}}$, but the different beam perveance for the two segments can give a different width and divergence, resulting in a different power density profile between top and bottom beam segment.

Varying the extraction potential affects the perveance by modifying both the extracted current I_{ext} and the extraction potential U_{ext}. To not modify the electrostatic lens, the ratio $U_{\mathrm{acc}}/U_{\mathrm{ext}}$ is kept constant to the value of 5. By increasing the extraction voltage, the global perveance decreases as shown in figure 5.5*a)*, where the extracted current I_{ext} and the normalized perveance are plotted as a function of U_{ext}. The extracted current increases almost linearly with the extraction potential, whereas the normalized perveance $P/P_0 \propto I_{\mathrm{ext}}/U_{\mathrm{ext}}^{3/2}$ decreases with increasing U_{ext}. In figure 5.5*b)* the beam divergence is plotted as a function of the global perveance P/P_0 for three different LOS, two horizontal at the center of the beam segments and one vertical. Both horizontal LOS show a minimum of divergence between 0.2 and 0.25 of normalized perveance, whereas the divergence measured by the vertical LOS steadily decreases and reaches a local minimum at about 0.28 normalized perveance. The vertical LOS indicates that the beam divergence is slightly improving with increasing global perveance, namely at low U_{ext}. The horizontal LOS give a value of divergence that is, within the error bars, constant. One possible reason for the different behavior between horizontal and vertical LOS can be the left-right beamlet deflection due to the deflection magnets, that influence the Doppler peak broadening (and hence the average divergence measured by BES) differently depending on U_{ext} and U_{acc} [89]. As a consequence, for this parameter variation, the beam properties will be studied only by means of IR calorimetry. The accelerated current and the power density profile evolve with U_{ext} as shown in figure 5.6, where the left half of the 2D beam power density profiles are plotted in *a)* and the power density profiles along the center of the second beamlet group normalized to the maximum[15] are plotted in *b)*. The peak intensity is almost top-bottom symmetric at U_{ext}= 5 kV and becomes less symmetric with increasing extraction voltage U_{ext}, until for U_{ext}= 8 kV the bottom peak intensity is 70% of the top one. Also the accelerated current is symmetric for low extraction voltages, whereas for U_{ext} higher than 7 kV $I_{\mathrm{acc}}^{\mathrm{top}}$ is higher than $I_{\mathrm{acc}}^{\mathrm{bot}}$, though with only 10% of difference.

The two beam segments are in a different perveance regime, since with decreasing the global perveance, the peak intensity of the top beam segment is almost constant, i.e.

[15]Since the extracted current increases, a normalization is applied to ease the comparison of the power density profiles.

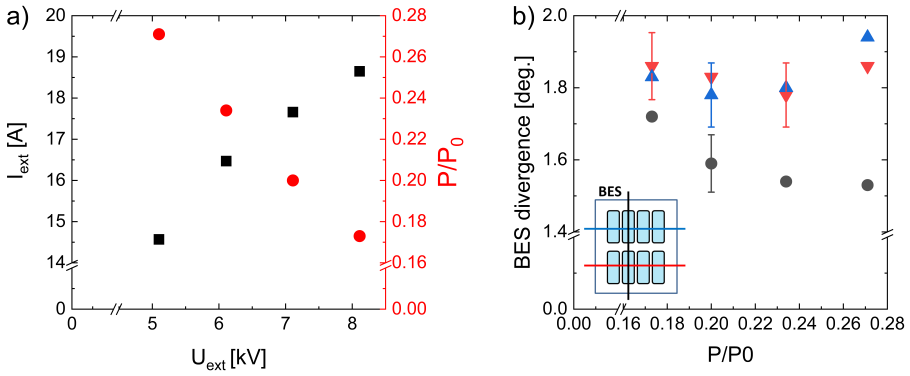

Figure 5.5: *a)* Extracted current density I_{ext} (black) and normalized perveance P/P_0 (red) as a function of the extraction voltage U_{ext}. *b)* BES divergence as a function of the extraction voltage U_{ext}. The divergence is measured for one LOS located at the top of the beam (LOS 13, blue points), at the bottom of the beam (LOS 5, red points) and for one vertical (LOS 18, black points). Parameters: H, Standard filter field, P_{RF}= 45 kW/driver, I_{PG} = 1.6 kA (1.5 mT), p_{fill} =0.3 Pa, I_{bias} =35 A, U_{acc}=5×U_{ext}

close to the optimum of the perveance curve, whereas for the bottom beam segment it is decreasing indicating an under-perveant regime. The difference in perveance is due to a lower extracted current for the bottom beam segment, which causes the observed lower accelerated current with respect to the top.

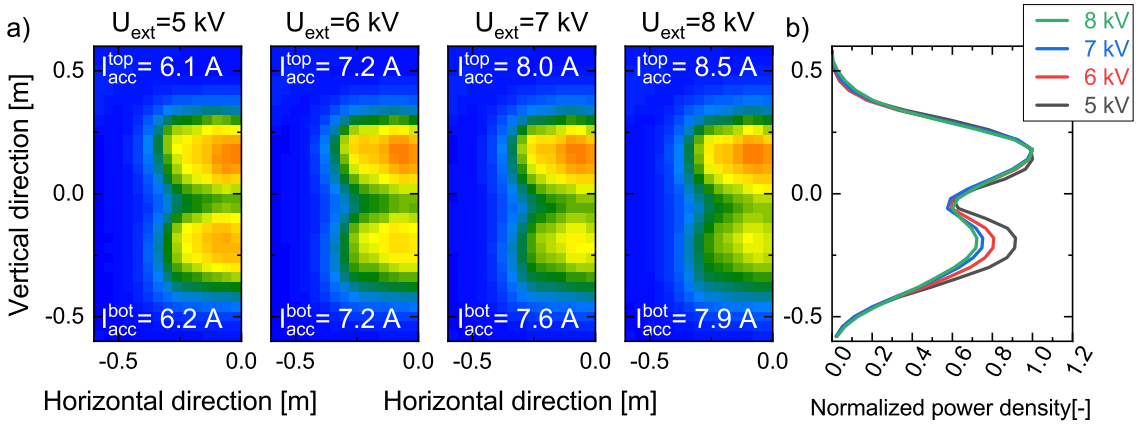

Figure 5.6: *a)* left half of the 2D beam power density profile for each value of extraction voltage. For every case the accelerated current is calculated for each beam segment. *b)* Power density profile along the center of the second beamlet group. The values are normalized to the maximum to ease the comparison among the different profiles. Same parameter variation shown in figure 5.5.

5.2.1 Localized Perveance

The top beam segment is characterized by a perveance higher than the one at the bottom beam segment. The difference in perveance between beam segments is given

by a lower extracted current for the bottom beam segment. With the information of the accelerated current at the level of the beam segment, it is possible to estimate the extracted current for each beam segment by assuming that the extracted current has the same ratio between top and bottom of the accelerated one. Thus, it would be possible the estimation of the local normalized perveance. Hence, the extracted current for the top beam segment is

$$I_{\text{ext}}^{\text{top}} = I_{\text{ext}} \cdot \frac{I_{\text{acc}}^{\text{top}}}{I_{\text{acc}}} \tag{5.3}$$

and similarly for the bottom beam segment. The extracted current for the top and bottom segments is used to calculate the beam segment perveance:

$$P_{\text{loc}}/P_{0,\text{loc}} = \left(\frac{I_{\text{ext,loc}}}{U_{\text{ext}}^{3/2}} \right) \frac{1}{P_0/2}, \tag{5.4}$$

where the factor 2 is present due to the reduced surface (half of the apertures) to be considered for the calculation of the local normalized perveance $P_{0,\text{loc}}$. In figure 5.7 the BES divergence is plotted as a function of the localized perveance and loc indicates either the top or the bottom segment. The variations shown in figure 5.7 are two RF power variations (the same of figure 5.3) performed at U_{ext}=5 kV in *a)* and at U_{ext}=7 kV in *b)*. Below each graph, the evolution of the accelerated current for the top and bottom beam segment is shown as a function of the RF power.
The use of the localized perveance shifts the horizontal axis and the perveance curves match better mainly for the low RF power cases, where the asymmetry of the accelerated current is more pronounced (see figure 5.3). For the case at U_{ext}=7 kV the local perveance curves are superimposed quite well when $P/P_0 \leq 0.22$, but they ùget apart for $P/P_0 > 0.22$. For the case at U_{ext}=5 kV, the agreement is good only when $P/P_0 < 0.22$, whereas for higher values of local perveance the two data sets get completely apart one from each other. For the case at U_{ext}=5 kV and for the upper BES LOS, a possible explanation for the mismatch is that the extracted current density is, within the beam segment, not uniform. Thus, in a beam segment the upper apertures are characterized by a higher local perveance,due to a higher extracted current.

The use of the localized perveance to match the perveance curves for the top and bottom beam segments indicates that the top-bottom asymmetry of the divergence is caused by a different extracted current in the two segments. Even if the agreement is improved, the curves still do not match especially at higher values of normalized perveance. Hence, vertically within the beam segments, a non uniform extracted current over the apertures seems to be still present, however the diagnostic access to a

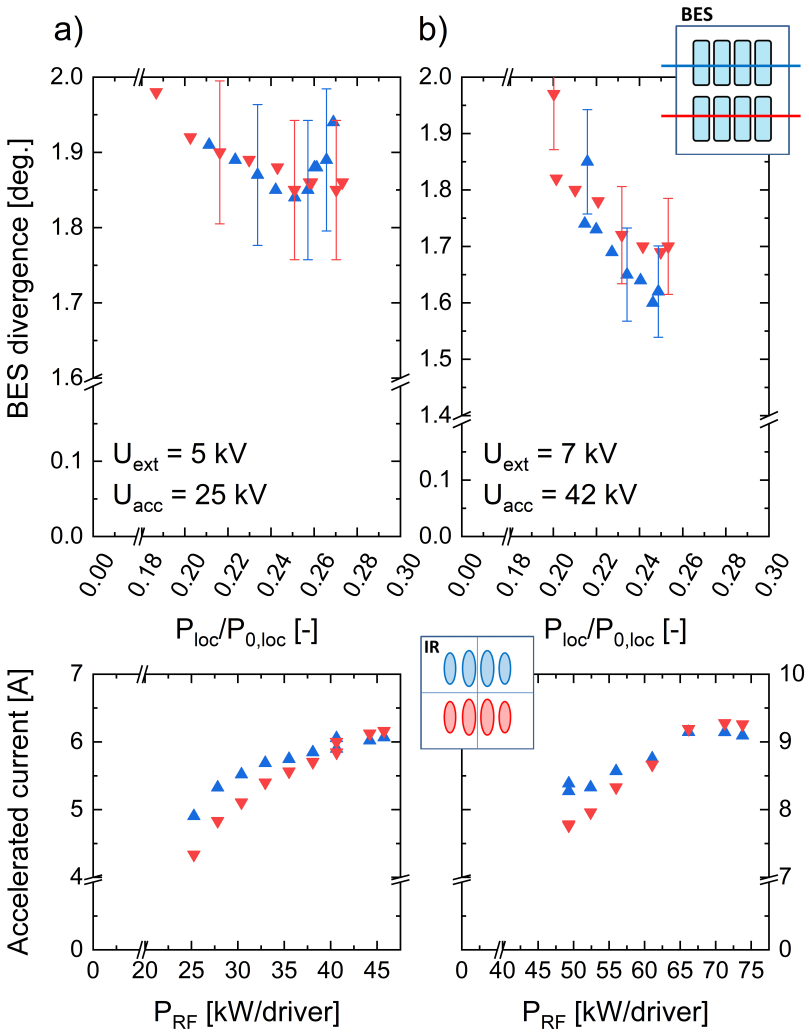

Figure 5.7: BES divergence as a function of the localized perveance for two power variations performed at U_{ext}=5 kV and at U_{ext}=7 kV. The divergence is measured for a LOS located at the top of the beam (LOS 12, blue points) and at the bottom of the beam (LOS 5, red points). The accelerated current for the top and bottom beam segments are shown at the bottom of the figure as a function of the RF power. The pulse parameters are the same of figure 5.3.

the more localized value of accelerated current is not possible with the actual setup. In general, the accelerated current is, within 10% absolute value, symmetric even in case of poor perveance values. The beam properties which are affected by the variation of the perveance are the divergence and, in turn, the beamlet group vertical and horizontal width.

5.3 Electrostatic lens

The acceleration voltage is a fundamental knob for tuning the beam divergence: the optimum ratio $U_{\text{acc}}/U_{\text{ext}}$ at ELISE is determined by finding the minimum of the beam divergence in the case of an acceleration potential variation with fixed extraction voltage. In figure 5.8 three U_{acc} variations are shown at different U_{ext}: in *a)* U_{ext} =5 kV, in *b)* U_{ext} =6.5 kV, and in *c)* U_{ext} =10 kV. With increasing U_{acc} a decrease of the BES

divergence is first observed down to a minimum value, then the beam divergence increases again. For *a)* and *b)* a minimum of divergence below 2 degrees is observed at $U_{\mathrm{acc}}/U_{\mathrm{ext}} = 5.5 - 6$. For the case at 10 kV of extraction the divergence monotonically decreases to 2 degrees with increasing U_{acc} without reaching a clear minimum.

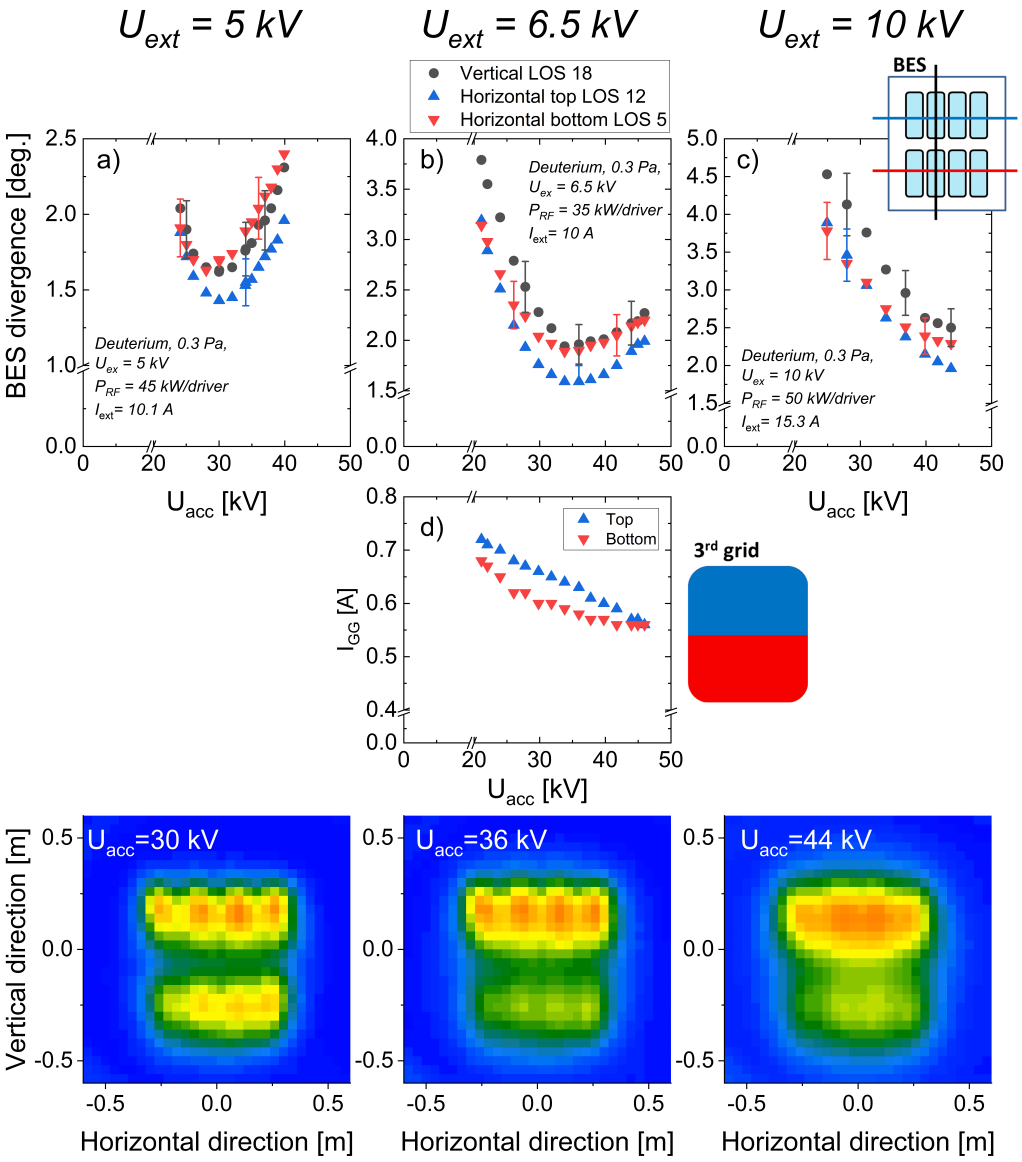

Figure 5.8: BES Divergence as a function of the acceleration voltage for three different cases: in *a)* for U_{ext}=5 kV, in *b)* for U_{ext}=6.5 kV and in *c)* for U_{ext}=10 kV. The divergence is measured for a horizontal LOS located at the top of the beam (LOS 12, blue points), at the bottom of the beam (LOS 5, red points) and for a vertical LOS (LOS 18, black points). In *d)* the GG current for the two grid segments is shown for the acceleration scan of case *b)*. The 2D power density profiles are shown for the best divergence of each scan (see bottom of the figure). Parameters: D, Standard filter field, I_{PG} =4.45 kA + external strengthening magnets (4.6 mT), p_{fill} =0.3 Pa, I_{bias} =55 A.

At the bottom of the figure, the 2D power density profiles are shown for the cases at the minimum divergence to highlight the difference of the beam shape due to the different divergence.
At extraction voltages larger than 10 kV the beam divergence is not optimized since the remaining acceleration voltage available is lower than 50 kV.
In figure 5.8*d)* the GG current I_{GG} for the two grid segments is plotted as function of U_{acc} for U_{ext} =6.5 kV, i.e. the same variation of panel *b)*. The current measured on the grounded grid is due to highly divergent negative ions and due to stripped electrons impinging both on the upstream side and on the downstream side of the grounded grid. Contrary to the beam divergence, the GG current does not show a minimum with increasing U_{acc}, but it monotonically decreases indicating that negative ions are not the major contributors to the GG current (otherwise, the GG current and divergence would show both the minimum at the same acceleration voltage).

5.4 Beam losses within the grid system

The minimization of the destruction mechanisms of negative ions within the grid system is relevant to maximize the efficiency of the NBI system and to minimize the acceleration of unwanted species, i.e. the stripped electrons, and to avoid power loads on the grids and on the beam line components downstream the grounded grid. The investigations shown in this section are focused on determining which particle species is hitting (and thus measured as a current) on the beamline components, thanks to the currents electrically measured on different beam line components as well as the accelerated current measured by the calorimeter. The total extracted current, which is measured as the total current downstream of the EG, accounts for the current collected on all the different surfaces such as GG, GGGHB, tank and the calorimeter (see section 3.2.3) which are on ground potential. On some beamline components the current is independently measured such as on the GG (I_{GG}), and on the GGGHB (I_{GGGHB}), whereas for the calorimeter and the tank no independent current measurement is available. The net current measured on the different components can be due to negative ions, electrons stripped within the grid system or electrons removed from the negative ion due to neutralization in the tank.
The beam power deposited on the calorimeter is due to negative ions and neutrals after the neutralization. The contribution of electrons to the the calorimetric measurement of the beam power is negligible due to the small mass.
The study of the currents on the different beamline components or on the GG as

a function of the perveance, which is correlated to the beam divergence (see figure 2.11), can give useful information on the type of particles impinging the different components. The trends of I_{GG}, I_{GGGHB} and of the accelerated current I_{acc} given by IR calorimetry as a percentage of the corresponding I_{ext} are shown in figure 5.9. The pulses investigated have been performed in hydrogen at a filling pressure of 0.3 Pa.

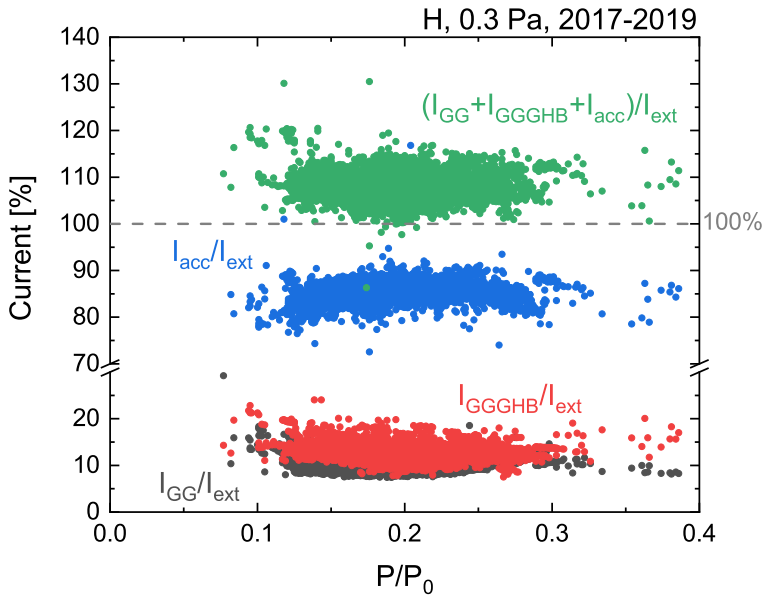

Figure 5.9: Percentage calculated with respect to the extracted current I_{ext} of the accelerated current measured by IR calorimetry I_{acc} in blue, of the GG current I_{GG} in black, of the GGGHB I_{GGGHB} in red and the sum of the three aforementioned in green. All the values are shown as a function of the global perveance P/P_0. About 4700 pulses performed in H at 0.3 Pa from 2017 to 2019.

In average, the accelerated current is between 80% and 90% of the total extracted current and the current collected on the GG is about 10% and on the GGGHB is between about 10 - 15% of the extracted current I_{ext}. The sum of the three contributions is about 110% of the total extracted current electrically measured, thus some particles are counted twice. As an example, a negative ion which is neutralized will be counted as beam power by IR calorimetry, thus contributing to I_{acc}, and the electron can be collected on the GG, contributing to I_{GG}. However, if the electron hits the sidewalls of the tank, whose collected current is included in I_{ext}, the double counting does not occur. On the other hand, it is not possible to know the ratio between neutrals and negative ions at the calorimeter, thus the amount of electrons present in the tank is not known. The comparison of the current collected on the different surface with the evaluation of IR calorimetry suggests that the current collected on the GG and on the GGGHB is by a relevant amount due to stripped electrons either within the the grid system or due to neutralization downstream the last grid.
At low values of P/P_0, i.e. high beam divergence (see figure 2.11), the accelerated current I_{acc} decreases below 80% and the GG and GGGHB currents increase up to

about 20%. In these cases the beam is under-perveant, thus beam scraping on the GG can occur.
To better understand the origin of the particles impinging on the different beamline components, a particle-tracking code such as BBCNI [74] should be used, but this analysis, which is only qualitative, demonstrated that a part of the current measured is definitely due to stripped electrons.

5.5 Conclusions

The beam parameters, such as the vertical and horizontal widths of the beamlet groups, the vertical position of the beam segments and the peak intensity for each beamlet groups, are reliably determined by a fitting routine applied to the 2D power density profile with an uncertainty of 10% on the peak intensity and of 1.5 cm on position and widths. From the fit outputs the accelerated current can be derived for the two beam segments. The comparison between beamlet group vertical and horizontal widths with the beam divergence measured by BES leads to the conclusion that the beam width is mainly determined by the beam divergence.
The study on the beam divergence of the two beam segments shows that the top beam segment is characterized by a higher value of perveance with respect to the bottom beam segment. This is particularly clear for pulses performed with a high RF power and low extraction voltage: in such cases, the uppermost BES LOS are in an over-perveant regime, namely the beam diverge increases by increasing the local extracted current, whereas the bottom beam segment is at the optimum perveance. The different perveance between beam segments is caused by a different extracted current in the two segments, namely the extracted current shows a vertical gradient. The accelerated current measured for the two beam segments is related to the extracted current, thus it is possible to give a localized value of perveance for each beam segment. The perveance curves calculated for the beam segments shows an improved matching. Discrepancies between the perveance curves are anyway still present, thus suggesting the presence of vertical gradient of the extracted current density within the beam segments.
Beam losses on beamline components as well as the grounded grid are studied as a function of the global beam perveance. Electric and calorimetric measurements highlight that a part of the current measured on the beamline components is definitely due to stripped electrons.

6 Plasma and negative ion beam vertical symmetry

In chapter 4 the correlation between local plasma properties, mainly electron density and sheath properties, and co-extracted electron current is carried out. In chapter 5 it was shown how the difference in perveance between the top and bottom beam segments affects the beam width and divergence. In this chapter, given the knowledge about the beam asymmetry, the correlation between plasma parameters and the negative ion beam is worked out in terms of accelerated current symmetry as a function of the two parameters that mostly affect the vertical plasma drifts: the PG biasing (studied here in presence of the rods) and the magnetic filter field. Both parameters affect the charged particle flux at the PG and the vertical plasma drifts. Thus, potentially affecting beam power density and divergence profile.
To study the effects of those parameters on the beam, two different parameter variations have been investigated: an I_{bias} variation and an I_{PG} variation. At first, the evolution of the rod current and the co-extracted electron current is studied, since it gives an insight into the evolution of the ion source performances. The symmetry of the positive ion density is described by using the bias plate current I_{BB} whereas the symmetry of the negative ion density is investigated using the two CRDS LOS. On the beam side, the symmetry is given in terms of accelerated current I_{acc} between the top and bottom beam segments. For all these quantities the symmetry is defined as the value of the top segment divided by the value of the bottom segment, i.e. $x_{\mathrm{top}}/x_{\mathrm{bottom}}$.

6.1 PG biasing variation

With increasing the value of I_{bias}, the vertical asymmetry of the plasma potential between top and bottom of the ion source is enhanced, e.g. see figure 4.21 at page 91. On the other hand, the sheath is more electron attracting at each vertical position in

the ion source by increasing I_{bias}. Thus, resulting in an increase in the current collected on both potential rod segments, but with a different slope on the two segments, since the plasma potential is getting more top-bottom asymmetric with I_{bias}. For the co-extracted electron current a decrease is expected on both EG segments but with a different evolution on the two segments: on the top, where the sheath is already electron attracting for low values of I_{bias}, the reduction of co-extracted electrons is mild whereas on the bottom, where the transition from an electron-repelling sheath to an electron attracting sheath occurs at a medium-high value of I_{bias}, the reduction of co-extracted electrons is enhanced. In figure 6.1 the current on the potential rod and the co-extracted electron current is shown segment-wise in *a)* and *b)*, respectively. About the symmetry of the co-extracted electron current (see the top part of figure 6.1*b)*), the bottom EG segment is higher than the top one, thus the symmetry is < 1 and the value gets smaller by increasing I_{bias}. The total extracted current I_{ext} (shown in figure 6.1*b)*) is slightly affected by the I_{bias}, i.e. it decrease of 1 A in a variation of 100 A of I_{bias}.

The emission of negative ions from the PG can be limited if the positive ion density

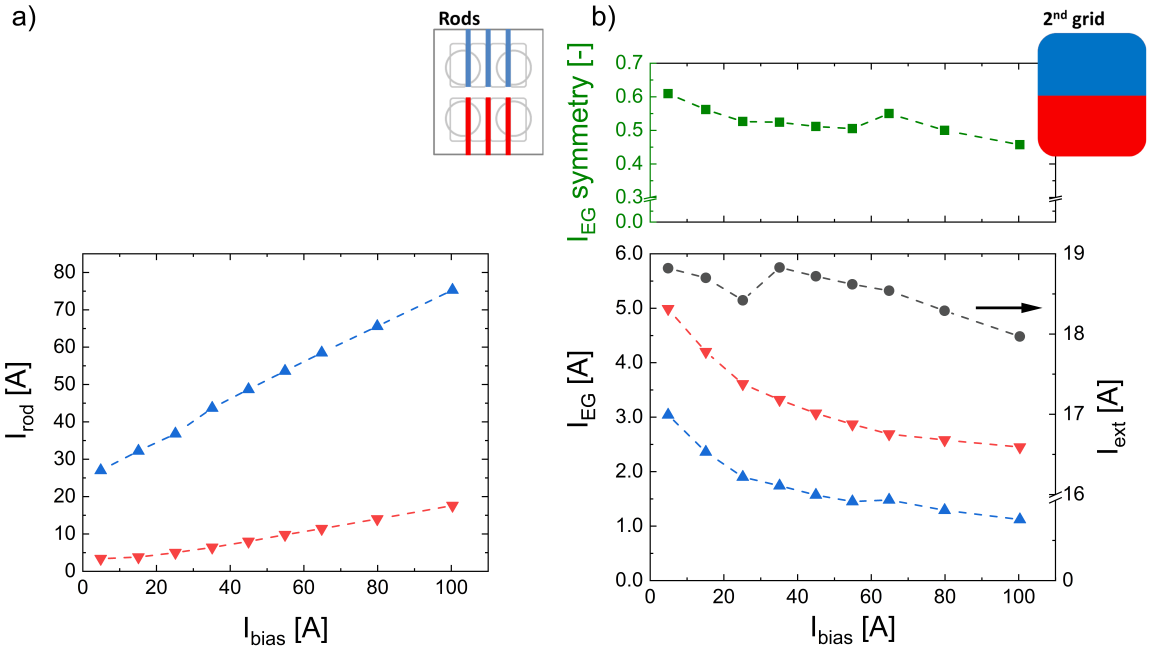

Figure 6.1: *a)* Potential rod current for the two segments (top in blue, bottom in red) as a function of the I_{bias} current. *b)* For the same I_{bias} variation, the co-extracted electron current measured on the two EG segments (blue top, bottom red) and the extracted negative ion current (black) are shown. The symmetry of the co-extracted electron current is shown above the main graph in *b)*. Parameters: H, $P_{\text{RF}} = 50\,\text{kW/driver}$, $p_{\text{fill}} = 0.3\,\text{Pa}$, standard filter field $I_{\text{PG}} = 1.6\,\text{A}$ + external strengthening magnets (1.9 mT), $U_{\text{ext}} = 8\,\text{kV}$, $U_{\text{acc}} = 40\,\text{kV}$

is not sufficient or if the PG sheath is strongly electron attracting, thus preventing the

emission of negative ions from the PG. Both effects are localized to the PG. Localized measurements of the positive ion density are performed with LP, but the effect of the plasma drifts on the symmetry of the flux of positive ions can be studied on the bias plate current, whose symmetry is shown in figure 6.2. The symmetry of the accelerated current is shown as well in figure 6.2 as a function of I_{bias}. By increasing I_{bias}, i.e. PG biasing, the symmetry increases from a value of 1.2 to a value of 1.6, i.e. the current measured on the top bias plate segment is about 60% higher than the bottom one. The increase in the asymmetry of the positive ion density does not imply that the plasma at the bottom is not space charge compensated. Even more so, by considering that the symmetry of the accelerated current is unaffected and that the total accelerated current (not shown) is only slightly affected, i.e. it decreases of about 1 A. The top beam segment carries about 20% more accelerated current than the bottom one.

The symmetry of the negative ion density measured in the plasma is not influenced,

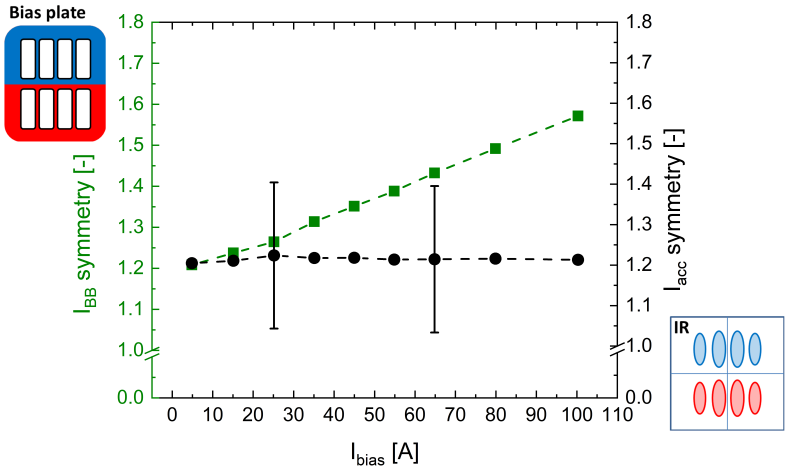

Figure 6.2: Bias plate current symmetry (green) and accelerated current symmetry (black). The values are shown as a function of the I_{bias} current. Same parameters of figure 6.1.

at the measurement positions, by the vertical asymmetry of the positive ion density. In figure 6.3 the symmetry of the negative ion density and the accelerated beam current are shown as a function of I_{bias}. The symmetry of the negative ion density is, within the experimental uncertainty, equal to the unity, namely top and bottom values coincide. The difference in the symmetry between negative ion density and accelerated current can be caused by the different measurement domain: the negative ion density is a local plasma measurement at the center of the beamlet group whereas the accelerated current is integrated over one beam segment, thus averaged on several beamlets.

A constant symmetry of the accelerated current I_{acc} does not exclude that the power

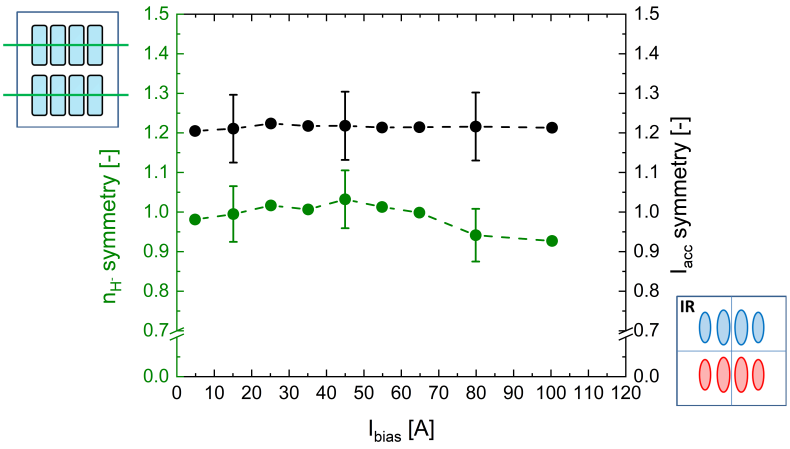

Figure 6.3: Negative ion density symmetry (green) and symmetry of the accelerated current (black). The values are shown as a function of the I_{bias} current. CRDS values measured during the HV phase. Same pulse parameters of figure 6.1.

density profile is affected by the variation of I_{bias}. In figure 6.4 the vertical profile of the BES divergence and the power density profile are shown for four values of I_{bias}. By increasing I_{bias} current, the top beam divergence decreases and, simultaneously, the power density profile of the beam segments is more peaked, i.e. the vertical width of the beam segments decreases. The bottom beam segment has, within the error bars, an identical divergence profile, whereas the power density profile shows a slightly lower peak intensity and vertical width. These observations on the beam profile indicate that the biasing of the PG has mild effects on the beam properties which are detected by the beam diagnostics. More investigations on the effect of the bias on the beam properties are ongoing activities.

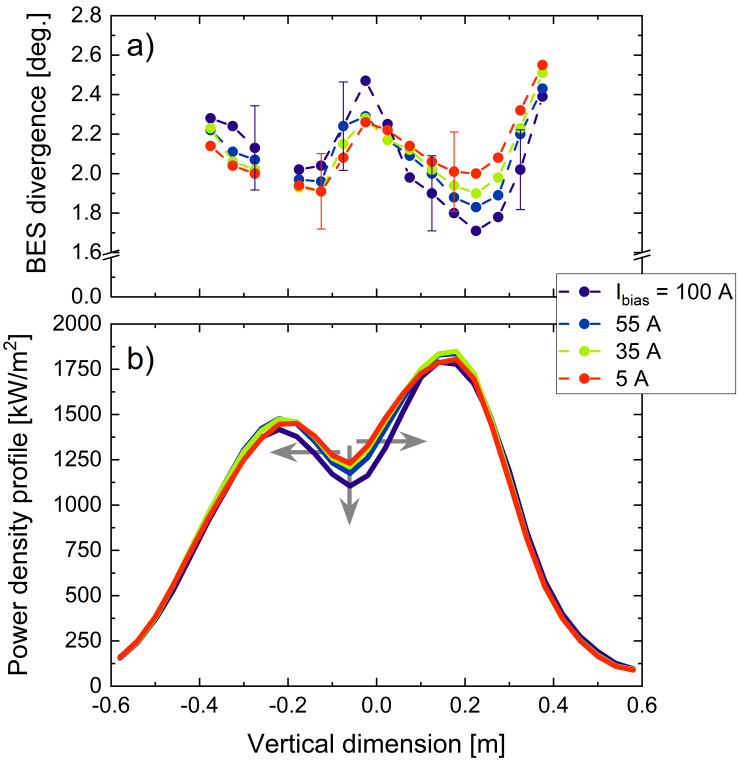

Figure 6.4: *a)* BES divergence vertical profile for three values of I_{bias} current. *b)* Vertical profile of the power density profile retrieved by IR calorimetry. Same pulse parameters of figure 6.1.

6.2 Filter field variation

The filter field strength is the main knob, operationally-speaking, to reduce the co-extracted electron current. The filter field influences the transport and the flux of the charged particles, thus the beam properties as well. The co-extracted electron current and the extracted negative ion current are shown as a function of the magnetic filter field in figure 6.5. The optimum operational value for the magnetic filter field, i.e. the one that maximizes I_{ext} with a low value of co-extracted electrons, is between 1.5 mT and 1.8 mT in hydrogen and for an RF power of 50 kW/driver. The symmetry of the positive ion density measured on the bias plate segments and of the accelerated beam current I_{acc} are shown in figure 6.6 as a function of the magnetic filter field strength. For the lowest magnetic field the currents on the two bias plate segments are identical, whereas for higher values of filter field the top bias plate current is larger than the bottom one. At low magnetic field, the flux of energetic electrons can anyway contribute to the bias plate current. The symmetry of the accelerated current is between 1.1 and 1.2 for all the cases with a filter field higher than 1 mT. The accelerated current symmetry is not affected by the change of symmetry of the positive ions, thus suggesting that the plasma drift has a small impact on the accelerated current symmetry.

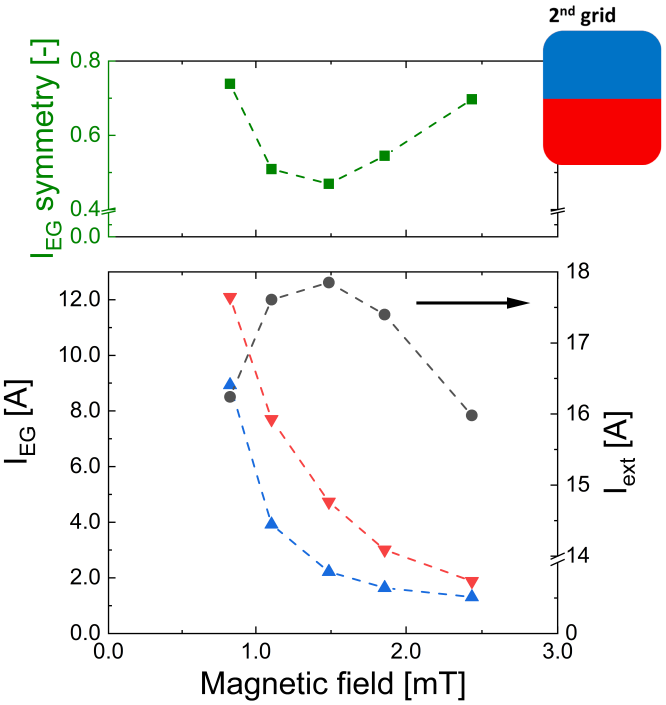

Figure 6.5: Co-extracted electron current measured on the two EG segments (top in blue, bottom in red) as a function of the filter field. The extracted negative ion current is shown in black. Above the main graph, the electron symmetry is shown. Parameters: H, Standard filter field, $P_{\mathrm{RF}} = 50$ kW/driver, $p_{\mathrm{fill}} = 0.3\,\mathrm{Pa}$, $I_{\mathrm{bias}} = 35\,\mathrm{A}$, $U_{\mathrm{ext}} = 7\,\mathrm{kV}$, $U_{\mathrm{acc}} = 35\,\mathrm{kV}$.

The symmetry of the negative ion density measured by CRDS is shown in figure

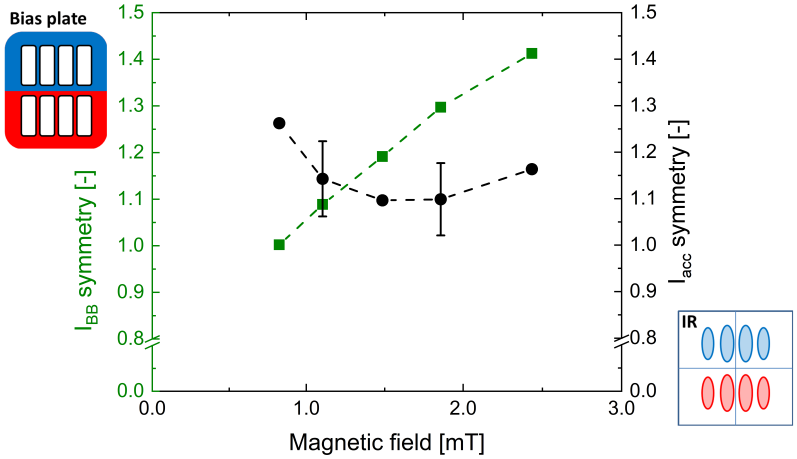

Figure 6.6: Bias plate current symmetry (green) and accelerated current symmetry (black). The values are shown as a function of the magnetic filter field. Same parameters of figure 6.5

6.7 together with the symmetry of the accelerated current given by IR calorimetry. The symmetry of the negative ion density is slightly lower than one for a magnetic field value higher than 1 mT. The symmetry value, which is between 0.9 and 1, is not strongly affected by the magnetic field variations. On the other hand, the beam properties are strongly affected by the filter field value. In figure 6.8, the vertical power density profile from IR calorimetry and the vertical beam divergence profile are shown for three values of filter field, i.e. a low value, an intermediate one, and a high value. The beam divergence of the top beam segment is, within the error

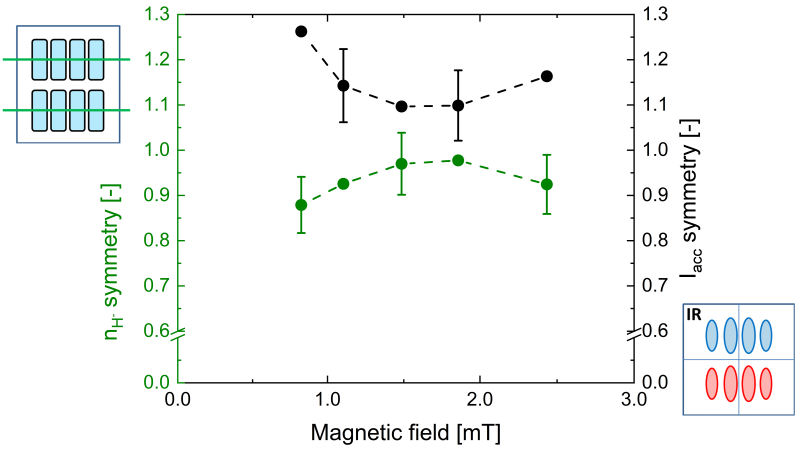

Figure 6.7: Negative ion density symmetry (green) and accelerated current symmetry (black). The values are shown as a function of the magnetic filter field. CRDS values measured during the HV phase. Same pulse parameters of figure 6.5.

bars, similar in absolute values, but the power density profile gets narrower and the beam divergence profile gets peaked. The bottom beam segment has a similar divergence profile, but different values of divergence according to the magnetic filter field. The lowest beam divergence is obtained at a magnetic filter field of 1.5 mT, when the extracted negative ion current, and consequently the accelerated one, is at the maximum value. At medium magnetic field strength, the difference in peak intensity between the top and bottom beam segments, observed in figure 6.8*b)*, is compensated by a larger vertical width of the bottom beam segment, thus the accelerated current of the two segments is in absolute values similar. The vertical beam deflection affects the vertical position of the beam on the calorimeter, thus the beam profile obtained with a low magnetic field is more centered on the calorimeter. The difference in vertical position between the low field case and the high field case is of 2.5 cm. To fulfill the ITER requirements in terms of extracted negative ion current with a low amount of co-extracted electrons and to comply with the beam power density homogeneity requirement, which in ELISE is estimated as beam accelerated current symmetry, the magnetic filter field must be adjusted and kept to an intermediate value between 1.5 mT and 2 mT (hydrogen at 0.3 Pa). In general, a strong magnetic filter field results in an asymmetry beam, whereas at a low magnetic filter field the extracted negative ion current is low, thus affecting the beam divergence.

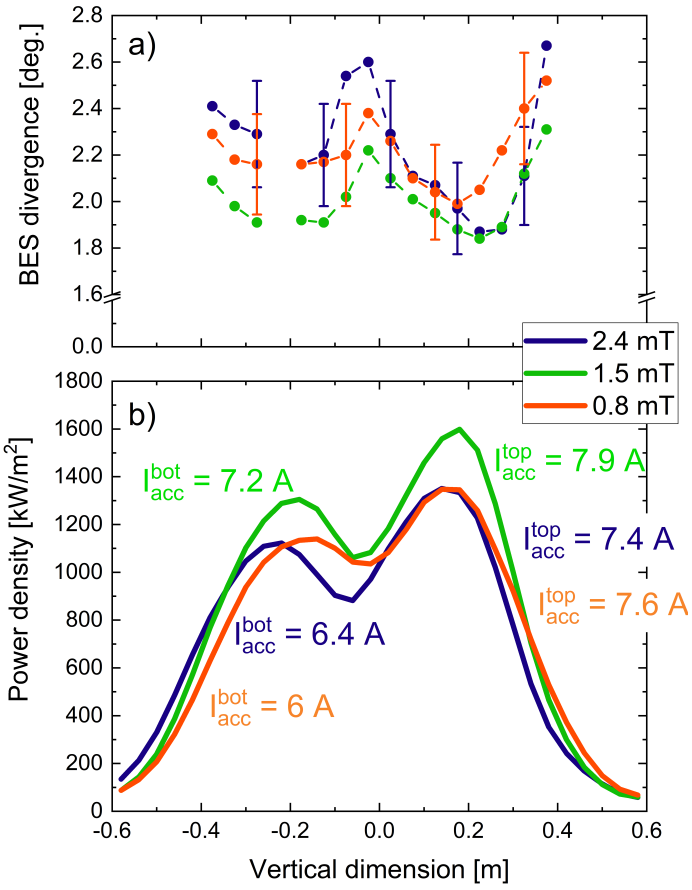

Figure 6.8: *a)* BES divergence vertical profile for three values of filter field. *b)* Vertical profile of the power density. Same pulse parameters of figure 6.5.

6.3 Beam homogeneity within the segments

The beam is symmetric in terms of beam segment accelerated current, with a different peak intensity which is compensated by a larger beam width at the bottom beam segment. The analysis is performed on the beam properties, up to now, directly on the averaged values over the beam segments, but non-homogeneities on a smaller scale, i.e. within the beam segments, cannot be excluded. It this section, one case with and higher resolution than the beam segment, on both beam and ion source is discussed. This analysis is useful to get a hint about which parameters in the plasma may cause the asymmetry in peak intensity between beam segments. In figure 6.9 the vertical profile of the positive ion density in the plasma (top), of the plasma potential (top), of the beam power density profile (center) and of the beam divergence (bottom) are shown. The vertical position of the 2D power density profile and of the BES divergence profile are corrected for the vertical beam deflection caused by the filter field. The negative ion density measured at the center of the top and bottom ion source halves as well as the currents on the grounded grid segments are

reported in the figure.

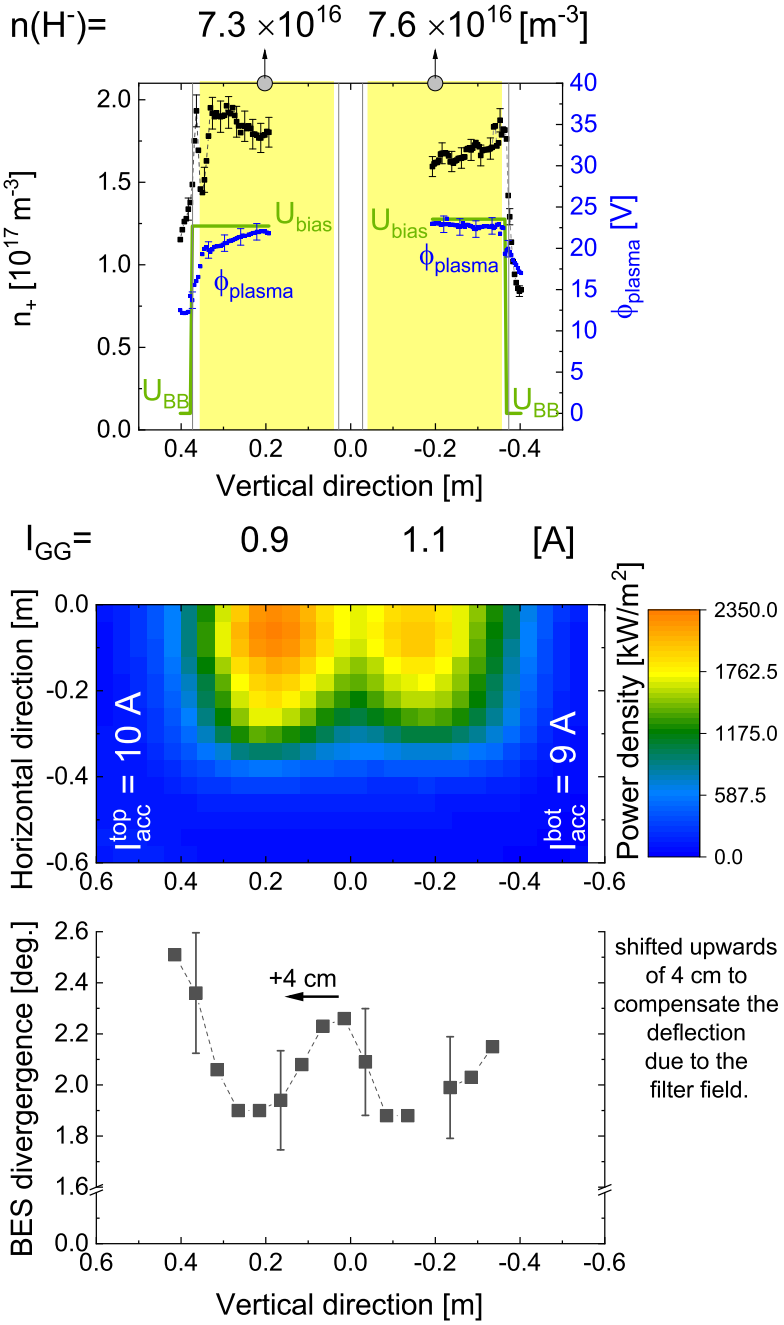

Figure 6.9: *top*: Vertical profile of the positive ion density in the plasma (black points) and of the plasma potential (blue points). At the top *center*: 2D beam power density profile. *bottom*: BES divergence vertical profile. Reported in the figure is also the negative ion density measured by CRDS and the currents on the grounded grid segments. Parameters: H, 0.3 Pa, $P_{\mathrm{RF}} = 60\,\mathrm{kW/driver}$, $I_{\mathrm{ext}} = 22.3\,\mathrm{A}$, $I_{\mathrm{PG}} = 1.6\,\mathrm{kA}$ + external strengthening magnets (1.9 mT), $I_{\mathrm{bias}} = 35\,\mathrm{A}$, $U_{\mathrm{ext}} = 8\,\mathrm{kV}$, $U_{\mathrm{acc}} = 40\,\mathrm{kV}$.

The symmetry of the positive ion density is close to the unity between top and

bottom of the ion source as well as the negative ion density, whose value is reported at the top of figure 6.9. The currents measured on the grounded grid segments are small compared to the extracted negative ion current (22.3 A) and similar in absolute value. Thus, similar beam losses within the grids can be assumed for the two segments. The beam 2D profile, see center of figure 6.9, highlights that the top beam segment has a higher peak intensity and that the accelerated current in about 1 A higher than the bottom accelerated current. The beam symmetry, defined between top and bottom, is 1.1. The beam divergence at the center of the beam segments has the same value, thus also for the beam divergence is top-bottom symmetric. Nevertheless, the beam segments are qualitatively and quantitatively different, e.g. in peak intensity and horizontal width. These differences are not caused by a different density, either of positive ions or negative ions, in the plasma, since the values are symmetric. However, the PG sheath at the uppermost positions of the is source is strongly electron attracting, i.e. $U_{\text{bias}} - \phi_{\text{plasma}} \approx 2\,\text{V}$. With such a PG sheath, emission from the PG of negative ions into the plasma is strongly hindered. But, at the same position, i.e. at the uppermost part of the beam, the beam intensity is the highest, thus suggesting that not only negative ions are effectively created in that region, but are, also extracted. Two physical aspects have been neglected and can explain the experimental observations: the presence of a potential well, whose depth is not accessible experimentally, affecting the emission of negative ions from the PG into the plasma and the presence of negative ions, which are emitted from the chamfered part of the PG, immediately extracted. Moreover, the PG sheath may influence the angle of the negative ions crossing the meniscus, thus affecting the beam divergence. This analysis shows, once more, that the relevant physics for the determination of the beam properties is the sheath physics during the extraction phase.

7 Isotope effect

The ITER target values for the extracted negative ion current with an electron to ion ration lower than one in deuterium are still not reached due to the high amount of co-extracted electrons. A comparison of the two hydrogen isotopes is carried out to investigate the causes of the increase of the co-extracted electrons in deuterium.

7.1 Comparison at the same source parameters

The following experimental campaigns are carried out at fixed source parameters and switching the isotope between two consecutive pulses. To sustain extraction in both H and D at the same source parameters the pulses have been performed at reduced parameters, i.e. extraction voltage and RF power, adapted to the much higher amount of co-extracted electrons in deuterium. The value of filter field chosen for hydrogen, i.e. 3.3 mT, is too strong thus reducing the positive ion flux and in turn, due to space charge limitation, the extracted negative ion current. On the other hand, in deuterium the filter field strength in not high enough, thus resulting in a high amount of co-extracted electrons. In figure 7.1 the time-traces of the co-extracted electron current density and of the extracted negative ion density are shown for hydrogen and deuterium. The co-extracted electrons are about four to nine times higher in deuterium than in hydrogen and the co-extracted current density is significantly more unstable in time. The negative ion current density is slightly reduced in deuterium compared to hydrogen. In general and especially for the case of deuterium, the temporal instability of the source performance is addressed to a degradation in time of the PG work function, which is turn given by a higher removal of Cs from the walls compared to the deposition rate [87].

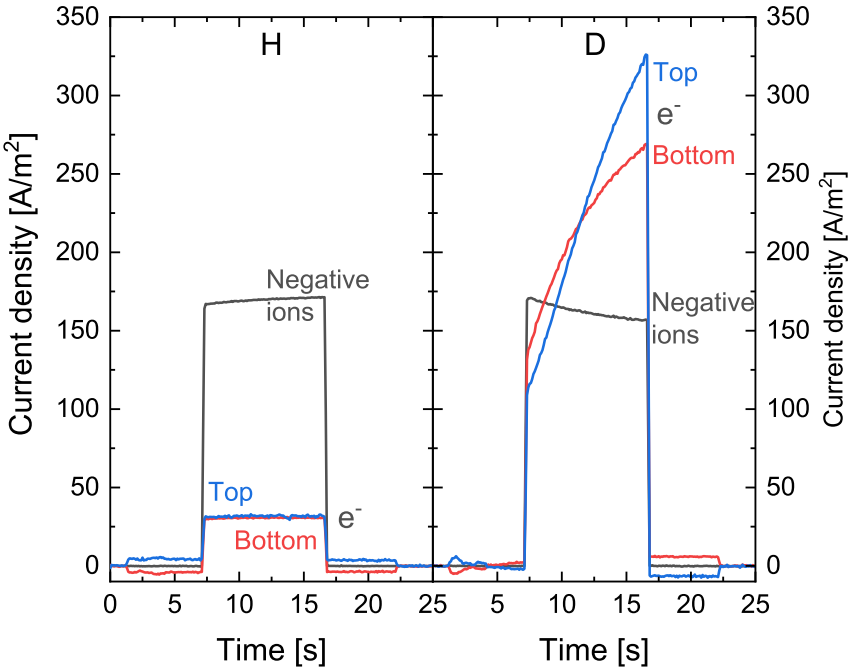

Figure 7.1: Pulses in H and D at the same source parameters: $p_{\text{fill}} = 0.3\,\text{Pa}$, $P_{\text{RF}} = 50\,\text{kW/driver}$, $U_{\text{ext}} = 7\,\text{kV}$, $I_{\text{PG}} = 3\,\text{kA}$ + external magnets strengthening (3.3 mT), $I_{\text{bias}} = 35\,\text{A}$. In black the negative ion current density, in blue and in red the co-extracted electron current density for the top and bottom EG segment, respectively.

In figure 7.2 the results of several measurements at the top and the bottom side of the ion source are shown as a function of the pulse number. The change of isotope immediately affects the measurements and the values are stable for the pulses afterwards, thus no long term offect of the Cs redistribution is affecting the results. In deuterium with respect to hydrogen the emission in the driver is higher due to the higher atomic density. The symmetry of the emission between top and bottom is slightly shifted in deuterium, being the emission in the bottom driver about 10% higher than the one in the top one. The top and bottom values are anyway compatible within the error bars.

The current collected on the two segments of the potential rods in hydrogen shows a strong asymmetry between top and bottom, i.e. the top current is four time higher than the bottom one. In deuterium this asymmetry is even more enhanced: the upper rods collect about 27% more current and the lower rods about 20% less compared to the case in hydrogen. As addressed in section 4.2.1, the current measured on the potential rods is due to the flux of electrons, thus the current is determined by the electron density and by the sheath properties at the rods, i.e. $U_{\text{bias}} - \phi_{\text{plasma}}$. As it will be observed later in this section, the positive ion density symmetry is improved

in deuterium, thus a better symmetry of the electron density can be assumed, due to the plasma quasi neutrality. A better symmetry of the plasma can result in a more asymmetric rod currents only in case of a significantly more asymmetric plasma potential between top and bottom ion source in deuterium with respect to hydrogen. The currents collected on the two parts of the bias plate, given by positive ions, increase differently by changing the gas type: the increase of current in deuterium is more pronounced in the bottom part (+42%) than in the top part (+27%). In deuterium the symmetry of the current is improved than in hydrogen. An indication of the variation of the positive ion density with the change of isotope can be given from the bias plate current, under the assumption than the positive ions have the same energy, thus only a factor $\sqrt{2}$ lower velocity for deuterium positive ions has to be included. The ratio between the positive ion density in deuterium and in hydrogen can be estimated as

$$\frac{n_+^D}{n_+^H} \approx \frac{I_{\mathrm{BB}^D}}{I_{\mathrm{BB}^H}}\sqrt{2} = 1.53 \cdot \sqrt{2} \approx 2 \tag{7.1}$$

for the bottom beam segment and 1.7 for the top beam segment. The increase of negative ion density in deuterium is different between top and bottom and the result is a more symmetric positive ion density in deuterium than in hydrogen.

The PG and rods potential $\mathrm{U_{bias}}$ increases from 22.1 V in H to 28.5 V in D as shown in figure 7.2*d)*. One physical explanation for this observation is the mass effect on the plasma potential (see equation 2.7, page 18).

The negative ion density, see *e)*, is constant when changing the isotope at the top whereas in the bottom the density increases of about 20% in deuterium with respect to hydrogen. The increase of negative ion density is explained by the increase of the atomic flux, given by an higher atomic to molecular density ratio in D than in H. However, the negative ion density at the top of the ion source does not increase. The reason for this asymmetry is not clear, but it can be due to the high electron density, thus due to an increase of the destruction rate of negative ions by collisions with electrons.

For what concerns the source performance, i.e. extracted negative ion current and co-extracted electrons, (see *f)*) the negative ion current is slightly lower in D than in H whereas the co-extracted electron currents are ten times higher. The 10% lower extracted current density in deuterium results from a lower velocity of the deuterium atoms $v \propto \sqrt{m}$ and from a higher atomic density. The influence of an higher electron density can also increase the negative ion destruction rate in the plasma, thus reducing the negative ion density in the plasma and the extracted negative ion current.

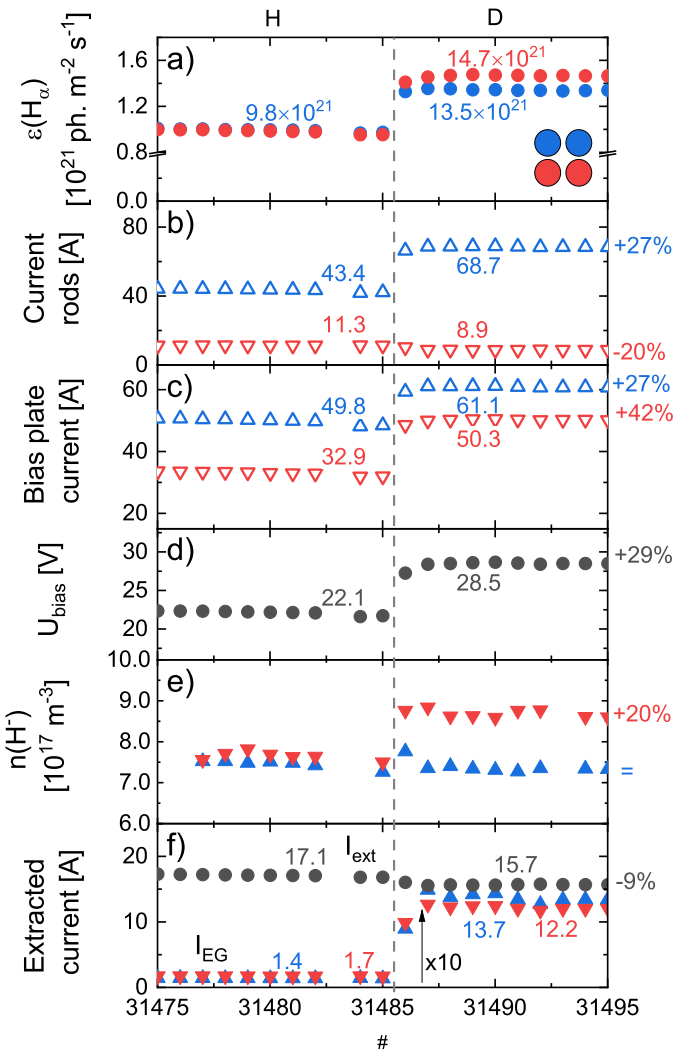

Figure 7.2: Variation of OES signals in the driver (*a)*) and electrical measurements (*b)* to *f)*) at the same source parameters but different gas type. In *e)* results from the CRDS are shown. From top to bottom: OES $\varepsilon(H_\alpha)$ in the drivers, current measured on the potential rods, bias plate current, PG and rod bias voltage, negative ion density and, extracted negative ion and electron current for several pulses. Same parameters of figure 7.1.

For the investigated source parameters, the aforementioned observations lead to the conclusion that, by changing from H to D, the symmetry of the positive ion density improves. Indications that the asymmetry of the plasma potential is enhanced in deuterium compared to hydrogen are retrieved by studying the potential rod currents.
In the following part the beam properties are discussed to understand the effect of the isotope change on the beam properties. In figure 7.3, the 2D power density maps are compared for H and D pulses in *a)* and *b)*, respectively. The beam in deuterium is about 2 cm less deflected downwards because the deuterium particle velocity after being accelerated is lower (see equation 2.20, page 28), thus the Lorenz force is a

factor $\sqrt{2}$ less intense.

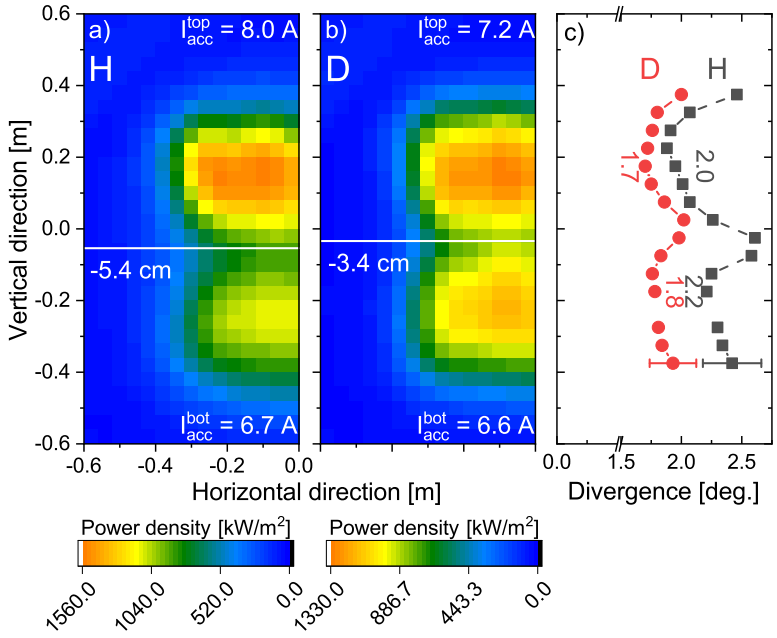

Figure 7.3: Left halves of the 2D map of the power density measured at the calorimeter in *a)* and *b)*. The color-scale used for each map is normalized for the maximum of each plot in order to highlight the changes in relative intensity between top and bottom. In *c)* the BES divergence profiles are shown for the case in hydrogen (black) and for the case of deuterium (red). Pulses in H and D performed at the same operational parameters: $p_{\text{fill}} = 0.3\,\text{Pa}$, $I_{\text{bias}} = 35\,\text{A}$, $I_{\text{PG}} = 2.4\,\text{kA}$ + strengthening external magnets (2.7 mT), $P_{\text{RF}} = 50\,\text{kW/driver}$, $U_{\text{ext}} = 7\,\text{kV}$, $U_{\text{acc}} = 35\,\text{kV}$.

A different symmetry between top and bottom beam segment is observed by comparing the beam segment intensity and the accelerated current: in hydrogen the top beam segment is more intense than the bottom one and it carries about 20% more accelerated current. In deuterium the accelerated current of the top beam segment is about 9% more than the bottom one. The higher accelerated current at the bottom beam segment with respect to the top one is correlated to an increase of the bottom negative ion density with respect to the top one (see figure 7.2*e)*).

The BES divergence profile shows that the beam deflection (downward) is more enhanced in H than in D, in agreement with IR calorimetry results. In deuterium, the beam segment divergence is lower than in hydrogen. The lower divergence is a general effect caused by an higher normalized perveance $P/P_0 \propto \sqrt{m}$ which gives, for the same extracted current and in the under-perveant regime, a lower divergence in D than in H. The improvement of the accelerated current symmetry causes an improvement of the symmetry of the divergence, being the top and bottom beam segment divergence more symmetric in deuterium than in hydrogen.

The amount of co-extracted electrons is such that the electron to ion ratio is largely above one (see figure 7.2*f)*), thus not ITER relevant. Thus, the magnetic field has to be raised to higher values.

7.2 Comparison at adjusted source parameters

To reduce the amount of co-extracted electrons an stronger filter field is needed. Consequently, the plasma drifts will be enhanced, thus modifying the vertical plasma and beam profile. The effect is studied by comparing three pulses: one pulse in hydrogen at I_{PG}=3 kA (3.2 mT), one pulse in deuterium at I_{PG}=3 kA (3.2 mT) and one pulse in deuterium at I_{PG}=4.45 kA (4.6 mT). All the other source parameters as well as the configuration of the external magnets are unchanged.

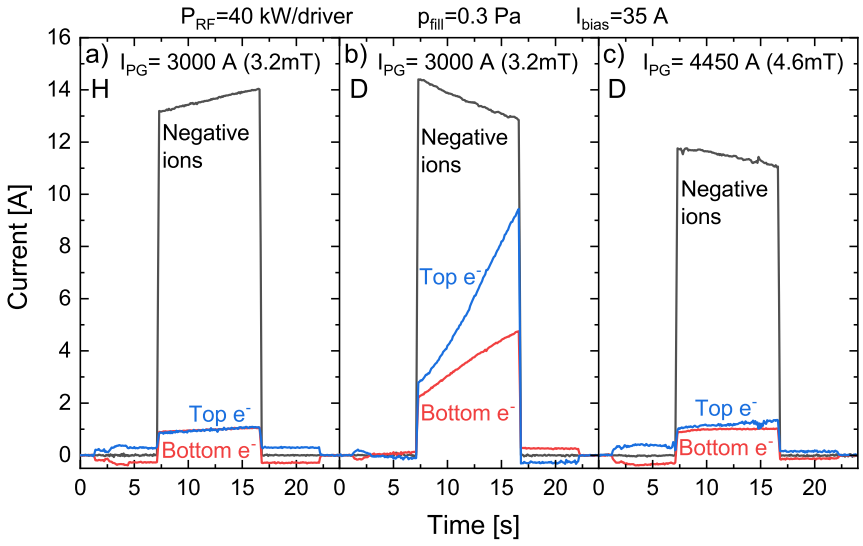

Figure 7.4: Time-trace of the extracted negative ion current (black) and of the co-extracted electron current measured on the top (blue) and bottom (red) half of the EG. The pulses are performed in hydrogen *a)* and deuterium *b)* at the same identical source parameters and in deuterium *c)* at increased I_{PG}. Pulse parameters: p_{fill} = 0.3 Pa, P_{RF} = 40 kW/driver, I_{bias} = 35 A, U_{ext} = 7 kV, U_{acc} = 35 kV.

In figure 7.4 the time traces of the co-extracted electron current and extracted negative ion current are shown for each case. In deuterium, by increasing the I_{PG} from 3 kA to 4.45 kA, a strong reduction and a temporal stabilization of the co-extracted electrons is observed. The absolute value of the co-extracted electrons is similar to the hydrogen case. The extracted negative ion current, however, decreases by about

14%. This means that, on one hand, a stronger magnetic filter field stabilizes and reduces the co-extracted electrons and, on the other hand, it decreases the extracted negative ions.

The plasma properties are studied by means of the RF compensated Langmuir probe: in figure 7.5 the I-V characteristics for the three cases under investigation are shown. In deuterium, the positive ion density is identical to the hydrogen case. The amount of Cs locally present at the PG in hydrogen was extremely high with the results of a extremely high positive ion density (higher than for the deuterium case) which is not in general observed (phenomenon known as over-conditioning [87]). In deuterium a further decrease of the positive ion density is caused by a stronger filter field.

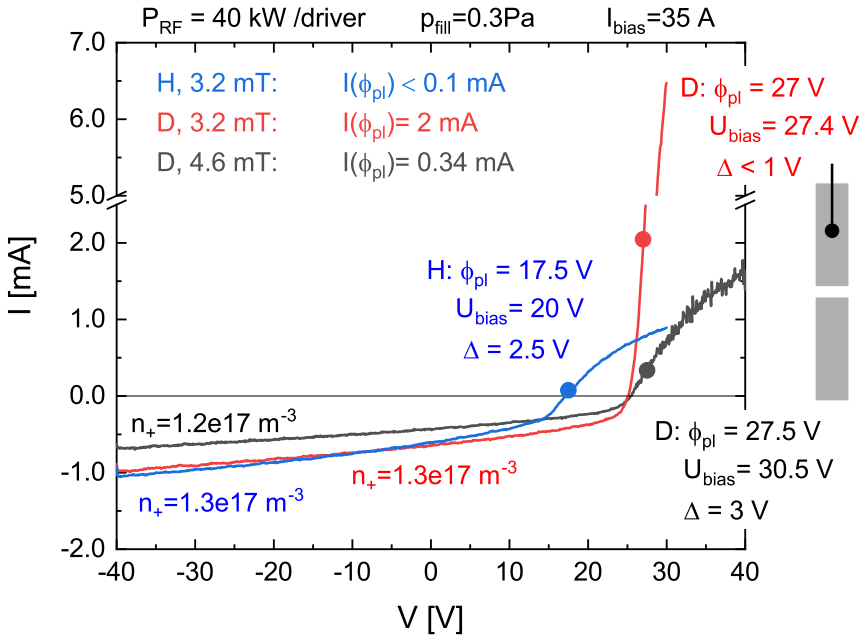

Figure 7.5: I-V characteristics from the RF-compensated movable probe positioned at about 200 mm, i.e. at the center of the beamlet group. Probe characteristics measured during the HV phase. The parameters of the pulses are shown on the figure, U_{ext} =7 kV and U_{acc} =35 kV. The points along the I-V curves represent the plasma potential. In the figure also the positive ion density is reported.

The plasma potential, indicated by dots, increases of about 9.5 V in deuterium compared to hydrogen. One reason for the increase of the plasma potential observed in deuterium is the higher mass of the deuterium positive ions. Consequently to the increase of the plasma potential, the PG potential U_{bias} increases. The current at the plasma potential $I(\phi_{\mathrm{plasma}})$ is about 20 times higher in D than in H for the same

source parameters, thus the electron density is strongly reduced in H compared to D. By increasing the filter field, $I(\phi_{\text{plasma}})$ decreases to a value comparable to the hydrogen case. In the three cases discussed, at the position investigated with the Langmuir probe, the PG is electron attracting, namely $U_{\text{bias}} > \phi_{\text{plasma}}$, but the difference $\Delta = U_{\text{PG}} - \phi_{\text{plasma}}$ reported in figure 7.5 strongly depends on the filter field strength.

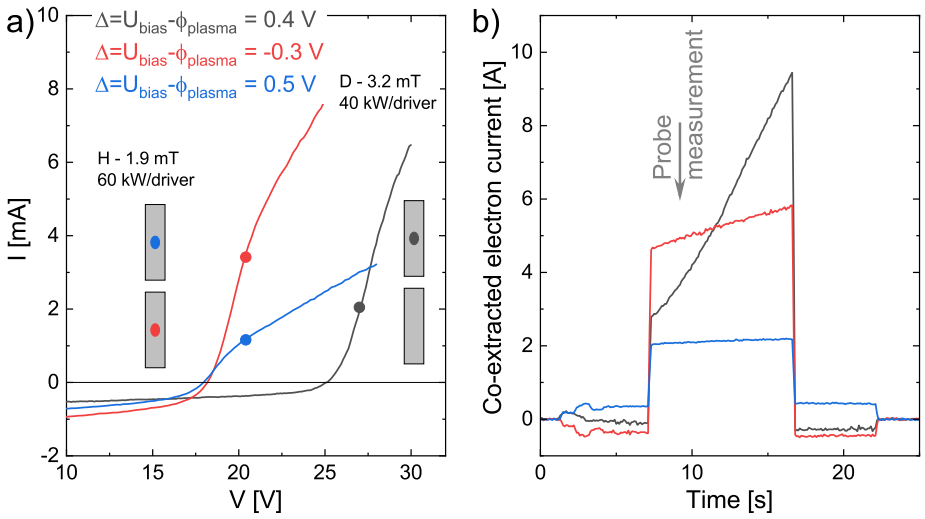

Figure 7.6: *a)* IV curves measured during the HV phase with the movable RF-compensated LP at the center of the beamlet group. *b)* Timetraces of the co-extracted electron current measured on EG segment. Red and blue: H, 0.3 Pa, filter field strength 1.9 mT, $P_{\text{RF}} = 60$ kW/driver, I_{bias}=35 A, U_{ext} =8 kV. Black: D, 0.3 Pa, filter field strength 3.2 mT, $P_{\text{RF}} = 60$ kW/driver, I_{bias} =35 A, U_{ext}=7 kV.

The higher prevalence of the electron flux in the I-V curve in deuterium, and consequently the electron density in the plasma, does not explain, in itself, such high amount of co-extracted electrons. In figure 7.6*a)* three I-V curves are compared: two of them measured in hydrogen with a filter field of 1.9 mT (the same I-V curves of figure 4.19) and one in deuterium at 3.2 mT (the same I-V curve of figure 7.5). It can be observed that the I-V curve measured in H at the bottom half of the ion source shows a similar value of $I(\phi_{\text{plasma}})$ to the I-V curve measured in D at 3.2 mT. The values of $\Delta = U_{\text{bias}} - \phi_{\text{plasma}}$ measured in the three cases are similar, i.e. $\Delta \approx 0$. The time traces of the co-extracted electrons measured on the corresponding EG segment are shown in *b)*. In deuterium compared to hydrogen, the co-extracted electron current is strongly unstable with time. Thus, clearly showing a PG work function degradation over the extraction phase, which causes a decrease of the negative ion emission at the PG and an increase of the electron density and, in turn, of the co-extracted

electron current. It can be deduced that, if a stable PG work could be achieved, the co-extracted electron current would be temporally stable in time and, at least for the case shown in figure 7.6, comparable in absolute values to the hydrogen case even at lower magnetic field strength.

In figure 7.7 the 2D maps of the beam power density for the three cases under discussion are shown. As observed in the previous section, in deuterium for the same value of filter field the symmetry of the top and bottom accelerated current as well as the beam divergence symmetry is improved compared to the corresponding hydrogen case. Nevertheless, the stronger filter field necessary to stabilize the co-extracted electrons affects the beam: a lower extracted negative ion current (I_{ext} =11.3 A) results in a worst divergence, i.e. 2.3 degrees for the bottom beam segment, at 4.45 kA compared to 3 kA, i.e. I_{ext} =13.8 A with 1.7 degrees for the bottom beam divergence. In deuterium both at 3.2 mT and at 4.6 mT, the beam segment accelerated currents are within 10% one from the other. For the low field case, the top beam accelerated current is higher than the bottom case, which is not the case for D at 4.6 mT of filter field.

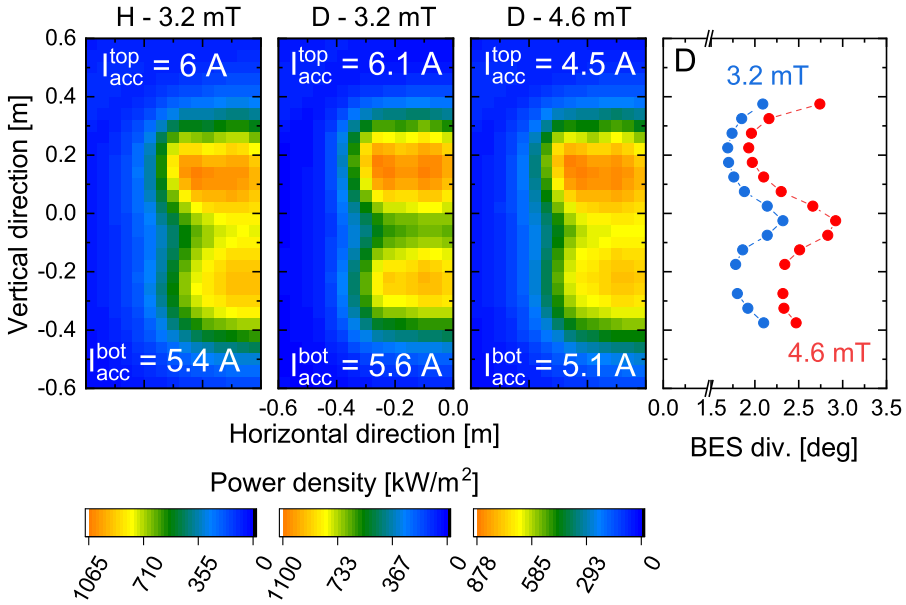

Figure 7.7: Left half of the 2D power density map measured by IR calorimetry at the diagnostic calorimeter. The first panel is the case in H at 3.2 mT, the second and third panel are the pulses performed in D at 3.2 mT and 4.6 mT, respectively. For each case the accelerated current calculated at the level of the beam segments is reported. The leftmost figure shows the vertical profile of the BES divergence for tha cases in D, at 3.2 mT and 4.6 mT in blue and red, respectively.

8 Long pulse stability

Long pulses (up to one hour in deuterium or 1000 s in hydrogen) are one of the main requirements for ITER and the stability of the co-extracted electrons is one of the main challenges to tackle. The temporal instability of the co-extracted electrons and of the extracted negative ions over the pulse duration is the result of a degradation of the PG work function over the pulse length. To fulfill the ITER requirements it is mandatory to develop measures, based on the physical insight, to counteract the increase of the co-extracted electron current.

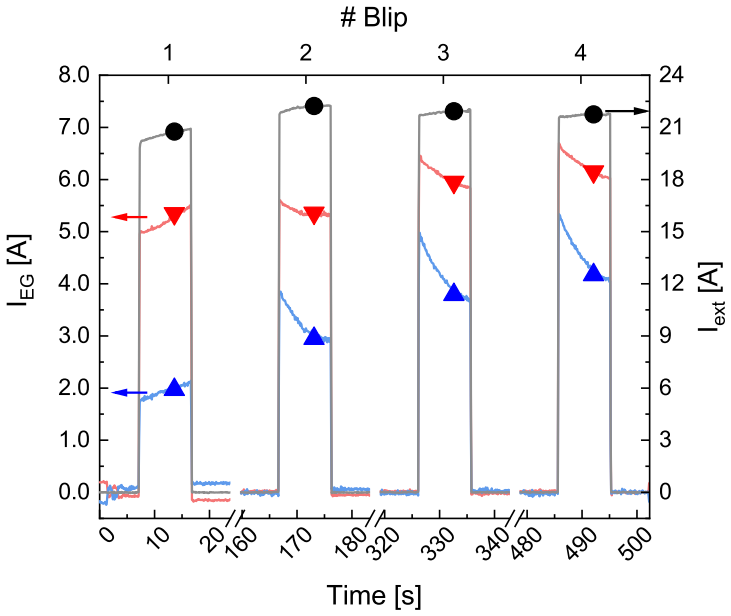

Figure 8.1: Temporal evolution of the co-extracted electron current measured on the top and bottom EG segments shown in blue and red, respectively. In black the extracted negative ion current is shown. The symbols are the value averaged, the lines are the time traces. Pulse parameters: H, 530 s long pulse with 4 extraction phases (blip), $p_{\mathrm{fill}} = 0.3\,\mathrm{Pa}$, $P_{\mathrm{RF}} = 60\,\mathrm{kW/driver}$, $I_{\mathrm{bias}} = 35\,\mathrm{A}$, $I_{\mathrm{PG}} = 1.6\,\mathrm{kA}$ + external strengthening magnets (1.9 mT), $U_{\mathrm{ext}} = 8\,\mathrm{kV}$, $U_{\mathrm{acc}} = 40\,\mathrm{kV}$.

An example of a medium-long pulse in hydrogen, i.e. the plasma on time is less than the ITER requirement but more than the 20 s short pulse, with four extraction

phases of 9.5 s each is shown in figure 8.1. The extracted current I_{ext} is almost constant at 22 A from the second extraction blip onward whereas the co-extracted electron current on the two EG segments increases from beam blip to beam blip. The trend of the two EG segment is different: in the top half the increase is more pronounced than the bottom part. Within the extraction phases, the co-extracted current decreases, thus the extraction phase has a beneficial effect on the Cs redistribution. Two strategies for improving the long pulse stability can be pursued:

- Tackling the Cs dynamics, thus ensuring a sufficient flux of Cs on the PG over the pulse duration.
- Tackling the plasma symmetry in term of plasma density and/or PG sheath to reduce and symmetrize the of co-extracted electrons in long pulses.

In the previous chapters it has been demonstrated that the co-extracted electrons are determined by the electron density in the plasma and by the sheath properties at the PG, i.e. $U_{\text{bias}} - \phi_{\text{plasma}}$. In this chapter the relation between plasma parameters and co-extracted electron current is studied in a long pulse, mainly focusing on the vertical symmetry of the co-extracted electron current. The correlation between plasma symmetry and negative ion beam symmetry is studied in terms of negative ion density symmetry measured in the plasma and accelerated current for the beam segments.

8.1 Co-extracted electrons

The following investigation is performed with the movable RF- compensated LP in the standard and reversed filter field configuration for medium long plasma pulses and four beam blip performed with the same source parameters and comparable Cs conditioning. The extracted current I_{ext} and the co-extracted electrons I_{EG} are identical in absolute values within 15% (comparison done for the first beam blip). Thus, the pulses can be combined to study the vertical asymmetry of the plasma profile and of the electron density. In the following, *top* refers to measurements with the movable LP performed at the top of the ion source with the standard FF configuration whereas *bottom* refers to measurements performed at the top of the ion source with the reversed FF configuration (virtually at the bottom). One beam blip in the reversed configuration is missing, due to a temporary interruption of the HV availability. The plasma potential profile ϕ_{plasma} is plotted in figure 8.2. The main characteristics (present also for the case under investigation) of the plasma

profile are presented in chapter 4, e.g. figure 4.17. On the top of the ion source, the plasma potential ϕ_{plasma} is always lower than the PG potential U_{bias}, thus the sheath is electron attracting. At the bottom of the ion source the plasma potential is identical, within the error bars, to U_{bias} for the first and second beam blips, whereas from the third one the plasma potential is higher than U_{bias}, i.e. the sheath is electron repelling.

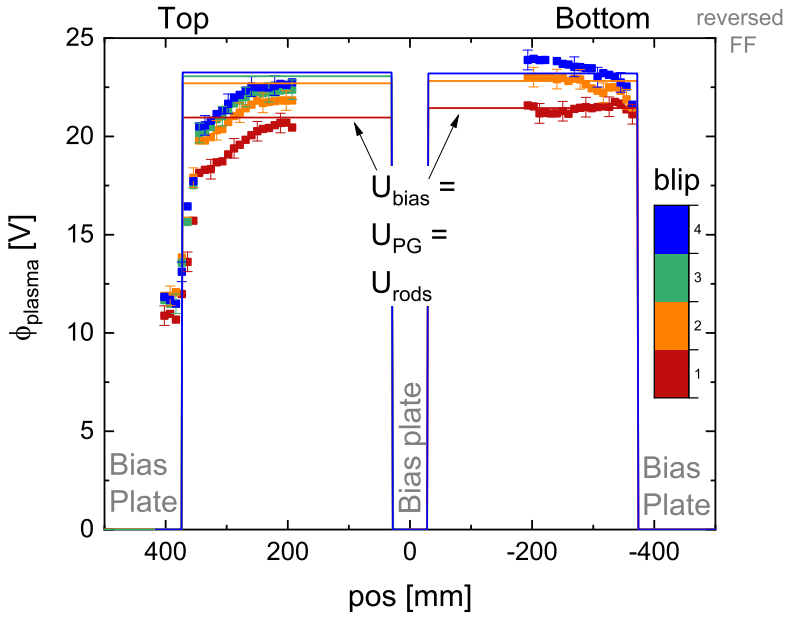

Figure 8.2: Vertical profile of the plasma potential ϕ_{plasma} measured with the movable RF-compensated Langmuir probe positioned at the top of the ion source. The top part is measured with the standard filter field, and the bottom part with the reversed filter field configuration. Values of the HV phase.The different colors specify the beam blip and the solid line indicates the wall potential according to the vertical position, i.e. U_{bias} at the PG and 0 V at the bias plate. Same pulse parameters of figure 8.1

The potential drop at the biased surfaces, i.e. $U_{\text{bias}} - \phi_{\text{plasma}}$, measured at the center of the beamlet groups is shown in figure 8.3 as a function of the beam blip. For the upper part of the ion source, the sheath at the potential rods and at the PG are electron attracting for every blip. The plasma potential at the top coincides within the error bar with the PG potential. From the second blip onward, the value of $U_{\text{bias}} - \phi_{\text{plasma}}$ gets, blip by blip, smaller thus the biased surface are less electron attracting. For the bottom, the value for the first beam blip is negative but close to zero and then the biased surfaces are more and more electron repelling. The error bar for these measurement is about 0.7 V, namely similar to the difference between ϕ_{plasma} and U_{bias} under investigation. Even if the absolute values is affected by a large

error bar, the relative trend of the measurement is anyway confirmed.

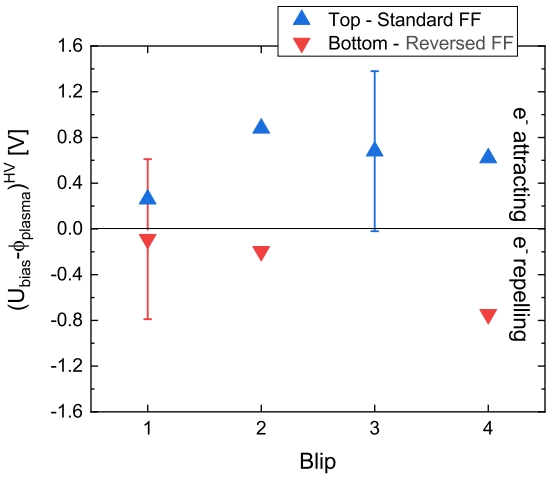

Figure 8.3: Value of $U_{\text{bias}} - \phi_{\text{plasma}}$ for the different beam blips of a long pulse. Top in blue and bottom in red. Value measured during the HV phase at 200 mm, i.e. at the center of the beamlet group. Same pulses of figure 8.2

The top-bottom asymmetry of the PG sheath affects the electron density in the plasma, proportional to the quantity $I(\phi_{\text{plasma}})$ measured by the LP, and, consequently, the co-extracted electrons. In figure 8.4*a)* the current at the plasma potential $I(\phi_{\text{plasma}})$ and the co-extracted electron current I_{EG} are plotted as a function of the plasma-wall interface $U_{\text{bias}} - \phi_{\text{plasma}}$. Solid symbols represents the co-extracted electron current $I_{\text{EG,top}}$ and the empty symbols are the measurements of the $I(\phi_{\text{plasma}})$ during the HV phase. Close to each symbol a number indicates the corresponding beam blip. The value of $I(\phi_{\text{plasma}})$ during the extraction phase decreases with increasing $U_{\text{bias}} - \phi_{\text{plasma}}$, namely the more the PG sheath is electron attracting the lower is the electron density in the plasma. Similarly as $I(\phi_{\text{plasma}})$, also the co-extracted electron current reacts to the PG sheath.
In figure 8.4*b)*, $I_{\text{EG,top}}$ is plotted as a function of $I(\phi_{\text{plasma}})^{\text{HV}}$. The co-extracted electrons are proportional to the electron density in the plasma measured during the extraction phase. Localized measurements of $I(\phi_{\text{plasma}})^{\text{HV}}$, i.e. mainly given by the electron density, measured with LP are correlated with the co-extracted electron current over one EG segment, a direct relation is still not possible due to the different measurement domain.

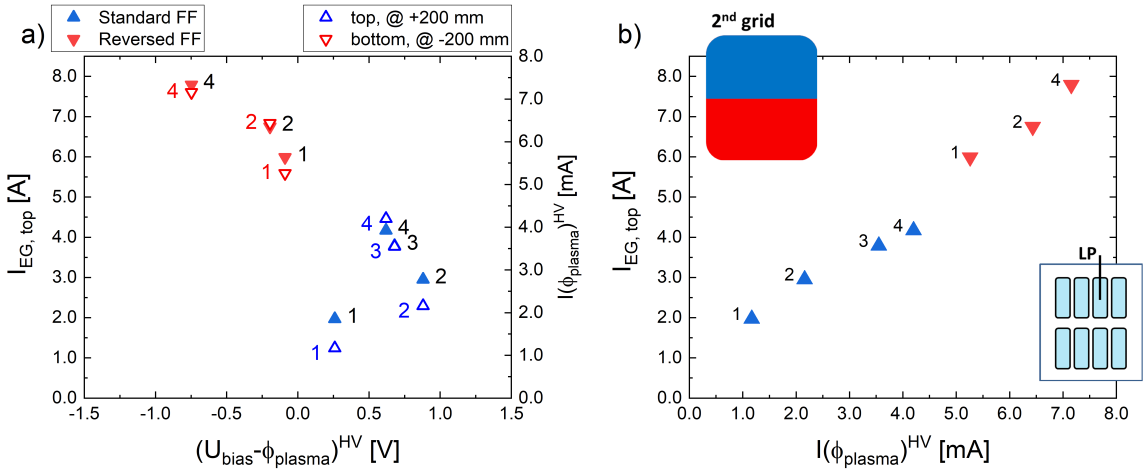

Figure 8.4: *a)* Co-extracted electron current (full symbols, left axis) and increase of $I(\phi_{\text{plasma}})$ during the HV phase with respect to the RF phase (open symbols, right axis) as a function of $U_{\text{bias}} - \phi_{\text{plasma}}$. Blue points refer to the standard FF and red points to the reversed FF. Values measured during the HV phase at 200 mm, i.e. at the center of the beamlet group. *b)* Co-extracted electron current as a function of $I(\phi_{\text{plasma}})$ during the HV. Same pulses of figure 8.1.

The PG work function degradation in time results in a more electron repelling sheath. The PG potential is, over the PG surface, an unique value, thus, due to the observed asymmetry in ϕ_{plasma}, it is not possible to have a symmetric sheath over the PG surface. On the other hand, the potential rods are divided in two segments electrically divided, which can be biased separately. In this way it is possible to test if an higher potential on the bottom rod segment is effective and reduces the co-extracted electrons. Such tests are planned for the near future.

8.2 Properties of the negative ion beam

The evolution of the accelerated beam current, divided in segments, and of the negative ion density in the plasma with the beam blips are studied in figure 8.5.
The negative ion density measured by the top CRDS LOS (see 8.5*a)*) shows the highest value for the first blip, then it decreases for the second beam blip and even more for the third blip. The bottom CRDS LOS shows that the negative ion density measured for the first beam blip is lower than for the second beam blip; the third beam blip shows a further slight decrease. The above considerations hold for the negative ion density measured during the RF phase and for the negative ion density measured during the the HV phase.

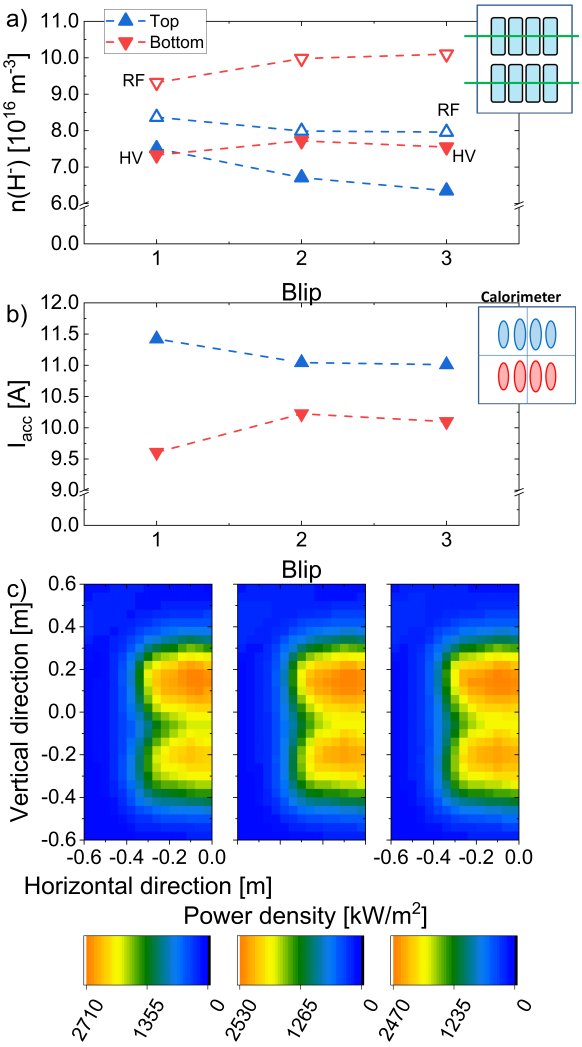

Figure 8.5: *a)* Negative ion density measured by CRDS along two LOS. In blue the density measured in the top LOS and in red the density measured in the bottom LOS. Empty symbols represent measurements performed during the RF phase, full symbols during the HV phase. *b)* Accelerated current for the top (blue) beam segment and bottom (red) beam segment. *c)* Left half of the 2D map of the beam power density. The corresponding color scale is reported at the bottom of the figure. Long pulse (320 s and three blips) parameters: H, p_{fill} = 0.3 Pa, P_{RF} = 65 kW/driver, I_{bias} = 35 A, I_{PG} = 1.6 kA + external strengthening magnets (1.9 mT), U_{ext} = 9 kV, U_{acc} = 45 kV.

During long pulses in hydrogen the beam properties show an higher dynamics especially for the first blip (see *b)*): the peak intensity of the top beam segment is higher than the bottom peak intensity, thus resulting in about 2 A more accelerated current in the top segment. For the blips after the first, the accelerated current decreases proportionally to the decrease of extracted current I_{ext} (not shown here, an example is shown in figure 3.16, page 60). After the first beam blip, the profile of the beam segments is mostly unaffected in terms of width and accelerated current symmetry as it can be qualitatively observed in figure 8.5*c)*.

The evolution of the negative ion density and the accelerated current from blip to blip is similar. What is different are the absolute values: for the first beam blip the top beam segment has a higher accelerated current than the bottom beam segment whereas the negative ion density are similar in absolute values, for both HV and RF phase. The measurement domain of the CRDS and of the accelerated current on the

beam segment are different: localized negative ion density at the center of the beamlet groups for the former and accelerated current over an entire beam segment for the latter. Thus, a univocal relationship between the accelerated current and negative ion density is not possible. Nevertheless, localized variations of the negative ion density are representative of variations in the beam segment accelerated current.
The increase of the negative ion density observed at the top of the ion source for the first beam blip is not clear: on one hand, the PG sheath, i.e. $U_{\mathrm{bias}} - \phi_{\mathrm{plasma}}$, is close to zero (see fig. 8.3) and, on the other hand, the electron density in the plasma is quite low (see $I(\phi_{\mathrm{plasma}})^{\mathrm{HV}}$ in 8.4*b)*). If only a small electron density in the plasma is observed, this may indicate that the emission of negative ions from the PG into the plasma is high, even during the extraction phase, to keep the electron density in the plasma low. This of course assumes a low work function at the PG, ensured by a sufficient amount of Cs on the plasma grid. The bottom part of the source shows a completely opposite behavior: the first blip shows a reduced negative ion density compared to the following blips. This can due to a reduction of atomic density, and consequently of atomic flux onto the PG, due to gettering of atoms with Cs as described in ref. [83]. For both hypotheses, an higher amount of Cs in the negative ion source is required and this is the case for the pulse under investigation.

9 Summary and conclusions

The neutral beam injection (NBI) system, which is foreseen to deliver heating and current drive in ITER, is based on a 2 m high and 1 m wide RF-driven negative hydrogen or deuterium ion sources. The target values for the ITER NBI ion source are an extracted negative ion current density of 329 A/m^2 in hydrogen and 286 A/m^2 in deuterium with a co-extracted electron current lower than the negative ion current for one hour pulse in deuterium (1000 s in hydrogen). The beam homogeneity, defined among apertures, has to be higher than 90% over the total beam surface and the single beamlet divergence has to be lower than 7 mrad. The low temperature, low pressure plasma is generated by inductive coupling in 8 cylindrical drivers and negative ions are mainly generated by surface conversion of atoms or positive ions on a low work function surface, which corresponds to the first grid (plasma grid) of the extraction and acceleration system. The low work function is achieved by evaporation of caesium into the ion source.

A horizontal magnetic field, called filter field, created by a current I_{PG} flowing vertically along the plasma grid is used to reduce electron temperature and density close to the plasma grid to minimize the destruction of negative ion due to impact with energetic electrons. The negative ions repel the electrons close to the extraction region, helping to reduce the co-extracted electrons. Additionally, the plasma grid is positively biased with respect to the source walls to further reduce the co-extraction of electrons. The presence of a horizontal filter field together with axial electric fields and density gradients leads to vertical plasma drifts which affect the vertical uniformity of the plasma density and plasma potential. Consequently also the vertical symmetry of the extracted negative ions and the co-extracted electrons is affected as well as the beam power density and divergence profiles. The ELISE test facility, which is equipped with a half-size (1 m×1 m) ion source, aims to demonstrate the ITER requirements in terms of extracted current density at an electron-to-ion ratio lower than one for long pulses in a large ions source. ELISE has demonstrated the scalability of the ion source performance from the prototype source (1/8 of ITER ion

source) to the large ion source in hydrogen for both long and short pulses. In deuterium the requirements are not yet reached. The extraction and acceleration system is made of three grids up to 60 keV energy.
The main limitation to the achievement of the ITER target values in deuterium in terms of negative ion extracted current density is the strong increase and the vertical asymmetry of the co-extracted electron current in short and long pulse operation. As a consequence, the applied RF power and extraction voltage are limited and, in turn, the extracted negative ion current. Furthermore, the power density profile of the negative ion beam is characterized by a vertical asymmetry between beam segments in terms of intensity and vertical width as well as divergence.
This work aims to correlate the plasma properties in terms of charged particle density and plasma potential to the co-extracted electron current and the beam properties to define operational knobs and recipes to reduce and symmetrize the co-extracted electrons, thus helping to reach the ITER requirement of the extracted current density. Along with the optimization on the co-extracted electrons, the beam uniformity is of high relevance to define a range of operational parameters which comply with the ITER requirements in terms of beam uniformity.
For this purpose several diagnostics are used combined with electrical measurements. The design of ELISE is characterized by an intrinsic vertical symmetry defined by segments (top and bottom) on the ion source and on the grid system. Electrical measurements over the large ion source components are thus mostly performed segment-wise and the currents collected on some of them are used to diagnose the plasma. Optical emission spectroscopy combined with a collisional-radiative model is used to determine electron density, temperature and atomic to molecular density ratio in the driver region. At two centimeters axial distance from the plasma grid in the top half of the source, an RF-compensated movable Langmuir probe is used for localized measurements of positive ion density, plasma potential and electron temperature close to the grid. Only relative estimations of the electron density are possible since the plasma is characterized by a high electronegativity. To investigate the plasma parameters with the movable probe in the bottom ion source half, a specific experimental campaign with reversed filter field is performed: in this configuration the plasma drift is reversed whereas the probe is always at the same position. The line-of-sight integrated negative ion density is determined with cavity ring-down spectroscopy at about 2 cm axial distance from the plasma grid for two vertical positions at the center of each ion source segment. The investigations are performed with the potential rods installed, namely positively biased surfaces at the same potential of the plasma grid,

which are oriented perpendicularly to the magnetic field lines. The potential rods are also separated in two segments at the top and at the bottom of the ion source. The concept was proven to have a beneficial effect on the symmetry of the positive ions in the plasma and of the co-extracted electrons.
The plasma potential is generally about 20 -30 V higher than the source walls, thus the current measured on non-biased surfaces is determined by the flux of positive ions whereas for biased surfaces the net current depends on the sheath potential drop, on the local particle density and on the emission of negative ions.
On the beam side, the diagnostic systems consist of beam emission spectroscopy on the Doppler-shifted H_α emission and infrared calorimetry on the diagnostic calorimeter, allowing the determination of the beam divergence, namely the width of the angular velocity distribution of the beam particle, and of the beam accelerated current on large portions of beam, i.e. beam segments. No insight on the single beamlet properties is possible due to the large beamlet overlap concurring at the diagnostics, i.e. 2.7 m distance for beam emission spectroscopy and 3.5 m distance for infrared calorimetry.
First, the symmetry of the plasma in the four drivers has been checked: the top-bottom and left-right symmetries of the plasma generated in the drivers has been demonstrated by comparing the measurements of the Balmer line emission, which coincide in the four drivers within the experimental error bars. The plasma in the drivers has been then characterized in terms of electron density, temperature and atomic to molecular density ratio: for an RF power of P_{RF}=70 kW/driver and in presence of magnetic field, the electron density is about $1.5 \cdot 10^{18}\mathrm{m}^{-3}$ in hydrogen (about $2 \cdot 10^{18}\mathrm{m}^{-3}$ in deuterium), and the electron temperature is about 11.5 eV (10.5 eV in D). The atomic to molecular density ratio is about 0.2 in hydrogen and about 0.35 in deuterium. All the quantities are affected by a relative error of about 30%. The presence of the horizontal magnetic filter field reduces the cross-field plasma diffusion of electrons, thus a slight increase of the electron density and of the atomic to molecular density ratio in the driver region is observed compared to the case without magnetic field.
Whereas the plasma properties in the drivers are top-bottom symmetric, in the expansion region the vertical plasma drifts play a role, resulting in a vertical non-uniformity of the plasma parameters at the plasma grid. The charged particle fluxes at the potential rods and at the plasma grid are fixed by the bias power supply, which draws a fixed positive net current, thus the plasma grid and the rod segments are at the

same potential U_{bias}. The analysis of the current on the different components highlights that the current collected on the plasma grid is negative between -20 A and -60 A and partially caused by emission of negative ions from the plasma grid into the plasma. The net current on the rods is between +40 A to +100 A and is mainly due to electrons impinging on the surface, hence removed from the plasma. For typical source parameters, the current collected by the top segment of the potential rods is higher than the bottom one by at least a factor 4. The asymmetry of the rod currents measured during the RF phase, is mainly caused by the plasma potential asymmetry between top and bottom of the source, since the electron density is comparable on the two sides of the ion source (measured also during the RF phase).
At the plasma grid the potential drop, i.e. $U_{\text{bias}} - \phi_{\text{plasma}}$, depends on the vertical position, since U_{bias} is the same for the entire plasma grid whereas the plasma potential depends on the vertical position. On the uppermost positions above the plasma grid the sheath is strongly electron attracting, whereas at the center of the upper beamlet group the plasma potential is similar to U_{bias}. An electron attracting sheath regime at the plasma grid is desirable because electrons can be collected at the plasma grid, thus decreasing the probability of co-extraction. At the bottom of the ion source the vertical profile of the plasma potential is flat and the value is, within the error bars, identical to U_{bias}. The positive ion density shows a slightly higher value at the top of the ion source, i.e. +10%, with respect to the bottom of the ion source.
The extraction phase has a strong impact on the plasma properties: negative ions are removed from the plasma and substituted by electrons to keep the plasma quasi neutrality, thus reducing the electronegativity of the plasma. During the RF phase the plasma parameters, i.e. positive ion density, electron density and plasma potential are identical within the experimental uncertainty between top and bottom of the ion source. Whereas a strong asymmetry, especially in terms of electron density, is observed between top and bottom, i.e. a factor 3-4 higher electron density at the bottom. A linear relation between electron density in the plasma during the extraction phase and co-extracted electron current is observed. Both the electron density in the plasma and the co-extracted electron current decrease when the potential drop at the plasma grid $U_{\text{bias}} - \phi_{\text{plasma}}$ increases, i.e. the sheath becomes more electron attracting. The plasma grid sheath is more electron attracting also by increasing the magnetic field strength and increasing the biasing of the plasma grid and rods, hence a decrease of the co-extracted electron is observed as well increasing the magnetic field strength and the biasing of the plasma grid.
Single beamlet characterization is not possible at ELISE, due to the large beamlet

overlapping occurring at the beam diagnostics. However, through a fitting function applied to the beam power density profile, localized measurements of the beamlet groups are possible, i.e. vertical position, accelerated current, vertical and horizontal widths. Thus, the beam homogeneity at ELISE is studied at the level of the beam segments where also line-of-sight integrated measurements of the beam divergence are possible. The minimum divergence for ELISE is obtained at about 0.25-0.30 normalized perveance, namely when the extracted current is 25%-30% of the maximum extractable current according to the Child-Langmuir law. Typically, the extraction system of ELISE is working in the under-perveant regime, namely the beam divergence decreases with increasing perveance, hence with increasing extracted current and/or with decreasing extraction voltage. Both beam segments follow the perveance law with the difference that, the top beam segments is characterized by a lower divergence with respect to the bottom segment. Such difference is due to a vertical asymmetry of the extracted negative ion current, thus the different beam optics is explained with a different perveance between top and bottom beam segments.

The operation at the ELISE test facility, which already fulfilled the ITER requirements on the extracted current density with an electron-to-ion ratio lower than one in hydrogen, shall comply with beam requirements in terms of homogeneity, which is defined at ELISE as symmetry of the accelerated current in the segments. The accelerated current symmetry is not affected by variations of the biasing voltage, but the beam divergence is slightly improved at strong value of biasing. On the other hand, the magnetic filter field affects the symmetry of the beam and the divergence of the beam segments: if the field strength is too high, thus reducing the extracted negative ion current, then the beam divergence gets worse. Thus, an intermediate value of magnetic field, i.e. between 1.5 and 2 mT, is the optimal value in hydrogen for both the ion source and the beam symmetry.

In deuterium, for identical experimental parameters as in hydrogen, the amount of co-extracted electrons increases by a factor of 4-10. The increase is caused both by an increased electron density, which is at least a factor 10 higher in deuterium, and by the potential drop which is less electron attracting in D with respect to H. In deuterium, the symmetry of the positive ion density improves as well as the symmetry of the beam accelerated current. Whereas, the asymmetry of the current collected on the potential rod gets worse, i.e. from a factor of 4 in H to a factor of 7 in D between top and bottom segments, thus suggesting a stronger asymmetry of the plasma potential in deuterium than in hydrogen. To stabilize and reduce the co-extracted electron current, a stronger filter field is needed: the sheath becomes electron attracting, and

the electron density in the plasma is strongly reduced. However, both the accelerated current symmetry and the beam segment divergence get worse due to the higher filter field. An higher biasing of the plasma grid in deuterium with respect to hydrogen is also beneficial, thus the plasma grid sheath would get more electron attracting.
An increase of the co-extracted electrons is observed during long pulses in hydrogen and deuterium, caused by a variation of potential drop, which becomes less electron attracting with time. The change of potential drop at the sheath results, thus, in an increase of the electron density in the plasma and of the co-extracted electrons in the beam. The temporal instability of the plasma grid sheath is due to a decrease of the emission of negative ions from the plasma grid, which is given by a degradation of the plasma grid work function determined by the Cs layer on it. Also, the negative ion beam shows, in most of the cases, a strong variation of the accelerated current during long pulses, especially between the first and the second extraction phases.
The plasma potential asymmetry is determined by the plasma transport due to the presence of a magnetic filter field. At the plasma grid the emission of negative ions strongly influences the sheath properties and the electron density. The electrons, in fact, are the minority species in the electronegative plasma close to the plasma grid and strongly react on small variations of the negative ion emission from the plasma grid, which are addressed to a degradation of the plasma grid work function. To stabilize the co-extracted electrons a refinement of the Cs-management needs to be developed as well as the implementation of measures to symmetrize the plasma potential or to vertically diversify the biasing of the biased surfaces. These actions can help in symmetrizing the charged particle fluxes on the plasma grid, thus symmetrizing the co-extracted electron current and the negative ion beam.
The transport and the physics of negative ions and electrons are of high relevance for the determination of the beam properties, thus a better experimental access to the quantities that defines the sheath properties is desirable. In particular, knowing the exact profile of the potential close to the PG or if the emission of negative ions from the plasma grid is space-charge limited would help in the interpretation of the measurements. To this purpose, the support of codes, e.g. the ONIX code [90], describing the sheath properties in a self consistent plasma model including emission of negative ions from the surface and magnetized particle species, is needed. The biasing of the plasma grid and of the potential rods seems also to influence the beam properties, thus this effect should be included in the simulations.
Variations of the beam divergence are mainly addressed to local variations of the beam perveance, but second order effects on the beam divergence have been observed, e.g.

a better beam divergence for strong plasma grid biasing, which cannot be explained with the perveance law. Further activities will help to study such cases, to determine how the sheath properties influence the beam divergence.
For the large beam at ELISE, where high power density and beamlet overlapping are inevitable, an increase in diagnostic resolution will still not be able to give beamlet level information. Therefore, coupling diagnostic measurements with beamlet simulations and transport codes such as IBSIMU [75] and BBCNI [74] is necessary for a better insight on the beam properties.

Acknowledgements

This work has been carried out within the framework of the EUROfusion Consortium and has received funding from the Euratom research and training programme 2014-2018 and 2019-2020 under grant agreement No 633053. The views and opinions expressed herein do not necessarily reflect those of the European Commission.

Bibliography

[1] *Fusion Physics*. Non-serial Publications. Vienna: International Atomic Energy Agency, 2012.

[2] *Blanket*. URL: `https://www.iter.org/mach/blanket`.

[3] ITER Physics Expert Group on Energe Drive and ITER Physics Basis Editors. "Chapter 6: Plasma auxiliary heating and current drive". In: *Nuclear Fusion* 39.12 (Dec. 1999), pp. 2495–2539.

[4] URL: `https://www.iter.org/mach/heating`.

[5] David R. Mikkelsen and Clifford E. Singer. "Optimization of steady-state beam-driven tokamak reactors." English (US). In: *Fusion Science and Technology* 4.2 pt 1 (Jan. 1983), pp. 237–252.

[6] J. Jacquinot, Martin Keilhacker, and Paul-Henri Rebut. "Mission and highlights of the JET Joint Undertaking: 1978-1999". In: *Fusion Science and Technology* 53 (May 2008).

[7] R. Hemsworth et al. "Status of the ITER heating neutral beam system". In: *Nuclear Fusion* 49.4 (Mar. 2009), p. 045006.

[8] M. Bacal and M. Wada. "Negative hydrogen ion production mechanisms". In: *Applied Physics Reviews* 2.2 (June 2015), p. 021305.

[9] K. H. Berkner, R. V. Pyle, and J. W. Stearns. "Intense, mixed-energy hydrogen beams for CTR injection". In: *Nuclear Fusion* 15.2 (Apr. 1975), pp. 249–254.

[10] R. S. Hemsworth et al. "Overview of the design of the ITER heating neutral beam injectors". In: *New Journal of Physics* 19.2 (Feb. 2017), p. 025005.

[11] B. Schunke et al. "Overview of the negative ion based neutral beam injectors for ITER". In: *Review of Scientific Instruments* 87.2 (2016), p. 02C101.

[12] Y. Okumura et al. "Development of a 500 keV, 22 A D- ion source for the neutral beam injector for JT-60U". In: *Review of Scientific Instruments* 67.3 (1996), pp. 1018–1020.

[13] E Speth et al. "Rf ion sources for fusion applications: design, development and performance". In: *Fusion Engineering and Design* 46.2-4 (Nov. 1999), pp. 383–388.

[14] A. Masiello et al. "European programme towards the 1MeV ITER NB injector". In: *Fusion Engineering and Design* 84.7-11 (June 2009), pp. 1276–1280.

[15] B. Heinemann et al. “Upgrade of the BATMAN test facility for H- source development”. In: *AIP Conference Proceedings* 1655.1 (2015), p. 060003.

[16] B Heinemann et al. “Towards large and powerful radio frequency driven negative ion sources for fusion”. In: *New Journal of Physics* 19.1 (Jan. 2017), p. 015001.

[17] B. Heinemann et al. “Design of the half-size ITER neutral beam source for the test facility ELISE”. In: *Fusion Engineering and Design* 84.2-6 (2009). Proceeding of the 25th Symposium on Fusion Technology(SOFT-25), pp. 915–922.

[18] B. Heinemann et al. “The negative ion source test facility ELISE”. In: *Fusion Engineering and Design* 86.6-8 (2011). Proceedings of the 26th Symposium of Fusion Technology (SOFT-26), pp. 768–771.

[19] B. Heinemann et al. “Achievements of the ELISE test facility in view of the ITER NBI”. In: *Fusion Engineering and Design* (Jan. 2019).

[20] V. Toigo et al. “The ITER Neutral Beam Test Facility towards SPIDER operation”. In: *Nuclear Fusion* 57.8 (July 2017), p. 086027.

[21] V. Toigo et al. “The PRIMA Test Facility: SPIDER and MITICA test-beds for ITER neutral beam injectors”. In: *New Journal of Physics* 19.8 (Aug. 2017), p. 085004.

[22] P. Agostinetti et al. “Detailed design optimization of the MITICA negative ion accelerator in view of the ITER NBI”. In: *Nuclear Fusion* 56.1 (Dec. 2015), p. 016015.

[23] M. Bacal et al. “Basic processes of negative hydrogen ion production and destruction in sources and beams (invited)”. In: *Review of Scientific Instruments* 67.3 (1996), pp. 1138–1143.

[24] M Bacal. “Physics aspects of negative ion sources”. In: *Nuclear Fusion* 46.6 (May 2006), S250–S259.

[25] P. W. van Amersfoort et al. “Formation of negative hydrogen ions on a cesiated W(110) surface; the influence of hydrogen implantation”. In: *Journal of Applied Physics* 58.9 (1985), pp. 3566–3572.

[26] J. N. Bardsley and J. M. Wadehra. “Dissociative attachment and vibrational excitation in low-energy collisions of electrons with H_2 and D_2”. In: *Physical Review A* 20.4 (Oct. 1979), pp. 1398–1405.

[27] Yu I Belchenko et al. “Studies of ion and neutral beam physics and technology at the Budker Institute of Nuclear Physics, SB RAS”. In: *Physics-Uspekhi* 61.6 (June 2018), pp. 531–581.

[28] W.M. Haynes. *CRC Handbook of Chemistry and Physics*. CRC Handbook of Chemistry and Physics. CRC Press, 2014.

[29] G.D. Alton. “Semi-empirical mathematical relationships for electropositive adsorbate induced work function changes”. In: *Surface Science* 175.1 (1986), pp. 226–240.

[30] J. D. Isenberg, H. J. Kwon, and M. Seidl. “Surface production of H- ions by backscattering of H^+ and H_2^+ ions in the 3-50 eV ion energy range”. In: *AIP Conference Proceedings* 287.1 (1992), pp. 38–47.

[31] Brian S. Lee and M. Seidl. “Surface production of H-ions by hyperthermal hydrogen atoms”. In: *Applied Physics Letters* 61.24 (Dec. 1992), pp. 2857–2859.

[32] R. Celiberto et al. “Cross section data for electron-impact inelastic processes of vibrationally excited molecules of hydrogen and its isotopes”. In: *Atomic Data and Nuclear Data Tables* 77.2 (Mar. 2001), pp. 161–213.

[33] U. Fantz et al. “A comparison of hydrogen and deuterium plasmas in the IPP prototype ion source for fusion”. In: *AIP Conference Proceedings* 1515.1 (2013), pp. 187–196.

[34] R. K. Janev, D. Reiter, and U. Samm. *Collision Processes in Low-Temperature Hydrogen Plasmas*. Tech. rep. Jül-4105. Forschungszentrum Jülich, Dec. 2003.

[35] P McNeely and D Wünderlich and. “Neutral depletion in an H-source operated at high RF power and low input gas flow”. In: *Plasma Sources Science and Technology* 20.4 (May 2011), p. 045005.

[36] P. Franzen et al. “Progress of the development of the IPP RF negative ion source for the ITER neutral beam system”. In: *Nuclear Fusion* 47.4 (Mar. 2007), pp. 264–270.

[37] E Speth et al. “Overview of the RF source development programme at IPP Garching”. In: *Nuclear Fusion* 46.6 (May 2006), S220–S238.

[38] Yukikazu Itikawa. “Momentum-transfer cross sections for electron collisions with atoms and molecules”. In: *Atomic Data and Nuclear Data Tables* 14.1 (July 1974), pp. 1–10.

[39] Joseph Donald Huba. *NRL: Plasma formulary*. Tech. rep. DTIC Document, 2004.

[40] R McAdams et al. “Transport of negative ions across a double sheath with a virtual cathode”. In: *Plasma Sources Science and Technology* 20.3 (May 2011), p. 035023.

[41] Francis F. Chen. *Introduction to Plasma Physics*. Springer US, 1995.

[42] L. Schiesko et al. “Magnetic field dependence of the plasma properties in a negative hydrogen ion source for fusion”. In: *Plasma Physics and Controlled Fusion* 54.10 (2012), p. 105002.

[43] S. Lishev et al. “Spatial distribution of the plasma parameters in the RF negative ion source prototype for fusion”. In: *AIP Conference Proceedings* 1655.1 (2015), p. 040010.

[44] D Wünderlich, R Gutser, and U Fantz. “PIC code for the plasma sheath in large caesiated RF sources for negative hydrogen ions”. In: *Plasma Sources Science and Technology* 18.4 (Oct. 2009), p. 045031.

[45] L. Schiesko, D. Wünderlich, and I. M. Montellano. "Kinetic sheath in presence of multiple positive ions, negative ions, and particle wall emission". In: *Journal of Applied Physics* 127.3 (Jan. 2020), p. 033302.

[46] P McNeely et al. "A Langmuir probe system for high power RF-driven negative ion sources on high potential". In: *Plasma Sources Science and Technology* 18.1 (Nov. 2008), p. 014011.

[47] A. Mimo et al. "Cavity ring-down spectroscopy system for the evaluation of negative hydrogen ion density at the ELISE test facility". In: *Review of Scientific Instruments* 91.1 (Jan. 2020), p. 013510.

[48] U. Fantz and Ch. Wimmer. "Quantification Of Cesium In Negative Hydrogen Ion Sources By Laser Absorption Spectroscopy". In: *AIP Conference Proceedings* 1390.1 (2011), pp. 348–358.

[49] C Wimmer, M Lindauer, and U Fantz. "Determination of the Cs distribution along a line of sight by the Zeeman splitting in an inhomogeneous magnetic field". In: *Journal of Physics D: Applied Physics* 51.39 (Aug. 2018), p. 395203.

[50] D. Wünderlich et al. "Modeling the particle transport and ion production in a RF driven negative hydrogen ion source for ITER NBI". In: *AIP Conference Proceedings* 1515.1 (2013), pp. 12–21.

[51] R Gutser, D Wünderlich, and U Fantz and. "Negative hydrogen ion transport in RF-driven ion sources for ITER NBI". In: *Plasma Physics and Controlled Fusion* 51.4 (Feb. 2009), p. 045005.

[52] Alessandro Mimo. "Optimization of Caesium Dynamicsin Large and Powerful RF Sourcesfor Negative Hydrogen Ions". PhD thesis. Universität Augsburg, 2018.

[53] C. D. Child. "Discharge From Hot CaO". In: *Physical Review (Series I)* 32.5 (May 1911), pp. 492–511.

[54] Ian Brown. *The Physics and Technology of Ion Sources, Second Edition*. Ed. by Ian G. Brown. Second, Revised and Extended Edition. Wiley-VCH, Oct. 2004.

[55] A. Ben Ismail et al. "Space charge compensation studies of hydrogen ion beams in a drift section". In: *Phys. Rev. ST Accel. Beams* 10 (7 July 2007), p. 070101.

[56] R. S. Hemsworth et al. "Status of the Development of the SINGAP Accelerator for ITER". In: *AIP Conference Proceedings* 925.1 (2007), pp. 290–305.

[57] R. Gutser et al. "Simulations for the generation and extraction of negative hydrogen ions in RF-driven ion sources". In: *AIP Conference Proceedings* 1097.1 (2009), pp. 297–306.

[58] D. Wünderlich et al. "Optical emission spectroscopy at the large RF driven negative ion test facility ELISE: Instrumental setup and first results". In: *Review of Scientific Instruments* 84.9, 093102 (2013).

[59] M. Giacomin. "Application of collisional radiative models for atomic and molecular hydrogen to a negative ion source for fusion". MA thesis. Università degli Studi di Padova, 2017.

[60] B. Der Van Sijde, J. J. A. M. Van der Mullen, and D. C. Schram. "Collisional radiative models in plasmas". In: *Beiträge aus der Plasmaphysik* 24.5 (1984), pp. 447–473.

[61] D. Wünderlich et al. "Yacora on the Web: Online collisional radiative models for plasmas containing H, H2 or He". In: *Journal of Quantitative Spectroscopy and Radiative Transfer* 240 (Jan. 2020), p. 106695.

[62] S. Briefi and U. Fantz. "Spectroscopic investigations of the ion source at BATMAN upgrade". In: *AIP Conference Proceedings* 2052.1 (2018), p. 040005.

[63] U. Fantz and D. Wünderlich. "A novel diagnostic technique for H-(D-) densities in negative hydrogen ion sources". In: *New Journal of Physics* 8.12 (Dec. 2006), pp. 301–301.

[64] U. Fantz et al. "Spectroscopy - a powerful diagnostic tool in source development". In: *Nuclear Fusion* 46.6 (2006), S297.

[65] C. Wimmer et al. "Improved understanding of the Cs dynamics in large H-sources by combining TDLAS measurements and modeling". In: *AIP Conference Proceedings* 2011.1 (2018), p. 060001.

[66] Francis F. Chen and Jane P. Chang. *Lecture Notes on Principles of Plasma Processing*. Springer US, 2003.

[67] Francis F Chen. "Langmuir probe measurements in the intense RF field of a helicon discharge". In: *Plasma Sources Science and Technology* 21.5 (Sept. 2012), p. 055013.

[68] Christian Wimmer. "Characteristics and dynamics of the boundary layer in rf-driven sources for negative hydrogen ions". PhD thesis. Universität Augsburg, 2014.

[69] Francis F Chen. "Langmuir probes in RF plasma: surprising validity of OML theory". In: *Plasma Sources Science and Technology* 18.3 (May 2009), p. 035012.

[70] V A Godyak, R B Piejak, and B M Alexandrovich. "Measurement of electron energy distribution in low-pressure RF discharges". In: *Plasma Sources Science and Technology* 1.1 (Mar. 1992), pp. 36–58.

[71] R. Nocentini et al. "Beam diagnostic tools for the negative hydrogen ion source test facility ELISE". In: *Fusion Engineering and Design* 88.6-8 (2013). Proceedings of the 27th Symposium On Fusion Technology (SOFT-27); Liège, Belgium, September 24-28, 2012, pp. 913–917.

[72] P. Franzen and U. Fantz. "Beam Homogeneity Dependence on the Magnetic Filter Field at the IPP Test Facility MANITU". In: *AIP Conference Proceedings* 1390.1 (2011), pp. 310–321.

[73] Isabella Mario et al. "Reconstruction of the large multi-aperture beam via IR calorimetry technique and beam emission spectroscopy at the ELISE test facility". In: *Nuclear Fusion* (Apr. 2020).

[74] A. Hurlbatt et al. “The particle tracking code BBCNI for negative ion beams and its application to BATMAN upgrade”. In: *AIP Conference Proceedings* 2052.1 (2018), p. 040007.

[75] T. Kalvas et al. “IBSIMU: A three-dimensional simulation software for charged particle optics”. In: *Review of Scientific Instruments* 81.2 (2010), 02B703.

[76] Niek Den Harder. Private communication. Aug. 2019.

[77] U. Fantz et al. “Achievement of the ITER NBI ion source parameters for hydrogen at the test facility ELISE and present Status for deuterium”. In: *Fusion Engineering and Design* 156 (July 2020), p. 111609.

[78] U. Fantz et al. “Advanced NBI beam characterization capabilities at the recently improved test facility BATMAN Upgrade”. In: *Fusion Engineering and Design* (Dec. 2018).

[79] R. Nocentini et al. “Advanced ion beam calorimetry for the test facility ELISE”. In: *AIP Conference Proceedings* 1655.1 (2015), p. 060006.

[80] D. Wünderlich et al. “Long pulse operation at ELISE: Approaching the ITER parameters”. In: *AIP Conference Proceedings* 2052.1 (2018), p. 040001.

[81] R. Friedl and U. Fantz. “Influence of H2 and D2 plasmas on the work function of caesiated materials”. In: *Journal of Applied Physics* 122.8 (Aug. 2017), p. 083304.

[82] F. Bonomo et al. “Uniformity of the large beam of ELISE during Cs conditioning”. In: *AIP Conference Proceedings* 2052.1 (2018), p. 040002.

[83] D. Wünderlich et al. “Achievement of ITER-relevant accelerated negative hydrogen ion current densities over 1000 s at the ELISE test facility”. In: *Nuclear Fusion* 59.8 (June 2019), p. 084001.

[84] D Wünderlich et al. “Influence of the magnetic field topology on the performance of the large area negative hydrogen ion source test facility ELISE”. In: *Plasma Physics and Controlled Fusion* 58.12 (Oct. 2016), p. 125005.

[85] P Franzen et al. “Magnetic filter field dependence of the performance of the RF driven IPP prototype source for negative hydrogen ions”. In: *Plasma Physics and Controlled Fusion* 53.11 (Oct. 2011), p. 115006.

[86] U. Fantz et al. “A comparison of hydrogen and deuterium plasmas in the IPP prototype ion source for fusion”. In: *AIP Conference Proceedings* 1515.1 (2013), pp. 187–196.

[87] D. Wünderlich et al. “Formation of large negative deuterium ion beams at ELISE”. In: *Review of Scientific Instruments* 90.11 (Nov. 2019), p. 113304.

[88] U Fantz and D Wünderlich. “Effective rate coefficients for molecular processes of hydrogen and hydrocarbons in edge plasmas”. In: *Atomic and plasma-material interaction data for fusion* (2008), p. 56.

[89] Andrew Hurlbatt et al. “Improved understanding of beamlet deflection in ITER-relevant negative ion beams through forward modelling of Beam Emission Spectroscopy”. In: *Fusion Engineering and Design* 153 (Apr. 2020), p. 111486.

[90] I. M. Montellano et al. “3D-PIC modelling of a low temperature plasma sheath with wall emission of negative particles and its application to NBI sources”. In: *Journal of Physics D: Applied Physics* 52.23 (Mar. 2019), p. 235202.